Neuromorphic Vision Sensors for Space-Based Applications

THESIS

Jessica L. Horn, Captain, USAF

AFIT-ENY-MS-21-M-304

DEPARTMENT OF THE AIR FORCE
AIR UNIVERSITY

AIR FORCE INSTITUTE OF TECHNOLOGY

Wright-Patterson Air Force Base, Ohio

AFIT-ENY-MS-21-M-304

NEUROMORPHIC VISION
SENSORS FOR SPACE-BASED APPLICATIONS

THESIS

Presented to the Faculty

Department of Aeronautics and Astronautics

Graduate School of Engineering and Management

Air Force Institute of Technology

Air University

Air Education and Training Command

in Partial Fulfillment of the Requirements for the

Degree of Master of Science in Space Systems

Jessica L. Horn, BS

Captain, USAF

25 March 2021

AFIT-ENY-MS-21-M-304

NEUROMORPHIC VISION
SENSORS FOR SPACE-BASED APPLICATIONS

Jessica L. Horn, BS
Captain, USAF

Committee Membership:

Lt Col Bryan D. Little, Ph.D
Chairman

Richard G. Cobb, Ph.D
Member

Andrew S. Keys, Ph.D
Member

Abstract

This research examines the viability of event-based vision (neuromorphic) sensors for future use on satellites. Outputting single pixel events only when a change in intensity is detected, event-based vision sensors offer a potential low power, low latency, high temporal resolution, and high dynamic range solution as compared to traditional CCD or CMOS camera technology. The commercial off-the-shelf (COTS) DVS240C sensor, is analyzed to determine if operability is affected by launch conditions and the low Earth space environment through vacuum, thermal vacuum, and vibration tests. No appreciable changes in sensor operation was observed throughout testing. Additionally, the sensor was able to detect both bright and dark objects directly in front of a solar simulator without pixel saturation, demonstrating its high dynamic range which provides a possible advantage for use on space-based platforms.

Acknowledgements

I would first like to thank my advisor, Lt Col Bryan Little, for providing guidance and support throughout the thesis writing process and always being available to discuss my ideas or questions. I would also like to thank the Center for Space Research and Assurance staff, whom without, this thesis would not have been possible. A particular thank you to Blake Benton and Phil Smith for aiding in the manufacture and design of the supporting equipment needed for my experimental setups and a particular thank you to Chris Sheffield for all of the time spent helping me with thermal vacuum and vibration testing. Additionally, I would like to thank the other members of my committee for their feedback and specifically Dr.Cobb for opening my eyes to neuromorphic vision sensors as a thesis research topic. Finally, I'd like to thank my friends and family for all their support while I was completing this project.

Jessica L. Horn

Contents

Page

List of Figures

Figure Page

Figure Page

Figure Page

Figure Page

Figure Page

List of Tables

NEUROMORPHIC VISION

SENSORS FOR SPACE-BASED APPLICATIONS

I. Introduction

1.1 Background and Motivation

Biology and nature have often inspired science and engineering. Discovering the high specific strength of beehives' honeycomb structure and the adhesiveness of plant burrs clinging to dog fur led to advances in aerospace manufacturing and the invention of Velcro. Neuromorphic or event-based vision sensors are also an example of biology inspired technology. Motivated by the desire to replicate biological vision and the signal spikes sent by neurons in the eye to the brain, event-based sensors output information in the same manner. Instead of producing images or frames at pre-determined rates like a conventional camera, event-based vision sensors use 'spikes' or 'events' triggered by intensity changes to convey information about the dynamics of a scene. It is the new mode of operation that event-based sensors offer which drives this research.

Additionally, this research is motivated by the current limitations existing within traditional camera technology in the space domain and the notion that event-based camera technology can be used to improve upon these limitations. Conventional space camera technologies have a limited dynamic range when compared to event-based sensors. The dynamic range of conventional cameras are typically around 60 dB whereas event-based cameras have dynamic ranges closer to 120 dB [7]. This means that traditional cameras cannot operate in as diverse lighting environments.

Traditional cameras have more difficulty with high contrast environments and are also susceptible to saturation from too much light (i.e. the Sun) without setting changes. Moreover, conventional camera technology encounters issues when faced with fast movement/changes in the sensor field of view. Without a quick enough frame rate and integration time compared to the movement, motion blur will become an issue. Additionally, event-based cameras typically have lower data rates than conventional cameras because they generate data based solely on scene dynamics. No data is generated if nothing within the field of view of the sensor changes. Lastly, size, weight, and power (SWaP) are crucial metrics to consider when designing sensors and payloads. With companies like SpaceX making it easier and cheaper to launch; smaller satellites ($<$ 100 kg) are becoming more prevalent. While engineers are constantly trying to improve upon conventional space camera technology, often times there is a trade off between performance capabilities and SWaP, with increased capability dependent upon a larger, heavier, more power hungry system. Event-based sensors offer a new way to address the issues encountered with traditional space camera technology providing a low power, low latency, high temporal resolution, and high dynamic range solution.

Although event-based technology was originally meant to improve upon machine vision and the operation of autonomous vehicles, the use of event-based vision sensors has expanded to other domains and applications. This research seeks to further expand the application of the technology in the space domain. Looking at the advantages of event-based sensors and the limitations of conventional cameras, the goal of this research is to investigate the COTS sensor's ability, specifically the DVS240C, to survive space conditions and provide potential space-based application to further defense research and future use of event-based vision sensor technology.

1.2 Research Objectives

This thesis aims to build an understanding of how event-based sensors operate and examine the viability for their use in the space domain. To do this, a commercial off-the-shelf (COTS) event-based vision sensor is used to analyze survivability in launch conditions and the low Earth space environment. This research also considers the potential of the event-based sensor to fulfill a space mission set, investigating the sensor's capabilities and advantages for space-based space domain awareness (SDA).

The overall goal of the research is to determine the viability for event-based sensors on small satellites; all testing, data collection, and analysis uses the DVS240C COTS product by iniVation. The hardware is able to produce both frames like a conventional camera and events like an event-based camera, however, it cannot output both simultaneously. The thesis scope covers survivability testing and an application demonstration with all tests geared towards initial discovery and investigation. The thesis will investigate the DVS240C's ability to survive vacuum and thermal vacuum environments similar to those seen in low Earth orbit. It will also investigate the DVS240C's ability to survive vibration conditions similar to those seen during launch. The thesis focuses on sensor operation as a survivability measure, given that the COTS sensor is not part of an integrated payload. Furthermore, the application demonstration serves to display how the output from event-based vision sensors could be used to fulfill gaps that exist with current space camera technology. The tests seek to show the promise of further research and development with event-based vision sensors for space-based space domain awareness applications.

Ultimately, the objective of this thesis is to show that if the event-based sensor can survive launch, operate in space, and perform relevant space missions, then it is viable for future small satellite use.

1.3 Thesis Document Overview

This thesis includes five chapters. Chapter I addresses the motivation behind the work, touching upon the limitations of current space camera technology while introducing the potential of event-based vision technology. It outlines the research objectives that this thesis will cover and relates some initial assumptions as well as the scope of the work. Chapter II is a background and literature review which gives more detail about how the event-based vision sensors operate, the advantages they hold, and several examples of where they have been used. It also explains the difficulties of the LEO space environment and the type of conditions space electronics need to survive to ensure mission success. In addition, Chapter II touches upon the SDA mission set, addressing gaps and revealing a potential application for the event-based vision sensor. Chapter III discusses the two types of testing done in this research – survivability testing and application testing. It describes the testing methodologies, setups, and how each test demonstrates either a survivability or application concept. Additionally, this section explains the analysis methodology that is used for several of these tests. Chapter IV, discusses the results of the testing and explains anomalies and discoveries in the data. Finally, Chapter V summarizes the testing results discussed in Chapter IV and gives an overall conclusion for the initial posed research question. The chapter points out areas for further research and investigation, explains the significance of the research, and details what it means for the future use of the sensor.

II. Literature Review

2.1 Chapter Overview

This chapter describes how event-based vision sensors work. It discusses the biological inspiration for the sensors, the various types of sensors available, and the Dynamic Vision Sensor (DVS) pixel operation. It also touches upon event-based sensor advantages compared to conventional cameras and describes several of its current applications. Additionally, this chapter gives an overview of the challenges of the harsh space environment. It describes the difficult conditions electronics and sensors experience from launch to low Earth orbit. Finally, this chapter presents space application for the technology. It discusses capability gaps in SDA and suggests how event-based vision sensors could aid in filling those gaps.

2.2 Event-based Camera Technology

Event-based vision sensors or silicon retinas are biologically inspired devices. With the introduction of neuromorphic engineering in the late 1980's, Carver Mead, a California Institute of Technology professor, created the first silicon retina prototype with his PhD student in 1991 [8]. Meant to mimic biological vision, event-based sensor pixels operate independently and asynchronously, outputting a temporal stream of events only when the pixel detects a change in brightness [14]. This is vastly different than conventional CCD or CMOS technology which capture data by collecting frames or images at a specified rate. Therefore, event-based sensors have several advantages over conventional sensor technology. This research specifically considers the possibilities and advantages these sensors could hold for defense applications in space, particularly in regards to small satellites.

2.2.1 Bio-Inspired Vision

Biological vision occurs when light passes through the eye and hits the retina. The retina is a thin layer of tissue located at the back of the eye which takes focused light and converts it into neural signals. It is composed of three main layers. The first layer is known as the photoreceptor layer and it contains rods and cones. The job of these cells is to convert light into electrical signals [9]. The photoreceptor layer feeds into the outer and inner plexiform layers which contain horizontal, bipolar, amacrin, and ganglion cells as shown in Figure 1. The cells form a network and together look at contrast changes in both time and space. The bipolar cells compare signals received from photoreceptors with spatiotemporal averages computed by horizontal cells [9]. It is these relative differences, rather than absolute values, which get passed off to the ganglion cells and ultimately the optic nerve. Figure 2 shows another representation of the retina cell network, aligning it with the circuit stages of an event-based sensor pixel.

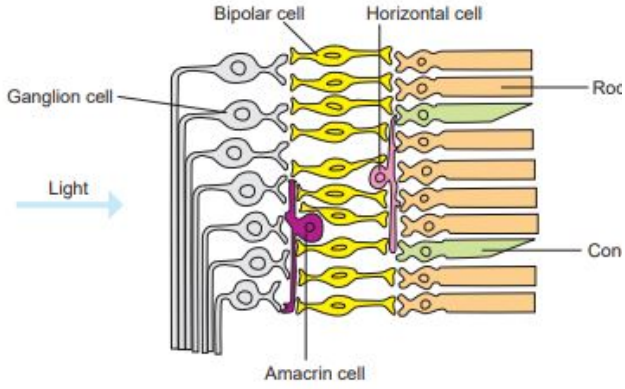

Figure 1. Cross Section of the Retina [1]

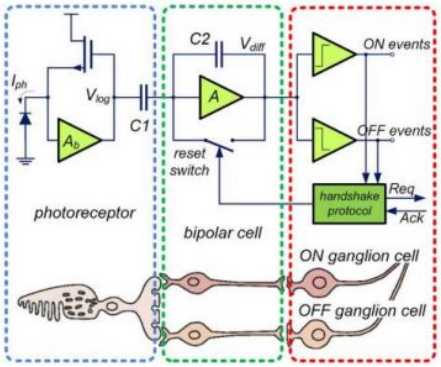

Figure 2. Retina Cell Network [2]

Operating in this manner allows biological retinas to work for a variety lighting conditions and discard unnecessary information rather than passing it to the brain. This effectively provides local gain control, redundancy reduction, and activity-driven

capabilities [9]. For example, the human eye is able to see a dynamic range of 200 dB [1], providing vision at both nighttime and in bright sunlight environments. Additionally, retinas use temporal contrast changes to perceive the environment instead of measuring the power and spectral composition of light. Therefore, it is an object's form, structure, surface, and motion which are the most important aspects of vision. A chair remains the same in both dark and light conditions, however, light reflects off the object differently in the two cases. Therefore, absolute illumination information gives details about the light source as well as the object. Biological retinas are able to filter out this absolute data and give local illumination ratios instead, which only carries information about the object itself [7, 9]. Finally, the retina is a large network of interconnected cells which do not use frame rates for a readout. Cells send signals when they see local spatiotemporal contrast changes and are therefore constantly sending information when there are scene changes. This allows them to observe and detect objects and scene dynamics much faster than a conventional camera. These advantages are the inspiration of the event-based sensors, which are designed to electronically model the communication architecture of biological retinas described above by translating these visual processing steps onto a silicon chip [9].

2.2.2 Dynamic Vision Sensor

The first commercial sensor of this type was created by T. Delbruck in 2008 and it is known as the Dynamic Vision Sensor (DVS) [15]. The DVS and other event-based sensors sample light based upon the dynamics of the scene within the sensor's field of view [8]. Each pixel within the focal plane array (FPA) is able to operate independently and asynchronously, responding to brightness changes where brightness is represented by the log intensity of the light [8]. The output of a DVS sensor is a continuous stream of 'events' or 'spikes,' representing this changing log intensity in

the scene. Since events are only produced when brightness changes are detected, the rate that events are produced can vary unlike conventional cameras with fixed frame rates. The DVS240C is the event-based camera used throughout this research and therefore a more in depth description will be given to how the DVS pixel operates.

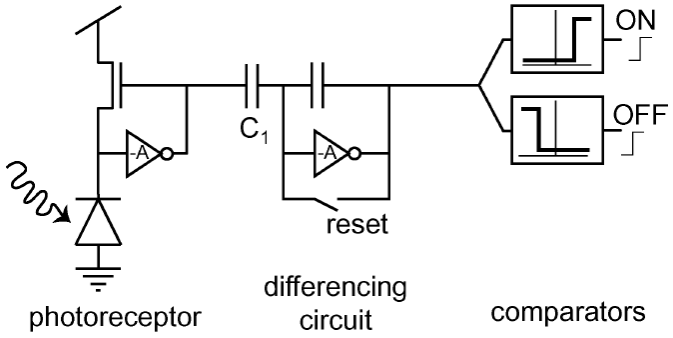

Figure 3. Abstracted DVS Pixel Circuit [3, 4]

As shown in Figure 3, the DVS pixel circuit has three main stages - the photoreceptor stage, the differencing circuit stage, and the comparator stage. The photoreceptor stage emulates the job of the photoreceptors, taking the incoming photons and turning them into a logarithmic voltage. Next, the differencing circuit or the change amplifier stage mimics the job of the bipolar cells. It uses a capacitor to block all DC voltage, only allowing relative illumination level information to pass through by stopping the absolute information of the signal from passing when the circuit is reset. This stage also contains an amplifier and event reset switch. Each time an event is triggered, the switch closes and opens, setting the voltage to a fixed value, essentially storing or memorizing the log intensity value [8]. Finally, the last stage contains the comparators which are meant to imitate the ganglion cells. This stage takes the amplified change in light intensity and relays it into a digital 'event.' There are two types of events, 'ON' events and 'OFF' events, representing an increase in light intensity and a decrease in light intensity respectively [16, 17]. If the change in

light intensity is greater than the threshold intensity value, an event is triggered as shown in Figure 4.

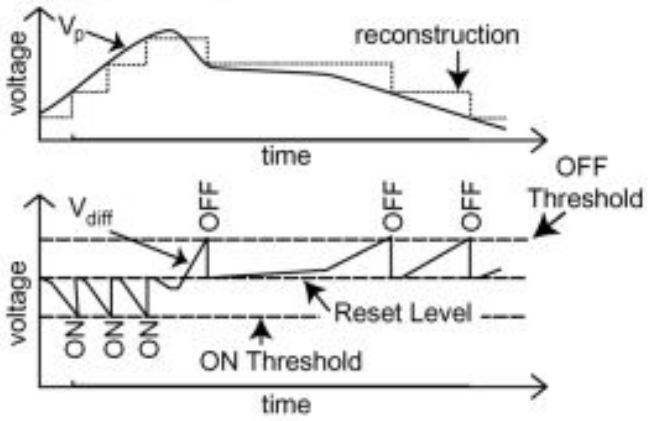

Figure 4. DVS Pixel Operation [3, 4]

The DVS and other event-based sensors use Address Event Representation (AER) communication protocol, a protocol commonly used in neuromorphic technology. AER protocol is meant to emulate the way in which neurons communicate through action-potentials or 'spikes' as well as the asynchronous nature of the neuron spikes as they are multiplexed into a single channel output [9]. Each event (e) is sent from the pixel to a shared bus with an AER output that contains a timestamp, position, and polarity information.

$$\mathrm{e} = [\mathrm{t}, \mathrm{x}, \mathrm{y}, \mathrm{p}]^{\mathrm{T}}$$

In the DVS output, t is the time at which the event occurred, x and y is the location of the pixel that generated the event, and p is the polarity that indicates if there was an increase or decrease in brightness. The combination of detecting only contrast changes with AER communication protocol enables a high compression rate and a high temporal resolution [1]. Therefore, the DVS is able to have a high-dynamic range and low latency response times on the order of microseconds.

In addition to its low latency response times, the DVS has high temporal resolution because of the asynchronous nature of the individual pixels. This asynchronous nature allows pixels to output events as soon as they detect a change in brightness. This makes the sensor particularly good for highly dynamic environments. With a fixed frame rate, conventional cameras may miss scene dynamics or have motion blur because they are unable to capture data quickly enough. While in some cases conventional cameras don't capture data quickly enough, in other cases they may be capturing too much data. If you want to pick up motion or changes in a scene and there are none, with a fixed frame rate, information would be recorded regardless and storage space would be wasted.

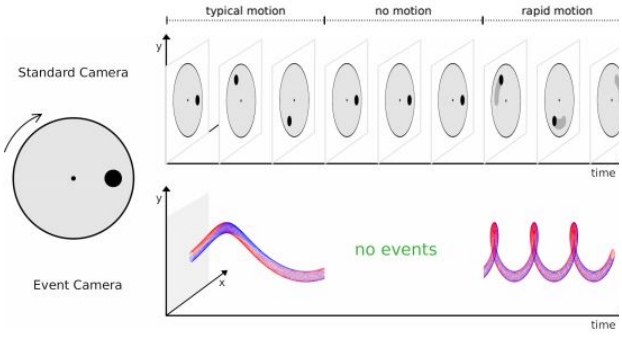

Figure 5. Frame v. Event Output [5, 6, 7]

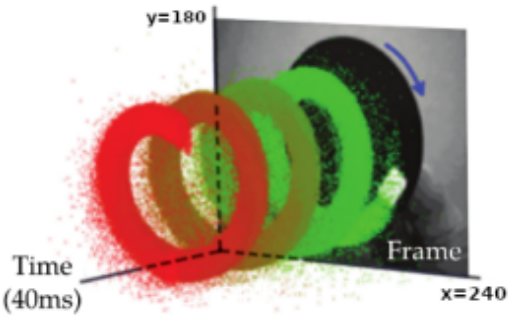

Figure 6. Event Output from DVS [8]

Figure 5 compares output from a standard camera versus an event-based camera for a rotating black dot. The first part of the graph indicates typical motion capture where the standard camera produces frames showing the black dot at different positions as it rotates. The event-based camera produces a continuous stream of events, showing the circular motion of the black dot as a corkscrew. The middle part of the graph shows output when there is no motion (stationary black dot). The standard camera continues to produce identical while the event-based camera produces no data. Finally, the last part of the graph shows the black dot rotating very quickly. Fast rotation creates motion blur with the standard camera output, but a more condensed

corkscrew with the event-based camera. Figure 6 is another representation of the DVS event output from the motion of a rotating circle. The image displays 40ms of data and is color coded with green indicating past events and red indicating present events. As seen with the rotating circles in Figure 5 and Figure 6, DVS events are only generated if there is motion and/or brightness change in the scene. Without these changes, the sensor will not trigger any events and therefore no data will be generated. Depending on the application of the sensor, this leads the DVS to have lower power consumption and data usage as a result. Clearly, the DVS operates with a completely different model than conventional cameras and has several advantages over conventional cameras.

Although the operation and advantages of the DVS pixel are described in this section, it is important to note that this is not the only type of event-based sensor that exists commercially. The Asynchronous Time-Based Imaging Sensor (ATIS) by Prophesee and the Dynamic and Active Vision Image Sensor (DAVIS) by IniVation (same maker as the DVS) are two comparable commercial event-based sensors. In addition to using DVS-like circuitry to generate AER events revealing relative brightness information, both the ATIS and the DAVIS give absolute brightness information as well [7, 8]. The ATIS pixel seen in Figure 7 contains a supplemental asynchronous exposure measurement circuit which uses Pulse-Width-Modulation (PWM) when triggered by AER events [11, 2]. This allows the pixel to determine the appropriate integration time based upon level of the signal [4]. The DAVIS also gives absolute brightness information with the addition of an active pixel sensor (APS) [8]. The APS circuit uses the same photodiode as the DVS circuit and enables the DAVIS to simultaneously produce both frames (like a conventional camera) and events [8]. Figure 8 illustrates the abstracted DAVIS pixel circuitry.

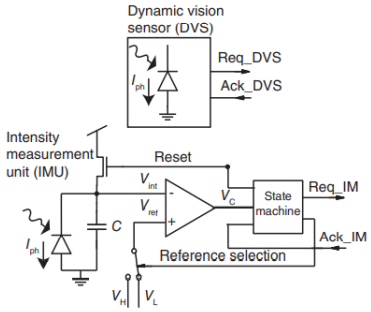

Figure 7. Abstracted ATIS Pixel [9]

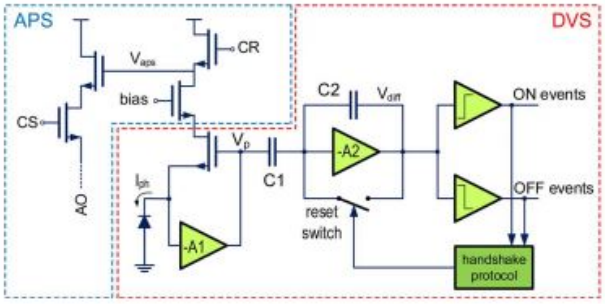

Figure 8. Abstracted DAVIS Pixel [2]

While the circuit design for each different commercial event-based sensor may vary, they are all capable of operating using a similar paradigm and are meant to model the biological retina. Figure 9 gives a comparison of some commercial and prototype event-based sensors available as of 2020.

	Supplier	iniVation			Prophesee				Samsung			CelePixel		Insightness
	Camera model	DVS128	DAVIS240	DAVIS346	ATIS	Gen3 CD	Gen3 ATIS	Gen 4 CD	DVS-Gen2	DVS-Gen3	DVS-Gen4	CeleX-IV	CeleX-V	Rino 3
Sensor specifications	Year, Reference	2008 [2]	2014 [4]	2017	2011 [3]	2017 [67]	2017 [67]	2020 [68]	2017 [5]	2018 [69]	2020 [39]	2017 [70]	2019 [71]	2018 [72]
	Resolution (pixels)	128 × 128	240 × 180	346 × 260	304 × 240	640 × 480	480 × 360	1280 × 720	640 × 480	640 × 480	1280 × 960	768 × 640	1280 × 800	320 × 262
	Latency (µs)	12μs @ 1klux	12μs @ 1klux	20	3	40 - 200	40 - 200	20 - 150	65 - 410	50	150	10	8	125μs @ 10lux
	Dynamic range (dB)	120	120	120	143	> 120	> 120	> 124	90	90	100	90	120	> 100
	Min. contrast sensitivity (%)	17	11	14.3 - 22.5	13	12	12	11	9	15	20	30	10	15
	Power consumption (mW)	23	5 - 14	10 - 170	50 - 175	36 - 95	25 - 87	32 - 84	27 - 50	40	130	-	400	20-70
	Chip size (mm^2)	6.3 × 6	5 × 5	8 × 6	9.9 × 8.2	9.6 × 7.2	9.6 × 7.2	6.22 × 3.5	8 × 5.8	8 × 5.8	8.4 × 7.6	15.5 × 15.8	14.3 × 11.6	5.3 × 5.3
	Pixel size (µm^2)	40 × 40	18.5 × 18.5	18.5 × 18.5	30 × 30	15 × 15	20 × 20	4.86 × 4.86	9 × 9	9 × 9	4.95 × 4.95	18 × 18	9.8 × 9.8	13 × 13
	Fill factor (%)	8.1	22	22	20	25	20	> 77	11	12	22	8.5	8	22
	Supply voltage (V)	3.3	1.8 & 3.3	1.8 & 3.3	1.8 & 3.3	1.8	1.8	1.1 & 2.5	1.2 & 2.8	1.2 & 2.8		1.8 & 3.3	1.2 & 2.5	1.8 & 3.3
	Stationary noise (ev/pix/s) at 25C	0.05	0.1	0.1	-	0.1	0.1	0.1	0.03	0.03		0.15	0.2	0.1
	CMOS technology (nm)	350	180	180	180	180	180	90	90	90	65/28	180	65	180
		2P4M	1P6M MIM	1P6M MIM	1P6M	1P6M CIS	1P6M CIS	BI CIS	1P5M BSI			1P6M CIS	CIS	1P6M CIS
	Grayscale output	no	yes	yes	yes	no	yes	no	no	no	no	yes	yes	yes
	Grayscale dynamic range (dB)	NA	55	56.7	130	NA	> 100	NA	NA	NA	NA	90	120	50
	Max. frame rate (fps)	NA	35	40	NA	NA	NA	NA	NA	NA	NA	50	100	30
Camera	Max. Bandwidth (Meps)	1	12	12	-	66	66	1066	300	600	1200	200	140	20
	Interface	USB 2	USB 2	USB 3		USB 3	USB 3	USB 3	USB 2	USB 3	USB 3			USB 2
	IMU output	no	1 kHz	1 kHz	no	1 kHz	1 kHz	no	no	1 kHz	no	no	no	1 kHz

Figure 9. Commercial and Prototype Event-Based Sensor Comparison [8]

2.2.3 Current Applications

As this technology continues to advance, more and more of these types of sensors will become available and have application in diverse problem sets and domains.

2.2.3.1 Feature Detection and Tracking

One of these problem sets is feature detection and tracking. Feature detection and tracking is used in many machine vision applications and algorithms to do this are rooted in frame-based camera technology. Therefore, although event-based sensors are well-suited for detection and tracking purposes due to their asynchronous low latency response times and high dynamic range, completely new processing algorithms are needed. One demonstration of a successful cluster tracking algorithm is shown by T.Delbruck and P. Lichtsteiner with their setup of a robotic goalie [10]. In this experiment shown in Figure 10, the robot uses event-based sensor data to prevent the "most threatening" (nearest) ball from entering a goal. The approaching balls are identified and tracked as 'clusters' based upon a pre-defined threshold number of events generated by the sensor. As the balls move, the location of the generated events moves, enabling the goalie to determine the position and velocity of the ball so it can be blocked. Overall, the goalie blocked 95 percent of the shots, thus proving that tracking algorithms can be used with event-based sensor data [10].

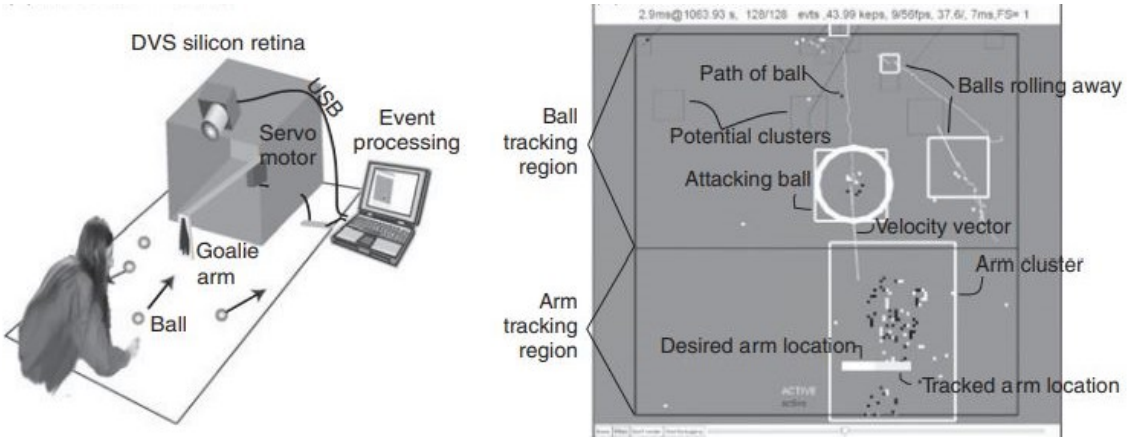

Figure 10. Robotic goalie tracking multiple balls with event-based data [7, 9, 10]

This is one example of a tracking algorithm that has been developed to work with event-based sensors, but there have been more examples of algorithm success. Similar blob/cluster tracking methods are used in traffic monitoring and surveillance [18, 19, 20] while more complex, user-defined shape tracking methods are used to follow human faces and bodies [8, 21]. With the maturation of event-based sensor technology, processing algorithms will also continue to mature and provide new opportunities for this type of sensor.

2.2.3.2 Space Domain Awareness

Event-based sensors also show promise for Space Domain Awareness (SDA). Space Domain Awareness, formerly known as Space Situational Awareness (SSA), refers to the detection, tracking, identification, and characterization/cataloging of resident space objects (RSOs). RSOs can range from space junk to operational satellites and SDA covers the surveillance of these objects from the low Earth orbit (LEO) regime to the geosynchronous orbit regime (GEO). SDA is currently maintained mainly through a combination of ground-based radar sensors and conventional optical imaging sensors. However, event-based sensors have been field tested to demonstrate their possibilities for use in this domain as well. In these tests, both the ATIS and DAVIS

were attached to the telescopes shown in Figure 11 and a series of experiments allowed observation of RSOs[11]. The starting location for pointing the telescope was established using a two-line element (TLE) from the NORAD space catalog of objects and previous research work on visualization, detection, and tracking enabled LEO and GEO RSOs to be observed and tracked at night and during the day [11]. Figure 12 displays a LEO object tracked at night and Figure 13 displays a GEO object tracked at night, where the blue represents events triggered first (events with an earlier timestamp) and the red represents events triggered last (events with a later timestamp).

Figure 11. Field telescopes for Testing [11]

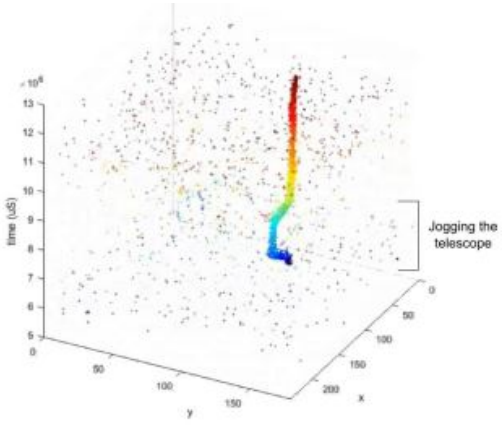

Figure 12. DAVIS Nocturnal Tracking of LEO Object [7, 11]

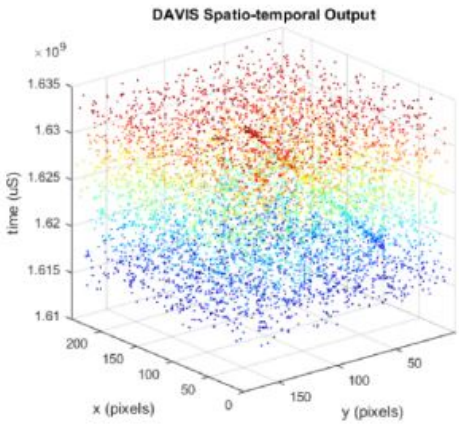

Figure 13. DAVIS Nocturnal Tracking of GEO Object [7, 11]

This testing displays a unique approach to SDA and reveals the possibilities especially for daytime space object detection and imaging of fast-moving space objects. Already, additional research is looking at detection and tracking algorithms for space domain awareness and future work should continue to expand upon this application for the sensors [22].

2.2.3.3 AFIT and USAFA Research

The Air Force Institute of Technology (AFIT) and the U.S. Air Force Academy (USAFA) have also been researching neuromorphic vision sensors for defense applications. Some examples include the thesis work of McReynolds and Boettiger. In his thesis, McReynolds characterizes neuromorphic imagers by identifying five critical parameters and creating a physics-based model detailing noise and frequency response parameters. His work expands on the limitations and performance of event-based vision sensors with the hope of using the new imaging concept for Intelligence, Surveillance, and Reconnaissance (ISR) platforms in the future [4]. In Boettinger's thesis, he focuses on object detection and tracking, considering event-based output as both pseudo frames and individual filtered asynchronous events to do event-based detection and tracking. Although his work doesn't show a viable event-based detection and tracking algorithm solution to replace framed-based algorithms, it does show the advantages of using event-based technology to do object detection and tracking. This further opens the door for additional event-based object detect and tracking algorithm development and exploration of the technology for defense applications. [7]. Additionally, the Physics Department at the U.S. Air Force Academy is working toward the launch of their Falcon Neuro CubeSat. The CubeSat contains an event-based sensor as part of its payload with a research goal of observing target backgrounds from space (i.e. sun, moon, city lights, stars, lightning, sprites) and

characterizing event-rates and dynamic range as a result [23]. The research being done by AFIT and USAFA show the increasing interest of the Department of Defense and U.S. Air Force in neuromorphic vision technology and the desire to expand its use in the defense domain.

2.3 Environmental Conditions affecting Space Electronics

Space payloads undergo a harsh environment. These payloads, comprised of electronics and sensors, must handle conditions that include the intense vibration of launch, the thermal cycles experienced in orbit, the low pressure vacuum of space, and the hazardous effects of radiation. This section focuses on the environmental conditions impacting space electronics and sensors from launch to LEO (200km-1000km) [24].

2.3.1 Vibration

The first condition that space electronics need to survive is vibration. Vibration during launch can cause damage to a satellite payload due to the large magnitude of loading that the satellite experiences during this time. Vibration can also cause damage to a satellite if the natural frequency modes of the satellite match those of the launch vehicle. Issues specific to electronics typically arise during launch, rocket stage separation, and satellite ejection because of pyrotechnic shock. Pyrotechnic shock is a dynamic structural shock that comes from a "high frequency, high magnitude stress wave propagating through the structure as a result of an explosive charge" [25]. The shock can cause damage to sensors and electronics, resulting in problems such as electrical circuit shorts and the loss of functional sensors.

2.3.2 Thermal Vacuum

Space electronics and sensors also need to survive the large temperature fluctuations and the high vacuum environment of space. Temperature fluctuations occur due to a satellite's orbit around Earth where it is exposed to both direct sunlight and complete darkness (eclipse). Although dependent upon position, material, and internal components, nominal cyclical temperature variations of a satellite can range from -120 C to +120 C [24]. Additionally, the vacuum of space results in pressures of 10^{-6} to 10^{-9} Torr [24], making radiation the main heat transfer mechanism in space. These extreme conditions can lead to issues with sensor functionality and circuit operation.

One of these issues is tin or metal whiskers, thin conductive crystalline structures which can grow on electrical devices or surfaces finished with tin [25]. Tin, zinc, and cadmium, are examples of materials that have displayed evidence of the growth of whiskers. It can take minutes to decades for whiskers to form [26], but with a low electrical resistance and the ability to carry current, whiskers can cause electrical shorts for circuits.

Another issue is outgassing, the release of gases or vapors that were trapped/dissolved in a material [27]. Outgassing in space can occur with adhesives, glues, and plastics and results in a cloud of contaminants. Contaminants can cause degradation of optics and sensors as well as build up of electrostatic discharge (ESD). ESD is the build up of energy from the space environment which can lead to charging and discharging, damaging space electronics.

Finally, issues arise with sensor performance and operation due to the extreme temperatures and thermal cycles in space. Space electronics experience periods of sustained high temperatures. High temperatures result in thermal noise which degrade the performance of the sensor and can lead to electronic failures from overheating [28]. Likewise, extremely cold temperatures can impact electronic devices. Cold tem-

peratures cause changes in the resistance and capacitance on integrated circuits [29], causing trouble with operation. Thermal cycling can also cause problems with sensors and electronics as materials expand and contract [29]. Not only do the extreme temperature conditions and thermal cycles of space impact the operation and performance of electronics, but they can reduce the lifespan and reliability of the devices as well.

2.3.3 Radiation

Radiation is another harmful condition that LEO space hardware needs to survive. In low earth orbit, radiation comes from transient radiation and trapped particles [27]. Transient radiation includes Galactic Cosmic Rays (GCRs) and solar particles from coronal mass ejections (CMEs) and solar flares. Trapped particles include electrons, protons, and heavy ions [27] and reside in the Van Allen belts. In LEO, the inner Van Allen belt area of concern is called the South Atlantic Anomaly (SAA). The SAA is an area where Earth's magnetic field dips, leading to an increased flux of energetic particles in the area. Transient and trapped particle radiation can lead to satellite charging, single event effects (SEEs), and ionizing/non-ionizing dose effects [30] - all of which can damage space electronics and sensors. Ionizing and non-ionizing dose effects can degrade microelectronics and optical components. Single event effects can cause noisy images, data corruption, circuit damage, or complete system failure [30]. Although radiation can damage electronics and sensors, small satellites (i.e. CubeSats) in LEO typically do not undergo radiation testing. This is because small satellites are designed to be cheaper and have a shorter lifespan.

2.4 Space Applications

Current applications of event-based vision sensors were discussed in section 2.2.3. This section gives insight into future defense applications for the sensor. Event-based vision sensors are being used for ground-based SDA and this section identifies the potential benefits of using the technology for space-based SDA. It specifically looks at the advantage of placing the event-based sensor in LEO orbit to observe GEO satellites.

2.4.1 Space-Based Space Domain Awareness

Space-based satellites, like the U.S. Air Force's Space-Based Surveillance System (SBSS), a LEO satellite, exist to support ground-based SDA systems by detecting, tracking, identifying, and characterizing RSOs. Operating from space allows SDA satellites to avoid problems typically seen with ground-based sensors. For example, current ground-based systems have issues with daytime observations of GEO satellites. Specifically, ground-based systems are unable to observe bright targets at GEO within a six hour window centered on local sun position [31]. Space-based SDA satellites can alleviate this issue by providing observations of GEO targets during the day. However, even space-based satellites have SDA limitations. One significant limitation is known as the solar exclusion gap [31]. This refers to the coverage gap that occurs when a GEO satellite passes in front of the Sun. This coverage gap exists because optical sensors have solar exclusion angles, angles at which the Sun is too close to the camera's line of sight, thus preventing the camera from seeing the target object [31].

Event-based vision sensors can potentially resolve this coverage gap, with the ability to detect only changes in brightness (the log intensity of light) and therefore avoid saturation. Traditional CCD or CMOS sensors either saturate from too much light during exposure or are unable to detect an object because of low contrast. However,

event-based sensors have a higher dynamic range and only pick up changes in brightness, allowing them to operate in more diverse lighting environments. Therefore, event-based sensors will not saturate when pointed at the Sun and are more likely to detect scene dynamics in lower contrast environments than conventional cameras. This opens up the possibility that event-based sensors could be used to detect both dark and bright objects passing in front of the Sun.

With more than 20,000 pieces of debris in space and space now considered a warfighting domain, filling coverage gaps within SDA is more important than ever. Event-based vision sensors integrated onto small LEO satellites may be a solution.

2.5 Summary

This chapter discussed event-based vision sensors, focusing on how the dynamic vision sensor pixel operates and how it is being used today. It covered environmental conditions affecting electronics and sensor operation during both LEO and launch. Finally, it described a potential mission set for event-based vision sensors on LEO SDA satellites. The topics discussed in Chapter II are meant to give background and context for the research, serving as the foundation for designing the test plans and objectives outlined in Chapter III. Chapter III gives more details about each of the testing setups, which ultimately are used to assess the viability of event-based sensors on small satellites.

III. Methodology

This chapter is broken up into four sections. It discusses the testing hardware and software, the survivability experiments, the demonstration application experiments, and the analysis methodology for the collected data. The survivability and application demonstration experiments detail any testing assumptions, the objectives for the tests, and the test setups and plans.

3.1 Testing Hardware and Software

All experiments in this research use the DVS240C by iniVation. The DVS240C is capable of outputting both event data and frame data; however, it cannot do both simultaneously. It has a 240 x 180 focal plane array with 18.5 micrometer^2 pixels. It uses a USB 3.0 connection for power and data, and is capable of fitting a CS-mount lens. Specifications for this device are found in Figures 14 and 15. The camera connects to Dynamic Vision (DV) software to display its event or frame output. The DV software uses a custom Address Event DATa (AEDAT) format for event data and contains several pre-built software modules for easy data conversion and filtering [32].

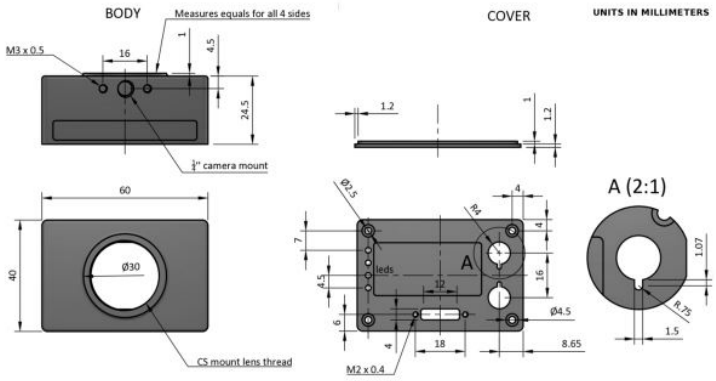

Figure 14. DVS240 Physical Dimensions [12]

inivation

DVS 240

The DVS 240 is a 240 x 180 pixels DVS event camera with USB 3.0 interface.

Specifications

DVS Resolution	240 x 180 pixels
Frame Resolution	240 x 180 pixels, Grayscale, calibration mode only
DVS Dynamic range	120 dB
Min. latency	~ 12 us @ 1 klux with optimized biases
Lens mount	CS-mount
Connectors / Power	USB 3.0 micro
Bandwidth	12 MEvents / second
Software	DV-Platform
Power consumption	< 180mA @ 5V DC
Dimensions	H 40 x W 60 x D 25 [mm]
Weight	75g (without lens)
Hardware multi-camera sync	Supported (HiRose Connector)
IMU	6-Axis Built-in
Case	Machined polycarbonate, 4 mounting points
Tripod mount	Whitworth ¼" female
APS Frame Shutter	Configurable, Global or Rolling Shutter
CMOS Technology	0.18 um 1P6M MIM CIS
Chip size	5 x 5 [mm]
Pixel size	18.5 x 18.5 [um]
Array size	3.33 x 4.44 [mm]
Fill factor	22 %
Pixel complexity	48 transistors, 2 capacitors, 1 photodiode with micro-lens
Chip voltages	1.8 V and 3.3 V
Chip power consumption	5-14mW (activity dependent)

Specifications not guaranteed. All specifications subject to change without notice

Figure 15. DVS240 Specifications [12]

The lens used in survivability testing is the 'SkyPad' lens. It is an AFIT custom made lens and baffle design for a star tracker camera payload. It has a fixed focal length of 8 mm and uses a 3D printed baffle to hold the lenses in place. The SkyPad lens has already been through thermal vacuum (TVAC) bake-out and testing, therefore its use reduces the number of possible failure points for the survivability testing of the DVS240C. Figure 16 is an image of the SkyPad lens attached to the DVS240C.

Figure 16. SkyPad Lens on DVS240C

3.2 Survivability Testing

This research first looks at the survivability of the DVS240C, focusing on vacuum, thermal vacuum, and vibration testing of the sensor. Testing is executed at a subsystem developmental level to gather early evaluation data and reduce the risk for future payload integration. In vibration and vacuum testing, the DVS240C is put through simulated environments similar to the conditions of launch and low Earth orbit.

3.2.1 Vacuum Tests

AFIT's TVAC chamber is used in these experiments to simulate the vacuum of space in LEO. The AFIT TVAC chamber is made by Abbess Instruments and is capable of pumping the vacuum chamber to a pressure as low as 10^{-6} Torr [33]. In these experiments, pressures around 10^{-3} Torr are used to simulate the low earth environment. Qualification of space electronics is outlined in the Space and Missile Systems Standard document, SMC-S-016, and requires testing vacuum pressures of at least 10^{-4} Torr [13]. Since the purpose of testing is to gather early evaluation data of the sensor system, slightly higher pressures of 10^{-3} are still sufficient to simulate LEO conditions and look at sensor performance. Throughout the vacuum testing, temper-

ature remains ambient. Only vacuum survivability of the DVS240C is considered in order to isolate any issues that may occur during the testing.

3.2.1.1 Objectives

The main objective of these tests is to determine if the DVS240C can survive vacuum pressures as low as 10^{-3} Torr without degrading performance of the sensor. Testing is considered a success if the sensor performs at the same level in pre-vacuum, in-vacuum, and post-vacuum functionality tests. If the DVS240C is unable to operate or displays significantly degraded performance, the DVS240C is considered unable to survive the vacuum environment of LEO as a standalone COTS product. A secondary objective of testing is to establish procedures and guidelines for environmental testing of an event-based sensor.

3.2.1.2 Testing Setup and Plan

The DVS240C vacuum tests use a custom made bracket shown in Appendix A which allows the DVS240C to be attached at one end with a black aluminum box at the other. The black box contains an light emitting diode (LED) connected to a blinking circuit through a DB-9 connector. The blinking circuit is located outside of the vacuum chamber and is programmed to blink the LED at 2 Hz using a 9 Volt power source. The black aluminum box contains 0.40mm diameter holes to allow light to escape and gives a recognizable pattern for the event-based sensor as shown in Figure 18. Additionally, the test stand enables the distance between the black aluminum box and the DVS240C to be adjustable. Finally, a thermocouple is placed on the DVS240 processing chip in order to obtain temperature data on the DVS240C throughout the vacuum test and ensure temperatures do not reach higher than 85 degrees Celsius, the previously tested operational temperatures for the system [34].

Figure 17 is a diagram of the vacuum testing setup and Figure 20 shows the placement of the thermocouple on the DVS240C.

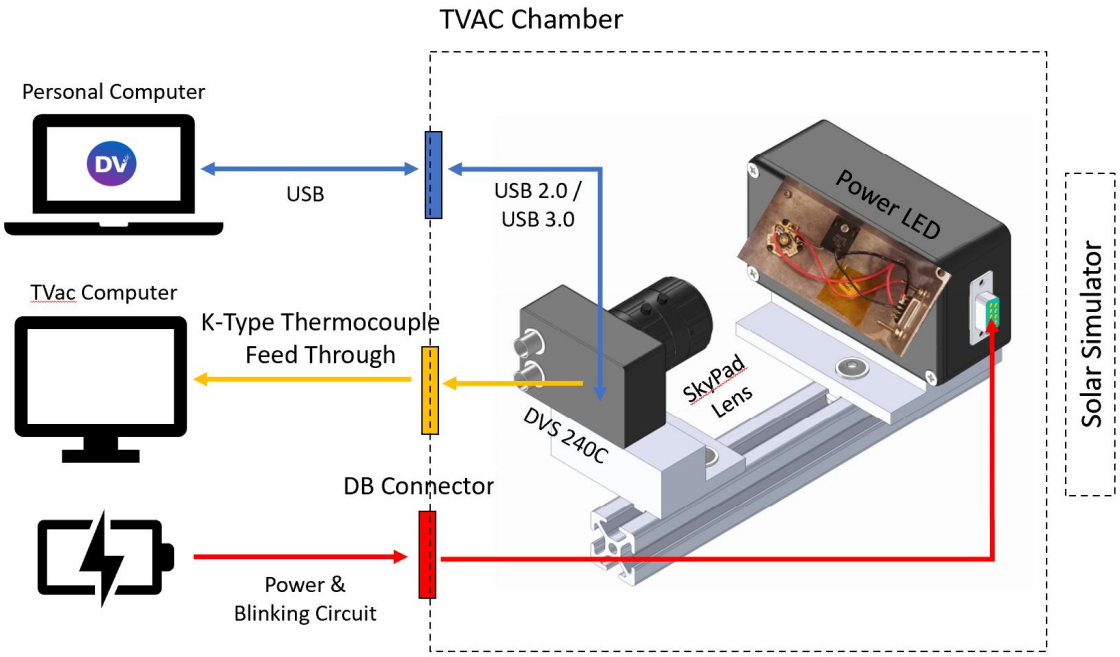

Figure 17. Vacuum Testing Setup Diagram

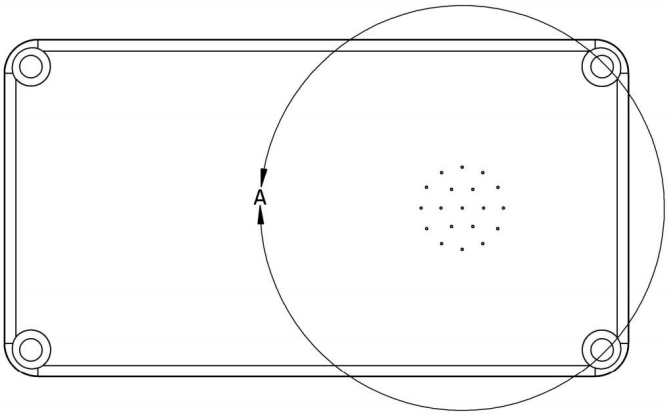

Figure 18. Black Aluminum Box Front Hole Pattern

The DVS240C vacuum test setup in Figure 17 is designed to allow functional testing of the event-based camera system. A conventional camera takes images of

stationary scenes and compares quality to look at degradation of performance. However, event-based sensors do not output any data if nothing is changing in the sensor's field of view. Therefore, to ensure event-based sensor functionality, the scene in the sensor's field of view needs to be changing. The vacuum tests use the blinking LED to create scene dynamics without moving parts. Figure 19 shows images of the testing setup. Table 1 gives the five steps required to do functional testing and data capture for the vacuum tests. Functionality testing involves a visual check of DVS240C event output with the DV software as well as event data capture for subsequent quantitative analysis. The quantitative analysis is used to more accurately characterize the sensor's ability to survive vacuum without degraded performance.

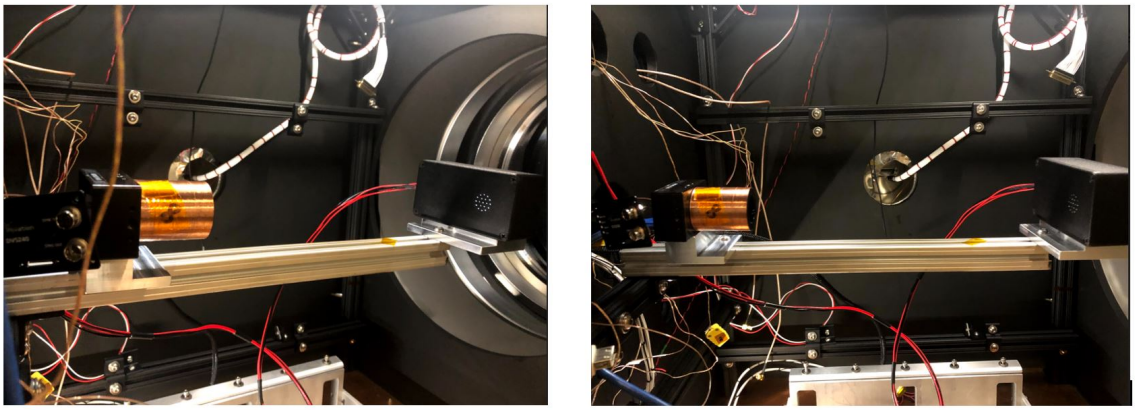

Figure 19. TVAC Testing Setup

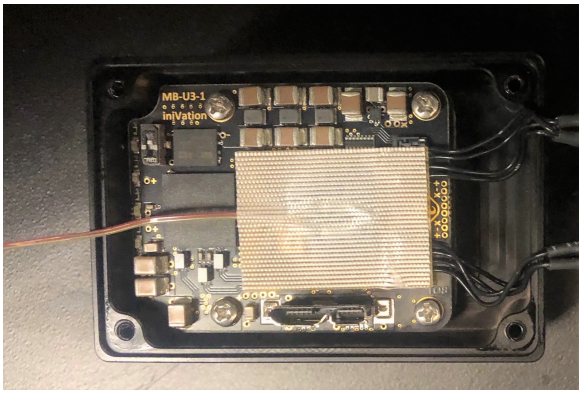

Figure 20. Thermocouple 1 Placement on DVS240C

Table 1. Vacuum Testing Data Capture and Functional Check

Step	Action
1	Turn on DVS240C.
2	Turn on LED blink circuit.
3	Open DVS software.
4	Record event data for 30 seconds (x2).

The vacuum testing procedure is outlined in the flow diagram in Figure 21. Functional check and data collection occurs at a normal atmospheric pressure of approximately 740 Torr in pre- and post- pump down and at LEO pressures of about 10^{-3} Torr in vacuum. The data collected from the thermocouple, TVAC chamber, and sensor functionality tests are used to analyze the DVS240C's ability to survive the LEO vacuum environment and the work is presented in Chapter IV.

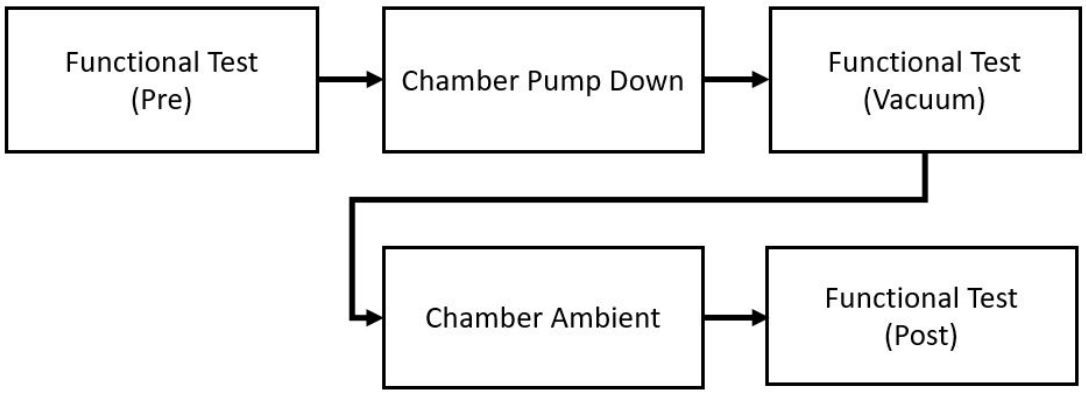

Figure 21. Vacuum Test Plan Flow Diagram

3.2.2 Thermal Vacuum Tests

AFIT's TVAC chamber is also used to execute the thermal vacuum tests. In these tests, the LEO thermal vacuum environment is simulated by bringing the DVS240C to

10^{-4} Torr and then cycling through hot and cold temperature extremes. The thermal cycling simulates the temperature extremes the system feels in LEO from exposure to total sunlight and complete eclipse. Since no mission exists for the subsystem, the hot and cold testing temperature extremes are derived from the SMC-S-016 electronics acceptability test requirements. Additionally, the DVS240C is not fully temperature certified and therefore there are no operational temperature range specifications for the system. The DVS240C temperature range monitored throughout testing is based on [34]. Testing focuses on early collection of survivability data for the DVS240C, therefore additional thermal vacuum testing is needed in order to qualify the hardware for space. Testing and analysis concentrates on the DVS240C sensor rather than the COTS product as a whole which has a polycarbonate case and is susceptible to material expansion and contraction upon thermal cycling.

3.2.2.1 Objectives

The main objective of the thermal vacuum tests is to determine if the DVS240C can survive and operate at temperature ranges of -24 to 61°C (SMC minimum required temperature for electronic unit subsystems [13]) without performance degradation. Survivability testing is a success if the DVS240C performs similarly before and after thermal cycle testing, and if the system is able to execute functional tests throughout. If the DVS240C is unable to operate from -24 to 61°C or displays significantly degraded performance after the thermal cycle testing, the DVS240C is considered unable to survive the thermal vacuum environment of LEO as a standalone COTS product. A secondary objective of testing is to establish procedures and guidelines for environmental testing of an event-based sensor.

3.2.2.2 Testing Setup and Plan

The thermal vacuum tests use the TVAC setup described in section 3.2.1.2 and shown in Figure 17. Three thermocouples are placed on the DVS240C and one is placed on a plate in the TVAC chamber. The first thermocouple is placed on the back of the DVS240C processing chip (1), the second is placed on the side of the DVS240C (2), the third is placed on the back of the black aluminum box (3), and the fourth is placed on the plate at the bottom of the TVAC chamber (4). Images of the thermocouple placement are shown in Figures 20, 22, 23, and 24 respectively.

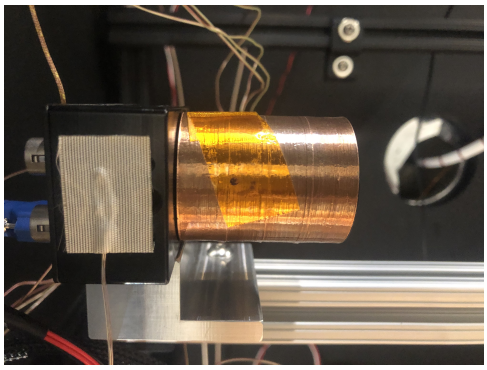

Figure 22. Thermocouple 2 Placement on DVS240C Side

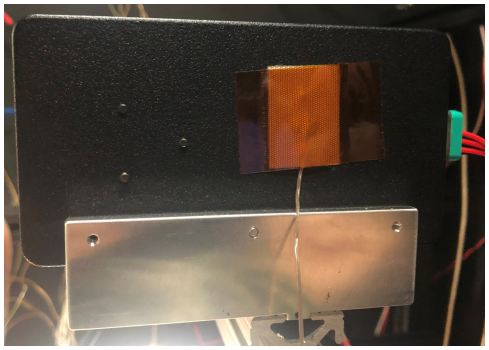

Figure 23. Thermocouple 3 Placement on Black Aluminum Box Back

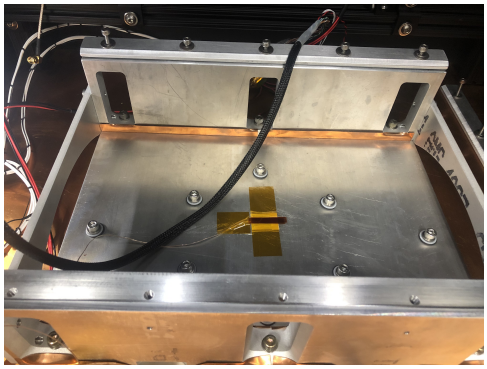

Figure 24. Thermocouple 4 Placement on Plate

Thermocouples 2 and 4 serve as the controls for this survivability testing and will be monitored to achieve the temperature testing profile seen in Figure 25. Thermocouple 1 serves to monitor the operational temperature of the system and if DVS240C

CPU reaches temperatures above 85°C, the system will be turned off. No functional tests will be executed with CPU operational temperatures greater than 85°C in order to avoid overheating and damage to the DVS240C.

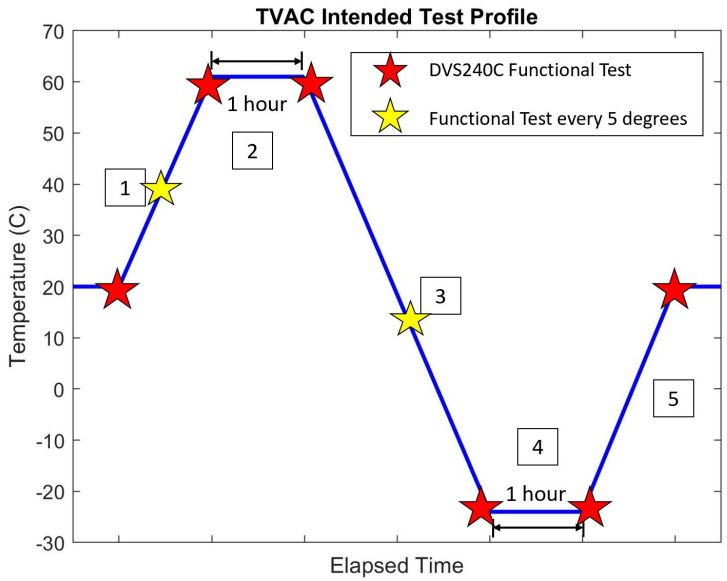

Figure 25. Thermal Vacuum Intended Test Profile

The testing profile seen in Figure 25 includes five phases which begin after the DVS240C has been brought to a pressure of 10^{-3} Torr. In the first phase, the chamber temperature is increased until thermocouple 2 reaches 61°C followed by a 'hot dwell' of 1 hour with the DVS240C turned off in Phase 2. In Phase 3, the chamber temperature is decreased until thermocouple 2 reaches -24°C followed by a 'cold dwell' of 1 hour with the DVS240C turned off in Phase 4. Finally, Phase 5 returns the DVS240C to ambient temperature of approximatly 20°C.

The dwells seen in Phase 2 and 4 allow for testing the DVS240C's 'hot starts' and 'cold starts.' The stars on Figure 25 indicate DVS240C functional tests. The functional test is the same process outlined in Table 1. Functional testing involves doing a visual check of DVS240C event output with the DV software as well as event data capture for subsequent quantitative analysis. The quantitative analysis is used to

more accurately characterize the sensor's ability to survive thermal vacuum without degraded performance and to characterize the sensor's performance throughout its operational temperature range. During Phases 1 and 3 of thermal vacuum testing, functional tests are executed for every five degree temperature change in order to monitor any issues or anomalies while approaching the temperature extremes. The data collected from the thermocouples, TVAC chamber, and sensor functionality tests are used to analyze the DVS240C's ability to survive and perform in the LEO thermal vacuum environment and the work is presented in Chapter IV.

3.2.3 Vibration Tests

In the vibration tests, AFIT's shaker table is used to simulate the vibration a satellite system or subsystem experiences during launch. Low-level sine sweep testing characterizes the DVS240C natural modes of vibration and ensures the camera subsystem's health after random vibration testing through response spectrum comparison. Random vibration testing is used to simulate the conditions the DVS240C experiences during liftoff and ascent. The vibration tests are developmental subsystem level tests and the 2014 Space and Missile Systems Center (SMC) Standard Test Requirements Document [13] determines the vibration parameters for the testing. Testing and analysis is focused on the survivability of the DVS240 sensor.

3.2.3.1 Objectives

The main objective of these tests is to determine if the DVS240C can survive random vibration testing without degrading performance of the sensor. Testing is a success if the sensor performs at the same level after random vibration testing for all subsystem axes and displays the same natural frequency vibration modes before and after random vibration testing. The natural frequency modes for pre- and post- sine

sweep testing must have no greater than a 5 percent difference in acceleration and a 10 percent difference in frequency to be considered the 'same' [35]. If the DVS240C is unable to operate or displays significantly degraded performance after any of the vibration testing, the DVS240C is considered unable to survive the launch environment as a standalone COTS product without modification. A secondary objective of testing is to establish procedures and guidelines for environmental testing of an event-based sensor.

3.2.3.2 Testing Setup and Plan

The DVS240C vibration tests use a custom made bracket shown in Appendix B which allows the DVS240 to be securely attached to the shaker table with access the camera system's ports. This setup allows for easy reconfiguration of the DVS240C on the shaker table to test all three axes. Figure 27 shows the testing setup on the shaker table. The SkyPad lens is attached after vibration testing is executed in order to execute a functional test. The lens is not attached throughout the duration of the vibration testing. The same LED black box setup seen in Figure 26 is used for functional testing, enabling the DVS240C to have consistent alignment, lighting, and distance settings for data comparison between tests.

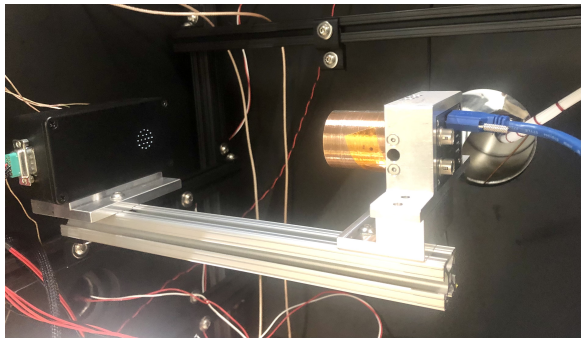

Figure 26. Pre and Post Vibration Functional Testing Setup

Single-axis accelerometers are placed on the side (1), front (2), and top (3) of the the DVS240C as shown in Figure 28 in order to gather vibration data. Accelerometer 1 measures acceleration in the X direction, accelerometer 2 measures acceleration in the Y direction, and accelerometer 3 measures acceleration in the Z direction.

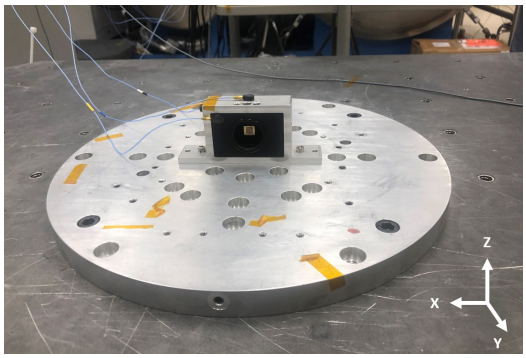

Figure 27. Vibration Testing Setup - DVS240C attached to AFIT Shaker Table for axis vibration

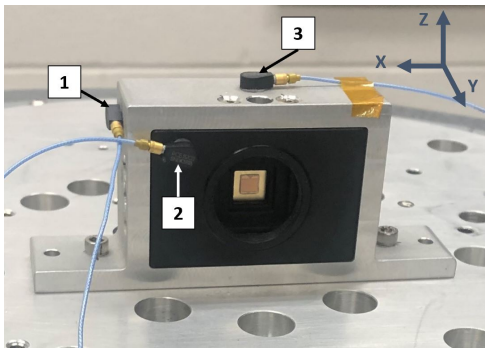

Figure 28. Accelerometer Placement on DVS240C

Figure 29 is a flow diagram of the vibration testing process for a single axis. Functional tests are run before and after all vibration testing to capture DVS240C performance data and ensure the system is still operating nominally after testing each axis. Low-level sine sweep tests are used before and after random vibration testing to ensure natural frequency modes remain the same. Visual comparison of the sine sweep data ensures there is no damage to the DVS240C. If the system does not show nominal performance after a given random vibration test, the testing will be stopped to prevent further damage to the sensor.

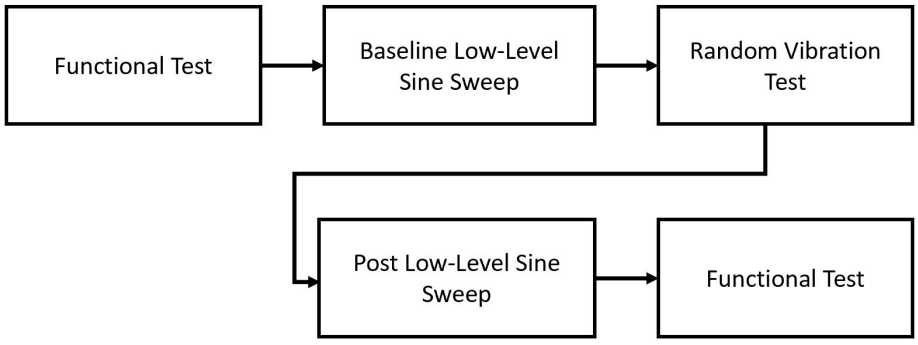

Figure 29. Vibration Test Plan Flow Diagram for Single Axis

The vibration functional test steps are outlined in Table 2 and are similar to those executed in TVAC testing. The functional test includes a visual check of DVS240C event and frame output with the DV software as well as data capture for subsequent quantitative analysis. The quantitative analysis is used to more accurately characterize the sensor's ability to survive vibration without degraded performance.

Table 2. Vibration Testing Data Capture and Functional Check

Step	Action
1	Attach lens to DVS240C (if not already attached).
2	Attach black box with LED to vibration mount.
3	Turn on LED blink circuit.
4	Open DVS software.
5	Record event data for 30 seconds (x2).

The sine sweep test profile can be seen in Table 3. It uses a low acceleration value 0.5 g and sweeps across a frequency range of 20-2000 Hz at a 4 octaves/minute rate. The random vibration test profile parameters can be seen in Table 4 and Figure 30. Random vibration testing lasts a duration of 1 minute for each DVS240C axis with

the power spectral density values corresponding to vibration frequency based upon the testing spectrum shown in Figure 30.

Table 3. Sine Sweep Vibration Test Parameters

Test Parameter	Value
Frequency Range	20-2000 Hz
Acceleration	0.5 g
Sweep Rate	4 octaves/min

Table 4. Random Vibration Test Parameters

Test Parameter	Value
Frequency Range	20-2000 Hz
Acceleration	6.958 G_{RMS}
Test Duration	1 min/axis

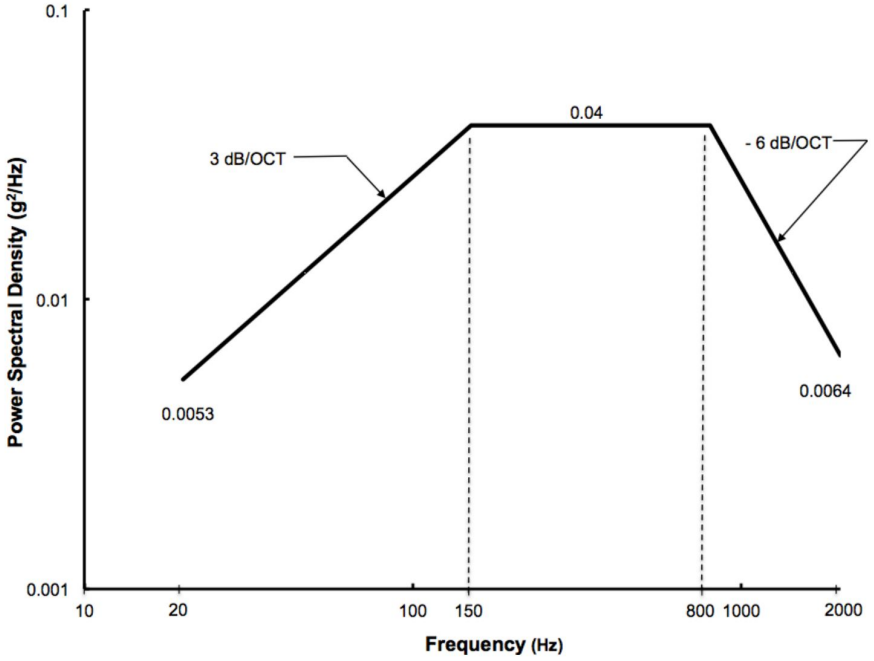

Figure 30. Minimum Unit Random Vibration Acceptance Testing Spectrum [13]

Overall G_{RMS} values for each axis of random vibration will be reported. Additionally, data collected from the accelerometers and sensor functional tests are used to analyze the DVS240C's ability to survive launch and the work is presented in Chapter IV.

3.3 Application Demonstration

This research also considers space mission set applications for the DVS240C event-based sensor through a series of application demonstration tests. The application demonstration tests aim to support the viability of event-based technology in space by showing feasible uses for the sensor technology in the area of space-based SDA.

3.3.1 Space-Based Space Domain Awareness Tests

The space-based SDA tests use AFIT's solar simulator to simulate sun illumination conditions in LEO. The solar simulator is a 12 inch x 12 inch assembly which uses 1.6kW arc lamp to emit three degree collimated light in horizontal beams [33]. The solar simulator is integrated into AFIT's chamber, however the SDA tests occur at ambient pressure and temperature. The sensitivity of the DVS240C can be changed to increase or decrease the number of events generated, but the SDA tests were run with the 'bias' settings at preset manufacturer settings.

3.3.1.1 Objectives

The main objective of these tests is to demonstrate that the DVS240C can detect and observe both bright and dark objects within standard camera solar exclusion angles (0-30 degrees). Testing is a success if the DVS240C does not saturate when pointed directly at the solar simulator and is able to detect the presence of the bright or dark object at the various angles. If the DVS240C is unable to detect objects in front of the solar simulator, the DVS240C is considered unsuitable for this space-based SDA application using its manufacturer preset sensitivity settings. The experiments also assess the extent of detection picked up by the DVS240C at each 10 degree interval.

3.3.1.2 Testing Setup and Plan

Two test setups are used for the space-based SDA demonstration tests. The first setup, previously used in TVAC testing, is shown in Figure 19. In this experiment, the blinking LED light is used to replicate a bright object ('target') in front of the Sun. The second setup, shown in Figure 32, is used to replicate a dark object ('target') in front of the sun. In the dark object test setup, a fan (with its blades taped back) is programmed to rotate. A black oval is taped to the center of the fan and the set-up is used as the 'dark object' and can be seen in Figure 31.

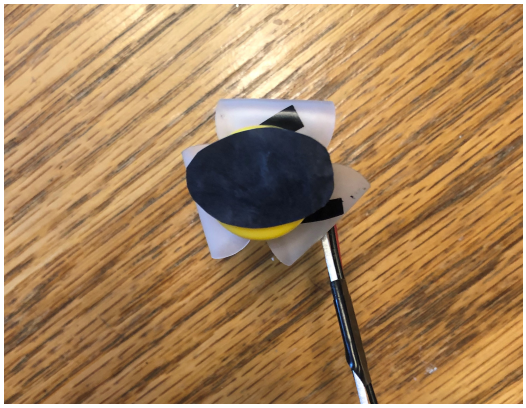

Figure 31. Dark Object - Black oval on rotating fan with blades taped back

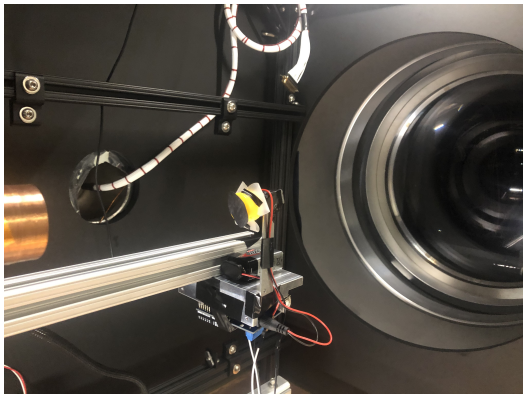

Figure 32. Dark Object Testing Set-Up in TVAC

The bright and dark object detection tests use scene dynamics to generate events and both follow the same procedure. Using the set-up in Figure 33, DVS240C event data capture occurs four times at 0, 10, 20, and 30 degree angles to the solar simulator. The red stars in Figure 33 indicate the data capture locations. With each ten degree angle change, the entire camera, bracket, and target assembly rotates as a unit. This ensures consistent target alignment with DVS240C while the angle relative to the solar simulator changes.

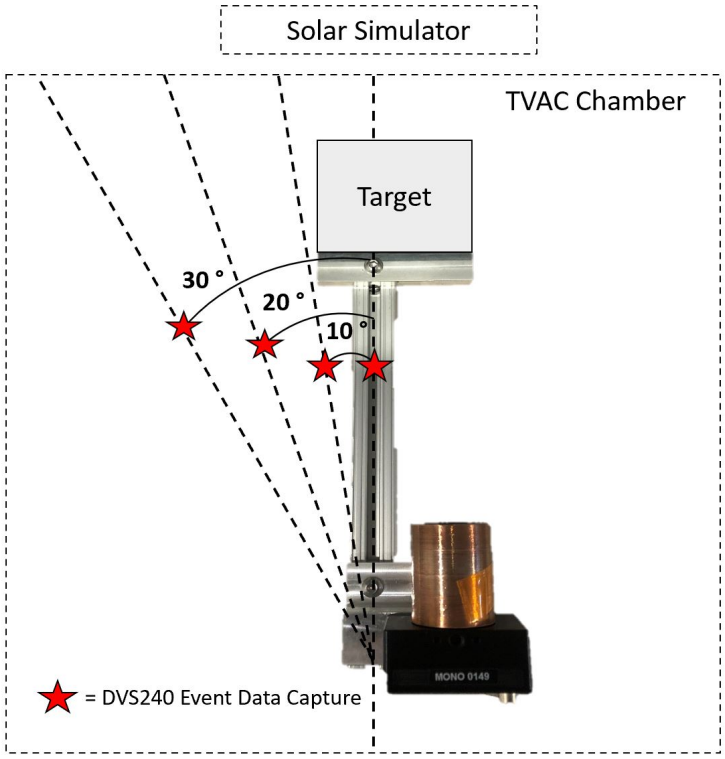

Figure 33. Space-based SDA Testing Setup

Test data collected from DVS240C will be used to show the viability of using this event-based camera system for space-based SDA to detect objects in front of and near the Sun. Analysis of the collected event data will be discussed in Chapter IV.

3.4 Data Analysis Methodology

The analysis method for this research is based on the work by Boettiger [7]. Boettiger uses Fourier analysis to look at the DAVIS 240C bandwidth capacity by observing the sensor's ability to respond to rapidly changing stimulus. He shows that the DAVIS 240C can detect frequencies up to 5000 Hz and also notes that as the frequency of the stimulus increases, less pixels are able to detect the stimulus (increased noise floor and decreased signal magnitude) [7].

Figure 34 shows a schematic of the process used in this thesis to translate the DVS240C captured event stream into time domain and frequency domain information. First, the captured event stream of AER data is mapped to a discrete time vector to create a time-pixel matrix. Since an event-based sensor outputs asynchronous data, the time between triggered AER 'events' is variable and there is no constant output or sampling rate. Therefore, in order to do a Fourier analysis, the data must be mapped to a time vector with a equally spaced samples. This discrete time vector is populated with microsecond timesteps due to the microsecond time resolution capabilities of the camera system. As the captured event stream gets mapped to the time vector through its timestamps, only the polarity component of each pixel's AER data is saved. This ultimately creates a time-pixel matrix composed of polarity information for every pixel of interest with microsecond resolution. All 'ON' events are indicated with a '1' for polarity and all 'OFF' events are indicated with a '-1' for polarity. If no event was generated for the timestamp, it is indicated with a '0.' Next the time-pixel matrix is translated into a mapped event vector by doing a summation for every timestep in the time-pixel matrix - if there are multiple AER events with the same timestep, they are added. For example, if three pixels generate 'OFF' events at the same time, the mapped event vector contains a '-3' for that timestep. The mapped event vector represents the discrete time domain signal of the DVS240C, where the magnitude of the vector indicates the accumulation of polarity events for the pixel(s) of interest. Finally, the mapped event vector or discrete time signal is translated to the frequency domain using Matlab's fast Fourier transform (FFT). Since the size of the data is not an integer power of 2 data points (2^n) in size, Matlab's FFT function uses the discrete Fourier transform (DFT) of a vector to translate the data into the frequency domain[36]. Taking the fourier transform of the mapped event vector computes the Fourier coefficients which are the weighted complex numbers

that represent the combination of harmonically related sinusoids for the signal. The final plot of the data in the frequency domain is a semi-logarithmic graph derived from plotting the magnitude of the Fourier coefficients and half of the signal sampling frequency. With the frequency domain plot, it is much easier to see the frequency content of the signal.

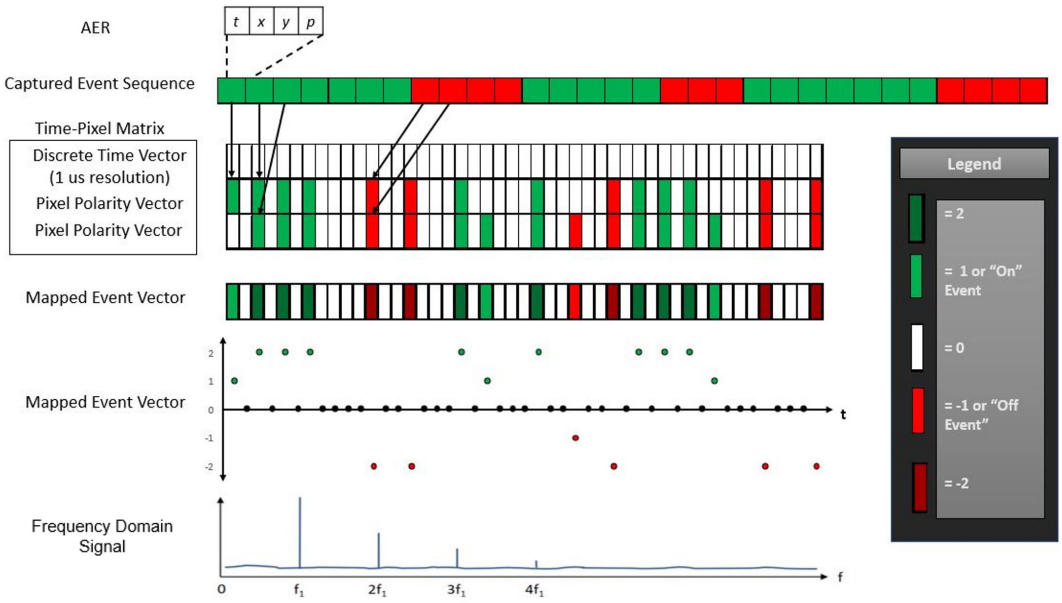

Figure 34. Fourier Analysis Method Diagram for Event Data [7]

3.5 Summary

This chapter outlined the hardware and software used throughout testing. It discussed the objectives, setups, and test plans for all survivability testing and application demonstration testing. Survivability testing is meant to assess the ability of the DVS240C to survive launch and low earth orbit conditions and determine the feasibility for using the system in space. The survivability testing encompasses vacuum testing to pressures of 10^{-3} Torr, thermal vacuum testing at 10^{-4} Torr for temperature ranges -24 to 61°C, and random vibration testing for 20-2000 Hz frequencies. Application demonstration testing is meant to provide a defense use of the DVS240C

in space and covers applications in space-based space domain awareness with detection of light and dark objects in front of the sun. Finally, Chapter III discussed the asynchronous Fourier analysis methodology the research uses for analyzing event test data. Chapter IV details test results of testing, ultimately determining event-based vision sensor viability for future satellite use.

IV. Results and Analysis

4.1 Overview

Chapter IV discusses the results of the survivability tests and demonstration of SDA application for the DVS240C. It begins with an examination of the vacuum testing and thermal vacuum testing results to determine DVS240 operability in low earth orbit conditions. Next, the chapter discusses vibration testing results to assess if the DVS240C can survive launch conditions without degrading sensor performance. Finally, this chapter explores SDA by observing the DVS240C operation in sunlight conditions to investigate a possible advantage for use of the sensor on space-based platforms.

4.2 Survivability Testing

4.2.1 Vacuum Tests

The results of vacuum testing show that the DVS240C is able to survive low pressures around 10^{-3} Torr without degraded performance and maintains performance at 10^{-3} Torr pressure levels. Figure 35 displays the nominal vacuum pressure profile for each of the executed tests. It takes approximately 45 minutes for AFIT's chamber to reach 10^{-3} pressure and approximately 10 minutes to pump up to ambient pressure. The large dip in pressure, marked with a blue star on the graph, indicates when the chamber's turbopump is activated. Figure 35 is generated using TVAC chamber pressure data from the first vacuum test. Although Figure 35 indicates the DVS240C is held at vacuum pressures longer than other tests, the functional test data capture occurs at the nominal test profile pressures for all tests. Functional testing is indicated with red stars in Figure 35 and is done before pump down, at LEO pressures, and

after pump down. The area between the dotted lines shows the time span during which the DVS240C is at approximate LEO vacuum pressures.

Figure 36 displays the nominal temperature test profile of the DVS240C for each of the executed tests. The graphed data is collected from the thermocouple located on the back of the DVS240C chip. Functional tests are again indicated with a red star and the area between the dotted lines shows the time period in which the DVS240C is at approximate LEO vacuum pressures. The temperature of the DVS240C spikes each time the system is turned on for a functional test data capture and immediately drops when the DVS240C is turned off. Figure 36 shows the approximate temperatures for each of the functional test data collections and indicates that they are within +/- 3 degrees Celsius of each other for each of the functional tests.

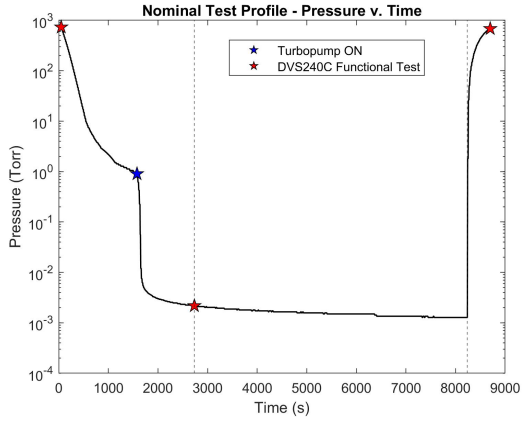

Figure 35. Nominal Test Profile Data for Vacuum Pressure

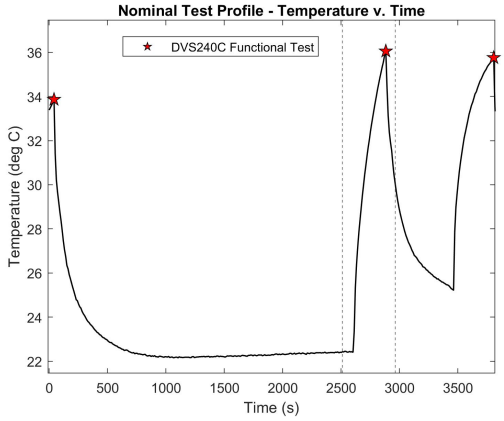

Figure 36. Nominal Test Profile Data for Temperature

Figures 37, 38, and 39 display the spatial data generated for the pre-, post-, and in-vacuum functional tests. Each figure plots the DVS240C event data as a heatmap by counting the number of ON and OFF events detected by each pixel over the duration of testing. The heatmap bins are created based upon the location of the DVS240C pixel on the focal plane array and the colormap uses a darker blue color to represent higher event counts and a lighter blue color to represent lower event

counts. While bins do not map perfectly to the sensor FPA, they provide a close representation of DVS spatial data. All figures plot approximately seven seconds of data with Figure 37 showing 7.058 seconds of data, Figure 38 showing 7.345 seconds of data, and Figure 39 showing 7.031 seconds of data. In all figures, the hole pattern on the aluminum box is visible in the data. The sensor generates the most events around the center circle of the hole pattern cluster since light has the most direct path to the DVS240C. All pre-, post-, and in-vacuum plots are similar based upon visual inspection, giving an early indication that the DVS240C sensor is able to survive the vacuum of space and maintain similar performance capabilities in atmospheric and space pressure conditions.

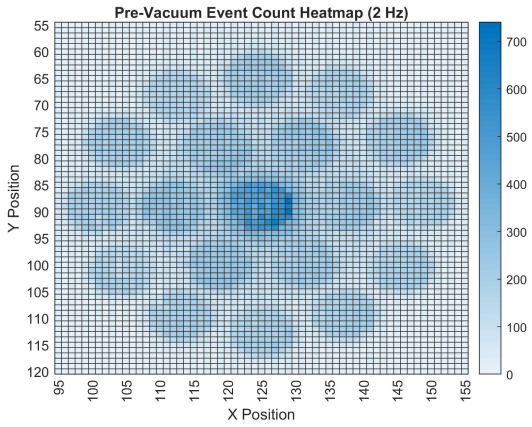

Figure 37. Pre-Vacuum Heatmap Generated for 2 Hz LED Blink Rate

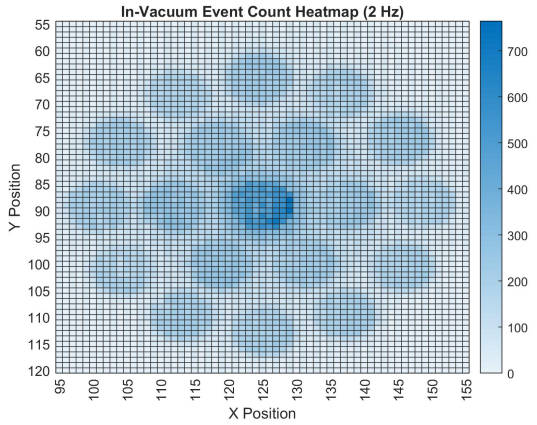

Figure 38. In-Vacuum Heatmap Generated for 2 Hz LED Blink Rate

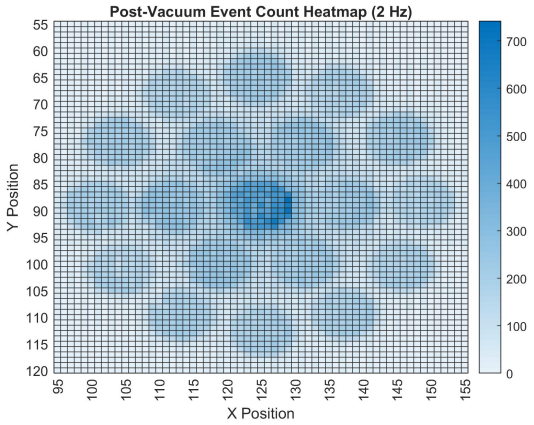

Figure 39. Post-Vacuum Heatmap Generated for 2 Hz LED Blink Rate

A more precise comparison of DVS240C performance in pre, post, and in-vacuum tests is made using the asynchronous Fourier analysis method. The Fourier analysis method uses the pixel area of interest displayed in Figures 40 and Figure 41. The pixel area is a rectangle of 99 pixels in [X,Y] positions [85:93, 120:130] on the sensor FPA. The same pixel area of interest is selected for pre-, post-, and in-vacuum data and exactly 7 seconds of each test set of data is used for the comparison.

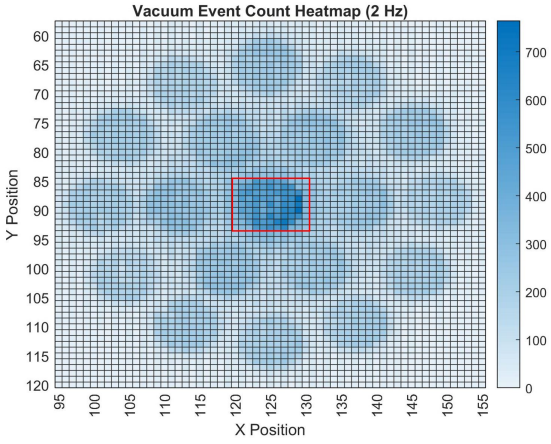

Figure 40. Vacuum Testing FPA for Fourier Analysis

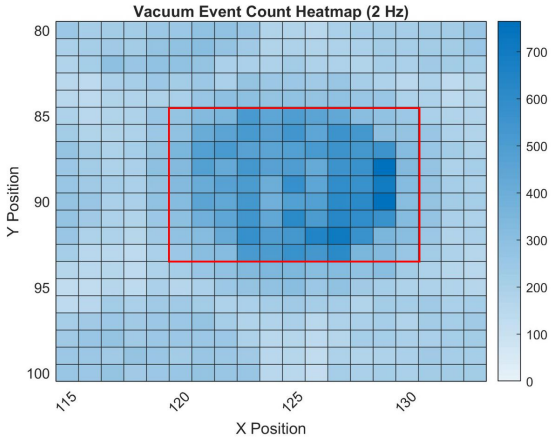

Figure 41. Vacuum Testing FPA for Fourier Analysis

Figures 42, 43, and 44 show the data as time domain signals. Each of the time domain signals display the 2 Hz blink frequency of the LED, with the pixels generating approximately two 'ON' events and two 'OFF' events every second. Additionally, the time domain signals display more 'ON' events (positive event counts) than 'OFF' events. DVS pixels generate a different number of 'ON' and 'OFF' events depending on the lighting environment, and therefore a difference in magnitude between 'ON' and 'OFF' event counts is normal.

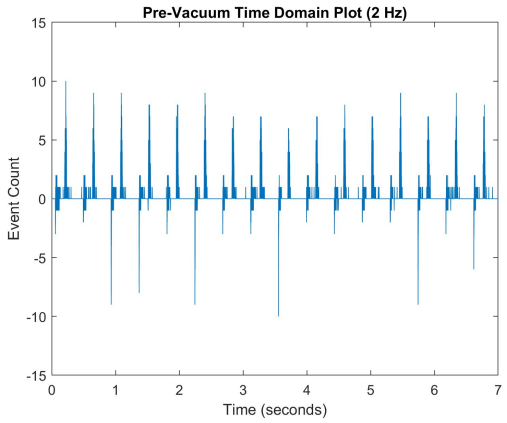

Figure 42. Pre-Vacuum Time Domain Plot Generated for 2 Hz LED Blink Rate

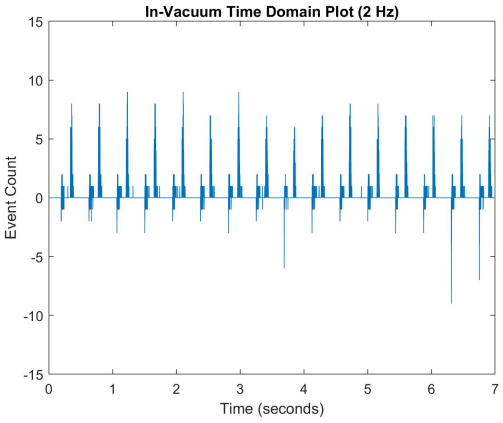

Figure 43. In-Vacuum Time Domain Plot Generated for 2 Hz LED Blink Rate

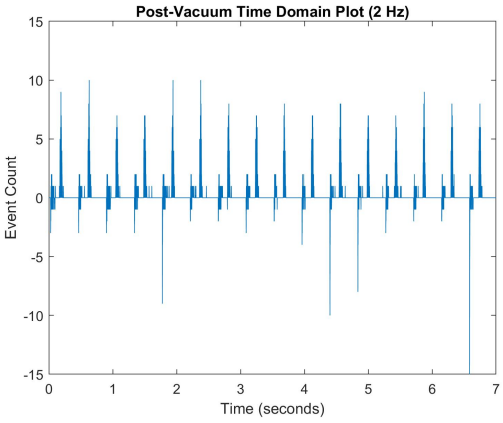

Figure 44. Post-Vacuum Time Domain Plot Generated for 2 Hz LED Blink Rate

Figures 45, 46, and 47 show the pre-, post-, and in-vacuum signal data in the frequency domain. The three plots display that the signals have the same fundamental and harmonic frequencies. The first significant peak marks the fundamental frequency (f) at a value of 2.286 Hz. There is a 0.37% difference in fundamental frequency magnitude between pre and post data and a 1.72% difference in fundamental frequency magnitude between pre and in-vacuum data. In all plots there are four harmonic frequencies with magnitudes greater than 10^4 at 2.286 Hz (f), 6.857 Hz (3f), 9.143 Hz (4f), and 13.71 Hz (6f), with the third harmonic frequency having the greatest magnitude. Each one is labeled and displayed in red. The third harmonic magnitude differs by 1.00% in the pre and post vacuum plots and by 1.48% in the pre and in-vacuum plots. Additionally, the noise floor appears to be at a magnitude of approximately 10^3 in all the data. The frequency domain results shown in Figures 45, 46, and 47 spike at the fundamental and harmonic frequencies, similar to Boettinger's results [7]. A 'cleaner' signal with less harmonics could be obtained by blinking the LED at a faster rate; however, for this testing it is more advantageous to blink at a slower rate in order to monitor the DVS240C event output visually. Boettinger did not identify an expected variation or classify sensor stationary noise using this data analysis method, therefore there is no established expected variation between the signals. However, the differences in signal are likely due to temperature variations and sensor stationary noise. In order to gain a true understanding of expected variation between signals, additional testing is needed. Overall, the similarity between the three frequency domain plots indicates that the DVS240C can survive and operate in the low Earth orbit vacuum environment with negligible degradation to performance.

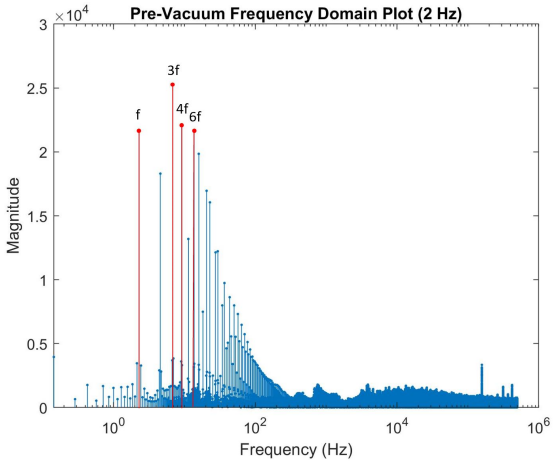

Figure 45. Pre-Vacuum Frequency Domain Plot Generated for 2 Hz LED Blink Rate

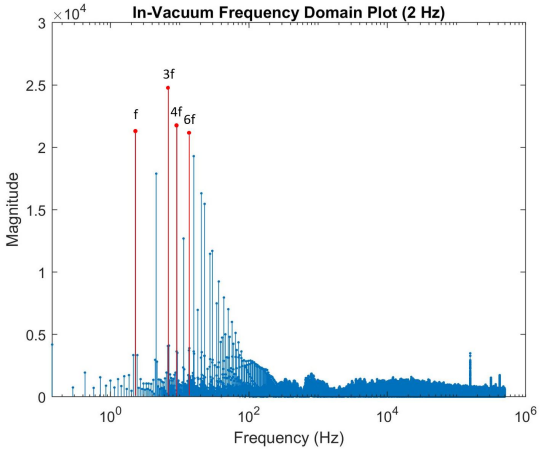

Figure 46. In-Vacuum Frequency Domain Plot Generated for 2 Hz LED Blink Rate

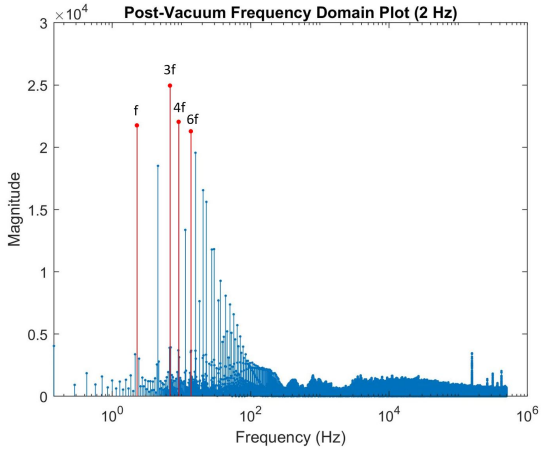

Figure 47. Post-Vacuum Frequency Domain Plot Generated for 2 Hz LED Blink Rate

Table 5 displays percent differences between the DVS240C signals for the first seven harmonic frequencies. Again, it can be seen that all harmonics occur at the same frequency in pre-, post-, and in-vacuum data with frequency differences calculated to the 15^{th} significant figure. The magnitude difference between pre-vacuum data and post/in-vacuum data are less than 4%, indicating the DVS240C can survive and operate in low Earth orbit vacuum environment without degraded performance.

Table 5. Percent differences as compared to DVS240C pre-vacuum functional test data.

	Post Vacuum		In Vacuum	
Harmonic	Frequency	Magnitude	Frequency	Magnitude
1st	0.00	0.37	0.00	1.72
2nd	0.00	1.09	0.00	2.15
3rd	0.00	1.00	0.00	1.48
4th	0.00	0.36	0.00	1.92
5th	0.00	1.35	0.00	3.94
6th	0.00	1.58	0.00	2.48
7th	0.00	1.47	0.00	2.86

4.2.2 Thermal Vacuum Test

The results of thermal vacuum testing indicate that the DVS240C is able to withstand low pressures of 10^{-4} Torr while experiencing temperatures between roughly -24 to 61°C. Thermal vacuum results also show that the DVS240C operates between -24 to 61°C and is capable of both a 'cold start' and 'hot start.'

Figure 48 displays the pressure profile for the duration of the test. The pressure is lower than 10^{-4} Torr (SMC required electronics qualification pressure) before the thermal cycle test begins and the start of the thermal cycle testing is indicated with a black star. The pressure increase and fluctuations immediately following the start of the thermal cycle test suggest outgassing from the system. Thermal cycle testing continues during outgassing and eventually the pressure drops below 10^{-4} Torr.

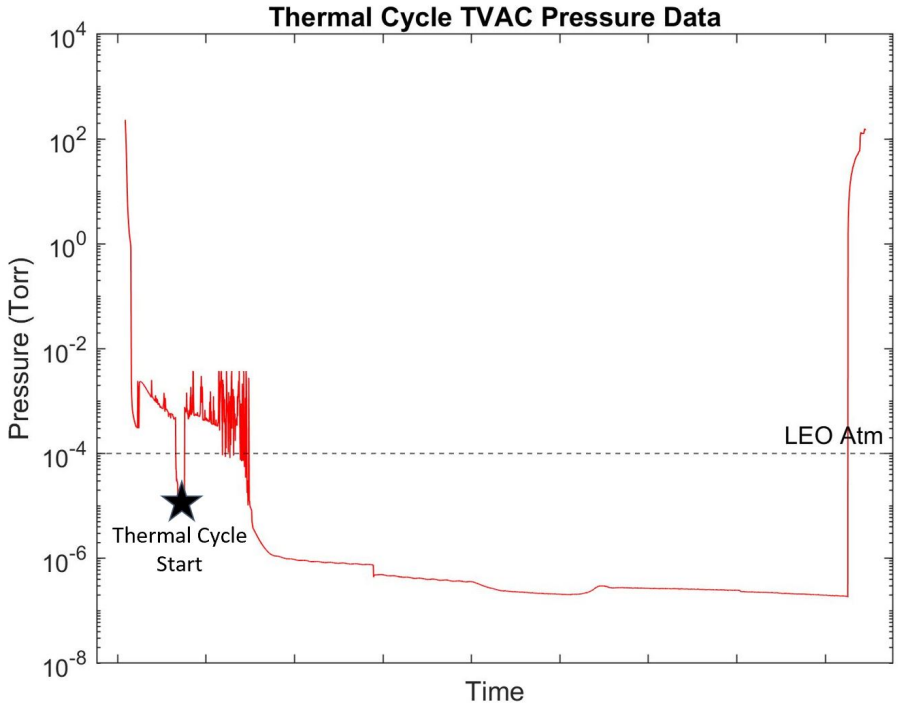

Figure 48. Thermal Cycle TVAC Pressure Data

Figure 49 displays the thermocouple data from testing. The thermal cycle testing is broken into two test runs - a hot cycle test and a cold cycle test. Both tests take approximately 8 hours to run and the numbers on Figure 49 indicate the locations of the DVS240C functional tests used in data analysis in this section. The five functional tests occur before thermal cycle (1), after the DVS240C 'hot start' (2), between the hot cycle and cold cycle (3), after the DVS240C 'cold start' (4), and after completion of the entire thermal cycle (5).

The thermocouples located on the DVS case side and plate serve as the controls for determining the temperature of the chamber and DVS240C environment. For the hot cycle, the DVS case side temperature is within +/- 9°C of the plate temperature throughout and for the cold cycle, the DVS case side temperature is within +/- 11°C of the plate temperature throughout. The highest and lowest temperatures experienced by the plate are 60.56°C and -23.58 °C respectively, while the highest

and lowest temperatures experienced by the DVS case side are 61.78°C and -18.73°C respectively. The 'hot start' test (functional test 2) occurs 30 minutes after the plate and DVS case side reach a temperature of 60°C. The 'cold start test' (functional test 4) occurs 30 minutes after the plate reaches -23°C. Functional test 3 is added as a precautionary measure between the hot and cold cycles to help explain any DVS240C performance issues should they arise (separation between hot and cold cycles). The thermocouples located on the DVS processing chip and black box are used for monitoring purposes and the temperature spikes seen throughout the plot show the DVS240C and blink circuit being powered on, therefore producing heat and increasing the temperature.

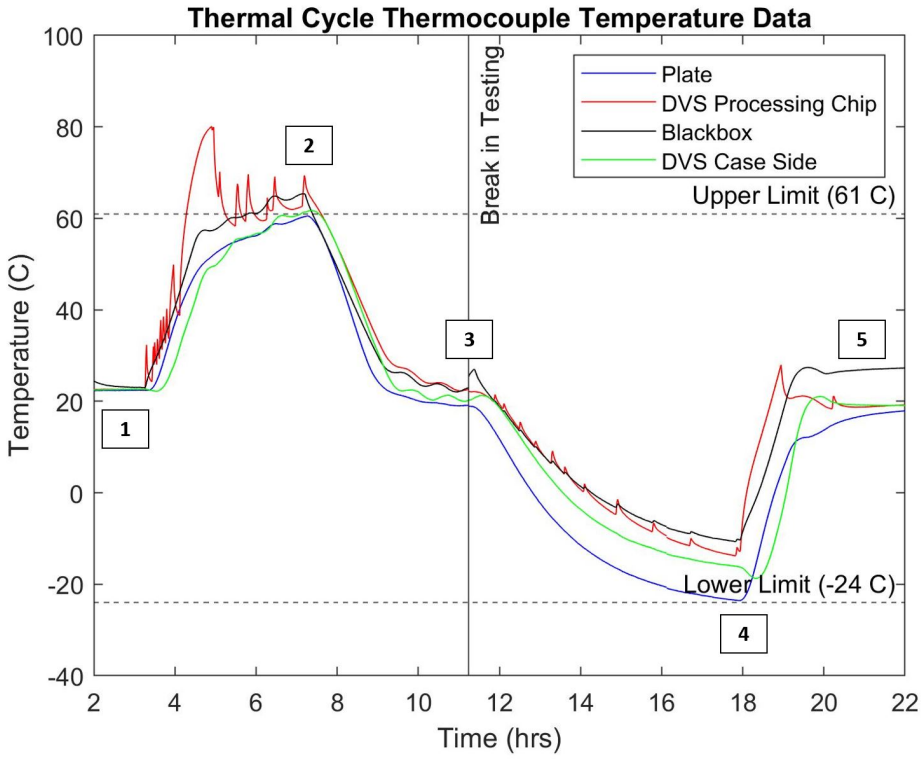

Figure 49. Thermal Cycle Thermocouple Temperature Data

DVS240C functional tests are executed throughout the temperature ramp up of the hot cycle and the temperature ramp down of the cold cycle. Table 6 shows the

hot cycle functional tests taken with every 10°C approximate increase in temperature. The table indicates that the DVS240C passed all functional tests from 20 to 61°C, including the 'hot start' functional test. Only one power cycle of the DVS240C at approximately 30°C was needed due to the DVS240C only registering 'ON' events (increasing light intensity). Executing a power cycle of the system fixed this issue and the DVS240C started registering both 'ON' and 'OFF' events again. Since the DVS240C passed all other functional tests during the temperature ramp up, the issue is considered a software issue rather than a camera functional error due to temperature changes.

Table 6. DVS240C Functional Test Results for Hot Cycle Ramp

Plate Temp (°C)	**Camera Side Temp (°C)**	**Functional Test**
22.29	22.38	Pass
34.27	26.21	Pass *Add'l Power Cycle
40.57	32.19	Pass
51.96	49.48	Pass
58.77	59.40	Pass
60.43	61.37	Hot Start Pass

Table 7 shows the cold cycle functional tests taken with every 10°C approximate decrease in temperature. The table indicates that the DVS240C passed all functional tests from -24 to 20°C, including the 'cold start' functional test.

Table 7. DVS240C Functional Test Results for Cold Cycle Ramp

Plate Temp (°C)	Camera Side Temp (°C)	Functional Test
18.20	20.01	Pass
10.74	17.71	Pass
-0.50	7.68	Pass
-8.20	-0.23	Pass
-19.74	-12.17	Pass
-23.53	-16.08	Cold Start Pass

Tables 6 and 7 indicate that the DVS240C is operational in the temperature ranges of approximately -24 to 61°C.

Fourier analysis is used to analyze the functional test data at the locations shown in Figure 49. The pixel area of interest used in the analysis is displayed in Figures 50 and 51. The pixel area is a rectangle of 117 pixels in [X,Y] positions of [84:96, 131:139] on the sensor FPA. The same pixel area of interest is selected for all five functional test data sets and exactly 7 seconds of each data set is used for the comparison.

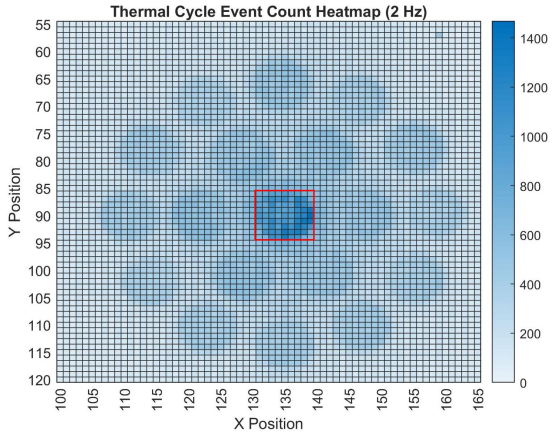

Figure 50. In-Vacuum Heatmap Generated for 2 Hz LED Blink Rate

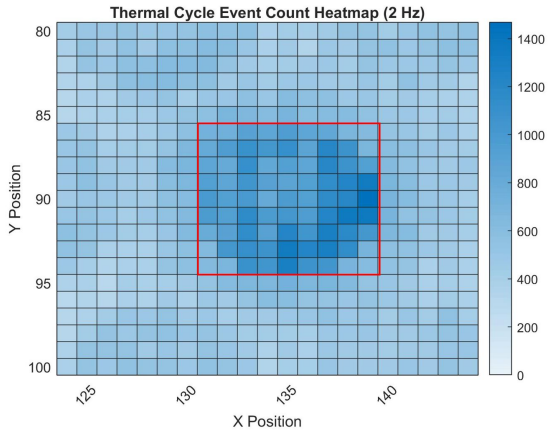

Figure 51. FPA Area used in Fourier Analysis for Thermal Cycle Testing

Figures 52 and 53 show the DVS240C signal before and after thermal cycle testing. The two signals have the same general shape with small differences (<4%) between each signal's harmonic frequency location for the first seven harmonics. There is a 30.62% difference between magnitudes at the third harmonic frequency. Therefore, although the third harmonic is the highest peak in pre thermal cycle data, it is not the highest peak in the post data. There is also a 174% difference between magnitudes at the seventh harmonic frequency, but the noise floor appears to be at a magnitude of approximately 10^3 in both test sets. Although there are differences in magnitude between some harmonic frequencies, there are not large differences at every frequency. These differences may be due to the slight temperature variations at the time of the data collection.

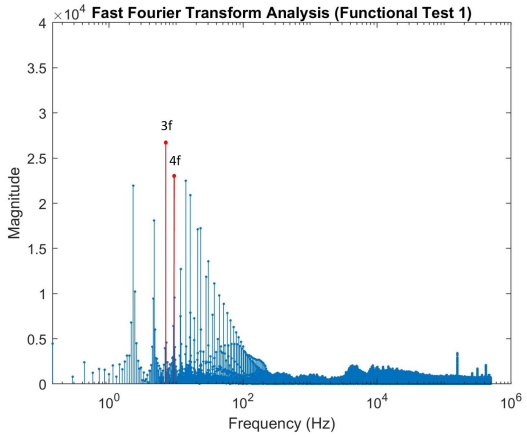

Figure 52. Functional Test 1 - Pre Thermal Cycle Frequency Domain Results

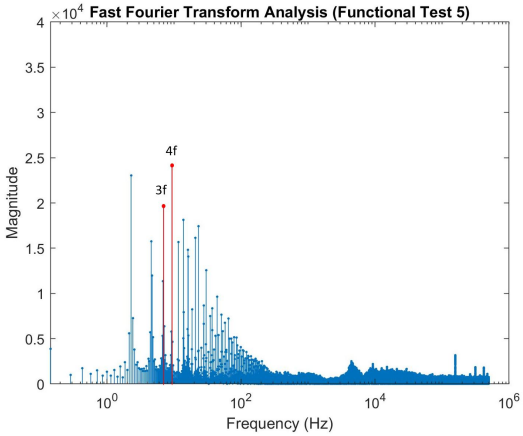

Figure 53. Functional Test 5 - Post Thermal Cycle Frequency Domain Results

Table 8 displays percent differences between pre and post thermal vacuum DVS240C signals for the first seven harmonic frequencies. The difference between the harmonic frequency values is less than 4%, but there is a larger difference between the harmonic magnitudes with the greatest difference at the 7th. However, since the other harmonic magnitudes are closer in magnitude, the DVS240C is considered to have

survived thermal cycle testing in vacuum for temperatures of -24 to 61°C with negligible degradation to operation. Further analysis and additional thermal cycle testing is needed to determine if thermal cycles in vacuum impact system performance.

Table 8. Percent differences between DVS240C post thermal vacuum (functional test 5) data and pre thermal vacuum (functional test 1) data.

	Post Thermal Vacuum	
Harmonic	Frequency	Magnitude
1st	0.00	4.87
2nd	3.08	13.92
3rd	0.00	30.62
4th	0.00	4.82
5th	1.23	20.87
6th	1.03	21.43
7th	0.88	174.43

Fourier analysis is also used to consider operation of the DVS240C during hot and cold starts. The hot start data is displayed in Figure 54 and cold start data is displayed in Figure 55.

The hot start signal data has harmonic frequencies of significantly decreased magnitude, although the harmonic frequencies are still large enough to be distinguished. There is a 61% difference between the fundamental frequency magnitude of the hot start data and pre thermal cycle data. These larger magnitude differences are found throughout the harmonic frequencies of the hot start signal with 76.90%, 95.56%, and 107.40% differences found between the second, third, and sixth harmonic magnitudes as compared to pre thermal cycle data. The harmonic frequency magnitude differences are a result of the increased temperature, causing more noise in the DVS240C data, making the blinking LED harder to distinguish.

The cold start data has harmonic frequencies of increased magnitude as compared to the pre thermal cycle data. The peak frequency in the cold data occurs at the third harmonic just like in the pre thermal cycle data, however its magnitude is

21.33% higher. The cold start has a narrower range of harmonic frequencies with large magnitudes, indicating less noise and a clearer LED blink signal.

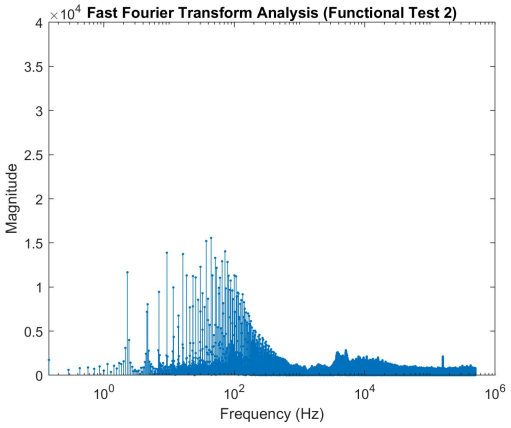

Figure 54. Functional Test 2 - Hot Start Frequency Domain Results

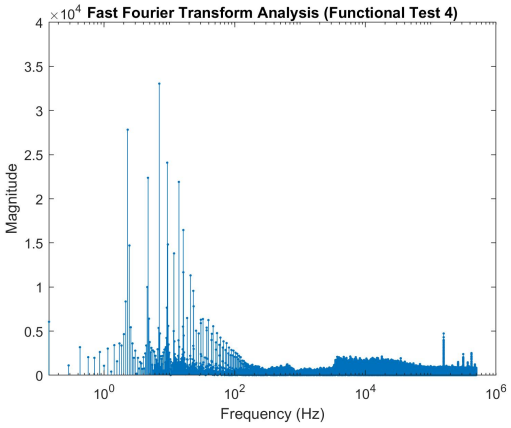

Figure 55. Functional Test 4 - Cold Start Frequency Domain Results

Table 9 displays the signal differences between the pre thermal vacuum data and the hot/cold start data for the first seven harmonic frequencies.

Table 9. Percent differences of DVS240C frequency signal as compared to pre thermal vacuum functional test data.

	Hot Start (Functional Test 2)		Cold Start (Functional Test 4)	
Harmonic	Frequency	Magnitude	Frequency	Magnitude
1st	0.00	61.21	0.00	23.61
2nd	0.00	76.90	0.00	21.09
3rd	0.00	95.56	0.00	21.33
4th	0.00	48.97	0.00	5.05
5th	1.23	24.31	0.00	8.15
6th	0.00	107.40	0.00	2.68
7th	0.00	41.40	0.00	23.77

4.2.3 Vibration Tests

The results of vibration testing demonstrate that the DVS240C is able to withstand random vibration in every axis over the frequency range of 20-2000 Hz with an overall acceleration level of 6.958 G_{RMS} for one minute.

Figures 56, 57, and 58 display the random vibration plots for the DVS240C X, Y, and Z axes respectively. Each figure includes power spectral density (PSD) information from each of the accelerometers over the one minute testing duration. Accelerometer 1 (Control - shaker table) is indicated with black, accelerometer 2 (Top - Z Axis) with blue, accelerometer 3 (Front - Y Axis) with red, and accelerometer 4 (Side - X Axis) with green. In each test, the control (shaker table) remains within +/- 0.005 g^2/Hz of the desired vibration profile (shown in yellow).

The accelerometer located on the axis of vibration determines the fundamental frequency for the DVS240C vibration in that direction (e.g. accelerometer 4 for the X axis). The fundamental frequency is the lowest resonant frequency produced by vibrating the object and can also be called the natural or resonant frequency. In Figure 56, accelerometer 4 shows the fundamental frequency for X axis vibration at approximately 1790 Hz. Figure 57 displays accelerometer 3 with a fundamental frequency peak around 1630 Hz for Y axis vibration. Finally, the fundamental frequency for Z axis vibration is shown at approximately 1680 Hz. One additional note is that both random vibration and sine sweep data display similar shapes and fundamental frequencies for the X and Y axes.

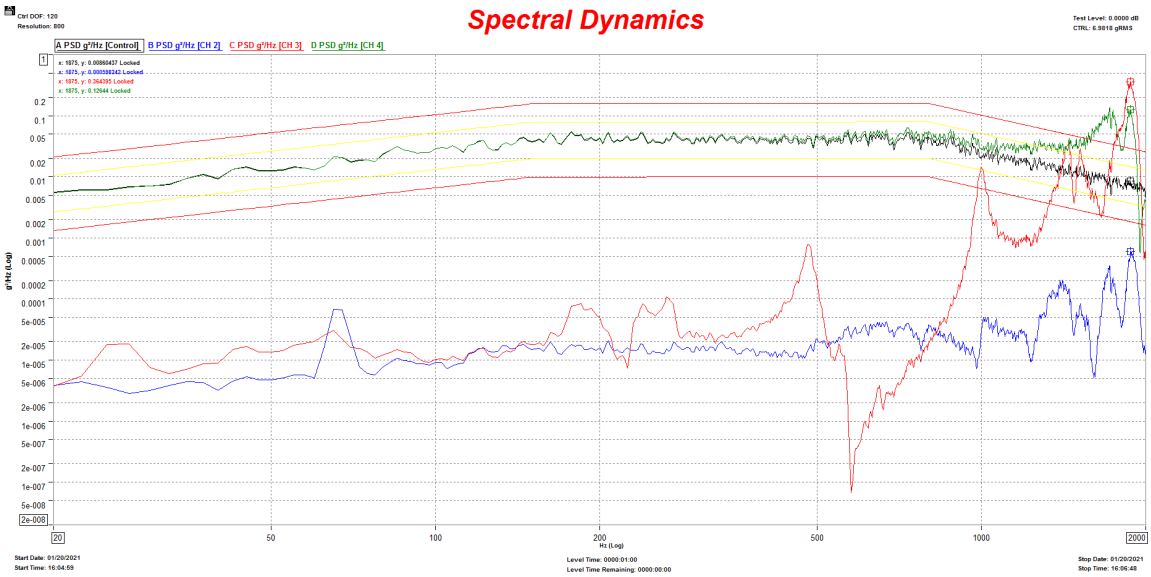

Figure 56. X Axis Random Vibration Test Profile

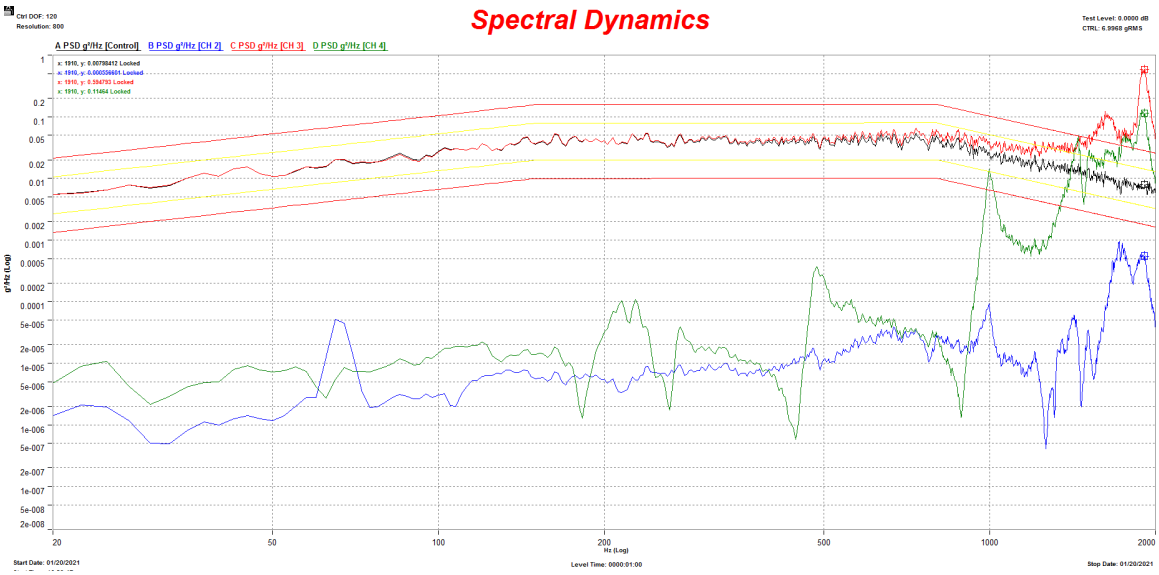

Figure 57. Y Axis Random Vibration Test Profile

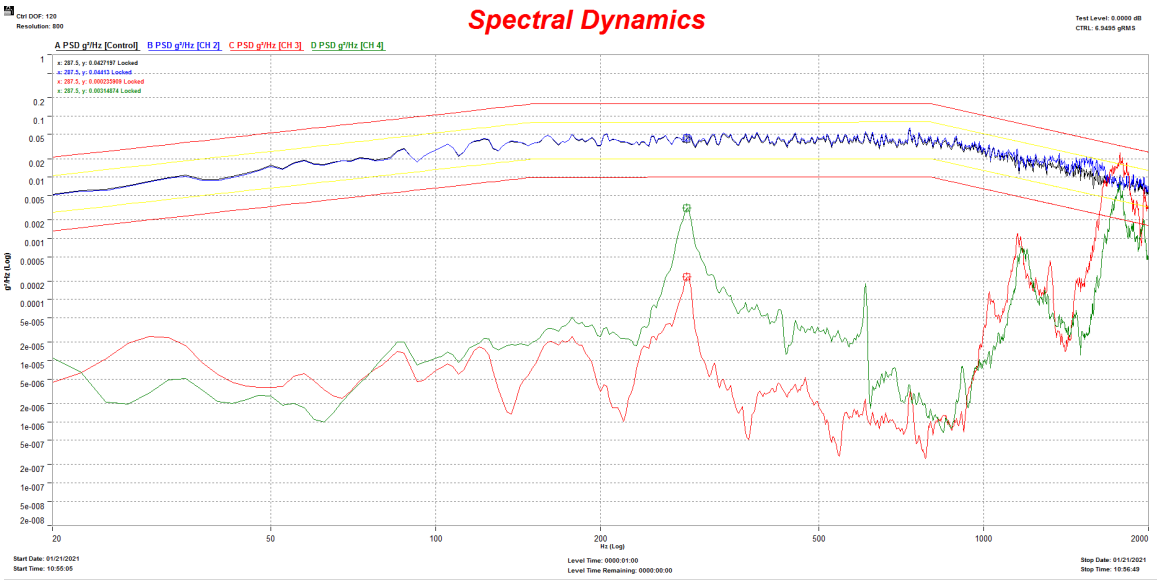

Figure 58. Z Axis Random Vibration Test Profile

Table 10 gives the fundamental frequency for each of the vibration axes and average overall G_{RMS} values experienced by the shaker table.

Table 10. Random Vibration Test Data

Vibration Axis	Fundamental Frequency (Hz)	Control G_{RMS} (g^2/Hz)
X Axis	1790	6.982
Y Axis	1630	6.997
Z Axis	1680	6.950

Figures 59-64 display the sine sweep comparison data for each vibration test axis (X, Y, and Z). The pre-vibe sweep data establishes a baseline vibration signature and the post-vibe sweep data is compared with the baseline to assess if any significant damage occurred during random vibration testing. All graphs use a log-log scale with pre-vibe sweep data in blue and post-vibe sweep data in red. The acceleration remains approximately 0.5g until approaching the DVS240C axes' natural frequencies, identified by the black vertical lines in Figures 60, 62, and 64. Initial visual assessment

indicates no significant damage to the DVS240C during X, Y, or Z axis random vibration testing.

Figures 59 and 60 display acceleration versus frequency data for X axis vibration. The data is from accelerometer (4) located on the side of the DVS240C. Two distinct frequency peaks occur at 1792.55 Hz and 1877.14 Hz (natural frequencies). Pre and post sine sweep data show there is no shift between natural frequencies for either peak, but indicate a 6.58% difference in magnitude for the first peak and a 14.13% difference in magnitude for the second peak. Although peak 2 exceeds the allowable magnitude difference to consider pre and post data 'the same,' nothing appeared loose or broken with the DVS240C setup. Therefore, the DVS240C is considered to have passed the X axis sine sweep vibration comparison and functional test data is used to further determine any degradation to the system.

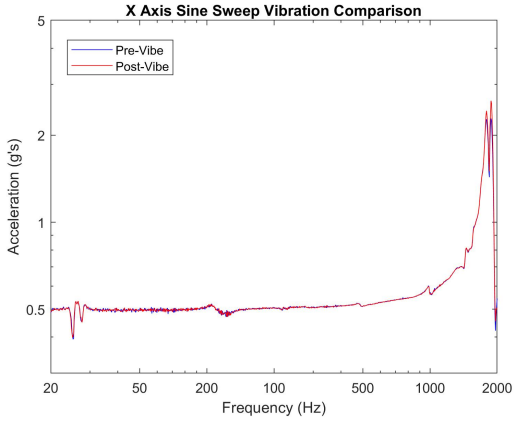

Figure 59. X Axis Sine Sweep Vibration Comparison

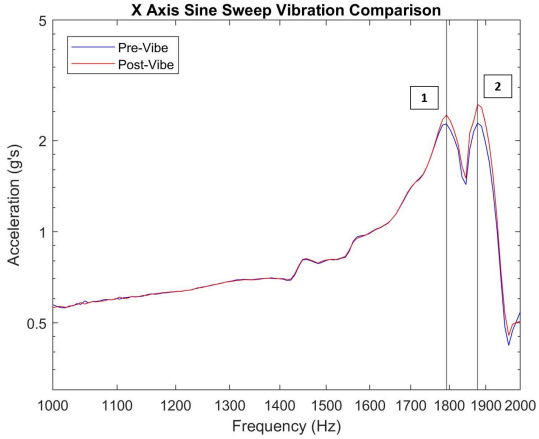

Figure 60. X Axis Sine Sweep Vibration Comparison

Figures 61 and 62 display acceleration versus frequency data for Y axis vibration. The data is from accelerometer (3) located on the front of the DVS240C. One distinct frequency peak can be seen in each of the data sets at 1920.91 Hz (pre-vibe) and 1909.88 Hz (post-vibe). There is a 0.58% shift in frequencies between the two tests and a 8.64% difference in acceleration magnitudes. Therefore, the DVS240C is considered

to have passed the Y axis sine sweep vibration comparison. DVS240C functional test data is used to further determine any degradation to the system.

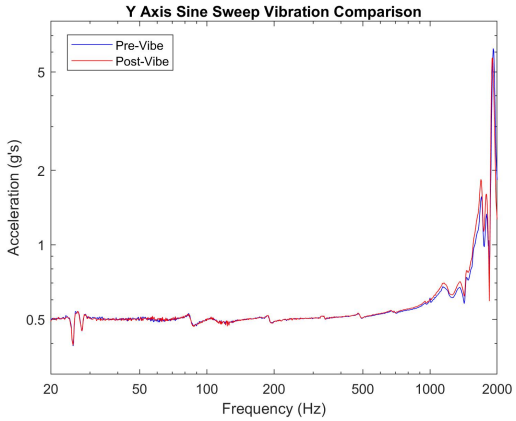

Figure 61. Y Axis Sine Sweep Vibration Comparison

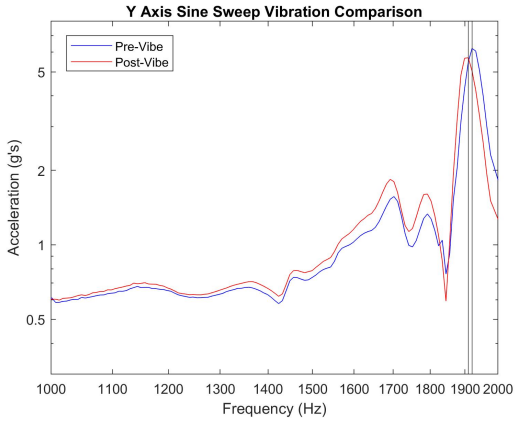

Figure 62. Y Axis Sine Sweep Vibration Comparison

Figures 63 and 64 display acceleration versus frequency data for Z axis vibration. The data is from accelerometer (2) located on the top of the DVS240C. One distinct frequency peak can be seen in each of the data sets at 1682.43 Hz (pre-vibe) and 1672.76 Hz (post vibe). There is a 0.58% shift in frequencies between the two tests and a 0.24% difference in acceleration magnitudes. Therefore, the DVS240C is considered to have passed the Z axis sine sweep vibration comparison. DVS240C functional test data is used to further determine any degradation to the system.

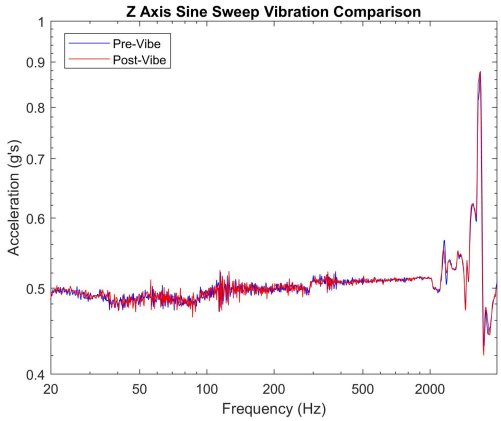

Figure 63. Z Axis Sine Sweep Vibration Comparison

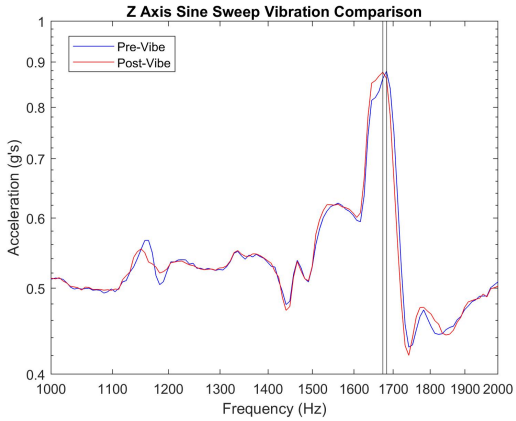

Figure 64. Z Axis Sine Sweep Vibration Comparison

Table 11 summarizes the differences in the sine sweep data for each axis.

	Frequency Difference (%)	**Magnitude Difference (%)**
X Axis (1)	0.00 %	6.58 %
X Axis (2)	0.00 %	14.13 %
Y Axis	0.58 %	8.64 %
Z Axis	0.58 %	0.24 %

Table 11. DVS240C Sinusoidal Sweep Vibration Comparison

Fourier analysis is used to analyze the DVS240C functional test data at the sample center pixel shown in Figures 65 and 66 when the LED is blinking at 2 Hz. The pixel area of interest is an 81 pixel rectangle on the sensor FPA. Each data set analyzes 7 seconds of data over the same 81 pixel area of interest.

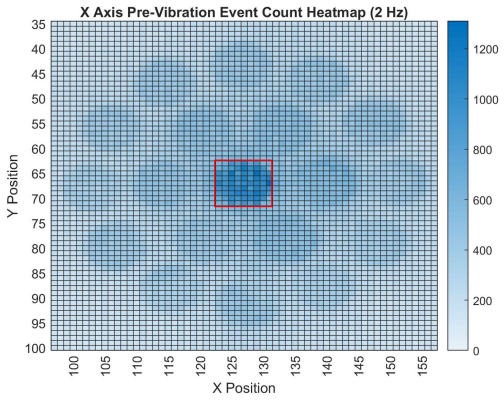

Figure 65. Vibration DVS240C Functional Test Heatmap Generated for 2 Hz LED Blink Rate

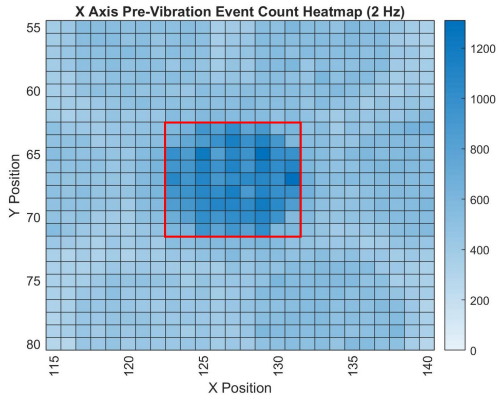

Figure 66. FPA Area used in Analysis for Vibration Testing

Figures 67-70 display the DVS240C functional data taken before and after each axis of random vibration testing. Although six DVS240C functional tests were executed, only data from four of the tests is represented in this analysis. This is because there are negligible differences between data captured for the post X and pre Y and data captured for the post Y and pre Z. The only events that occurred between these data captures is a DVS240C power cycle. Therefore, a post functional test can also serve as a pre functional test before the next random vibration test begins.

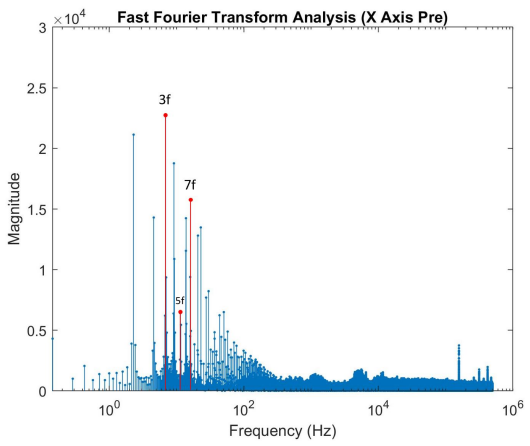

Figure 67. X Axis Pre Random Vibration Frequency Domain Results

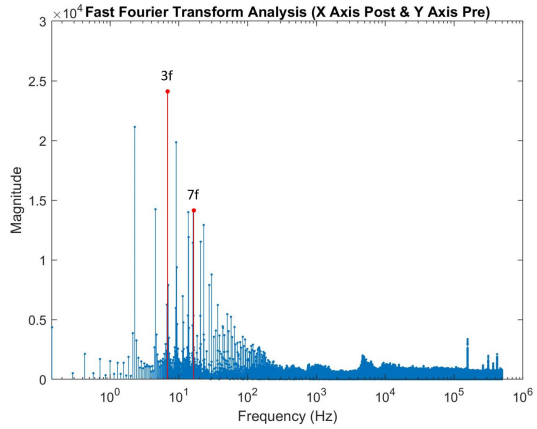

Figure 68. X Axis Post & Y Axis Pre Random Vibration Frequency Domain Results

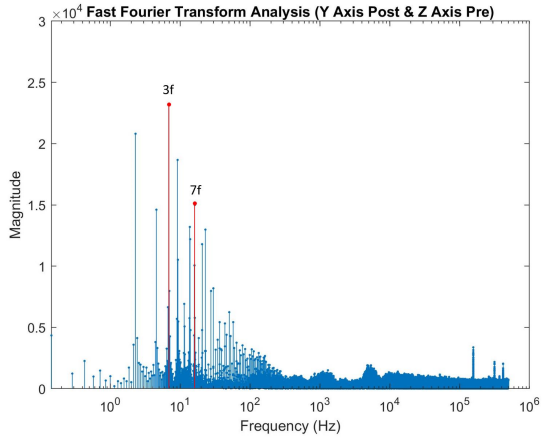

Figure 69. Y Axis Post & Z Axis Pre Random Vibration Frequency Domain Results

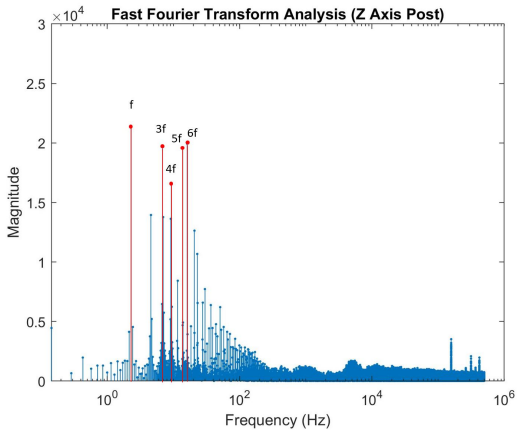

Figure 70. Z Axis Post Random Vibration Frequency Domain Results

The four plots display that the DVS240C signal has approximately the same fundamental and harmonic frequencies before and after random vibration testing. In all cases, the first seven harmonic frequencies are within 5% of each other. A comparison of pre and post X axis vibration functional data reveals a maximum frequency difference of 4.04% at the 3rd harmonic frequency and a maximum magnitude decrease of 11.25% at the seventh harmonic frequency. A comparison of pre and post Y axis vibration functional data reveals a maximum frequency difference of 4.04% at the third harmonic frequency and a maximum magnitude increase of 6.26% at the seventh harmonic frequency. Figure 70 is data from the last functional test executed (after random vibration testing of X, Y, and Z axes) and shows the largest signal deviation from pre-random vibration data. The post Z axis vibration functional data has similar fundamental and harmonic frequencies to pre vibration data, with a maximum difference in frequency of 1.55% found at the fourth harmonic. However, there is a 38.95% maximum increase in magnitudes from the pre to post Z axis vibration data at the sixth harmonic. Additionally, the event frequency magnitudes vary more across all harmonic frequencies which can be seen visually in Figure 70 and in Table 12. The fundamental frequency at 2.286 Hz has the largest peak rather than the third

harmonic frequency, which has the largest peak in all other plots. When comparing the post vibration data in Figure 70 to the pre vibration data in Figure 67, more similarity exists between the signals. The largest percent difference is a 27.35% increase in magnitude at the fifth harmonic. Since initial pre random vibration (before X, Y, and Z vibration) is closer to the final post vibration data (after X, Y, and Z vibration), it is unlikely that the differences in signal indicate a sensor performance issue. It is likely that the signal differences emerge due to variability in the sensor or testing environment setup. Additionally, the noise floor appears to be at a magnitude of approximately 10^3 in all the data, indicating the sensor is responding with similar performance before and after random vibration testing.

Table 12 displays the percent differences in pre and post DVS240C signal data for the X, Y, and Z axes. The data shows the first seven harmonic frequencies. Overall, the vibration results indicate that the DVS240C sensor is capable of surviving takeoff and ascent vibration with negligible operational degradation.

Table 12. Percent difference between DVS240C pre and post random vibration frequency signal for X, Y, and Z axes.

	X Axis		Y Axis		Z Axis	
Harmonic	Frequency	Magnitude	Frequency	Magnitude	Frequency	Magnitude
1st	0.01	0.03	0.00	1.57	0.00	2.80
2nd	0.01	0.58	0.00	2.57	0.00	4.55
3rd	4.04	6.06	4.04	3.64	0.00	16.21
4th	0.00	5.67	0.00	6.07	1.55	12.03
5th	0.01	8.17	0.00	0.58	1.22	19.86
6th	1.07	1.75	0.00	5.89	1.09	38.95
7th	0.02	11.25	0.00	6.26	0.00	28.29

4.3 Application Demonstration

4.3.1 Space Domain Awareness Tests

The results of the SDA demonstration reveal that the event-based sensor does not saturate when pointed directly at solar simulator and Sun. Initial investigation of the SDA application indicates that it is feasible to use the event-based sensor to detect bright and dark objects in the presence of the Sun. The testing results display that the sensor can detect bright objects within typical solar exclusion angles. Additionally, the results display that the sensor can detect dark objects near and passing in front of the Sun. All of the testing results use the DVS240C manufacturer sensitivity settings and therefore additional investigation is needed to fully understand the sensor's detection capabilities. Ultimately, the results show that event-based sensor does not require a solar exclusion angle as traditional CMOS and CCD sensors, therefore providing an opportunity to fill a space SDA capability gap.

4.3.1.1 Bright Object

The SDA application demonstration for bright object detection includes results from testing with the solar simulator and the Sun. The 2Hz blinking LED is used as the bright object ('target') and is meant to simulate a bright object in space, such as a star. Results show that the event-based sensor detects the bright object at angles of 0, 20, and 30 degrees with respect to the solar simulator. Results also display the sensor detects a blinking LED when pointed directly at the Sun.

DVS240C functional test data is displayed in this section. Heatmap data is plotted to serve as a tool for visualization of the event data and the frequency domain signal data is plotted to determine detection capability. The frequency domain signal for each plot is generated using 7 seconds of DVS data from the center hole of the black box pattern shown in figure 71. Figure 72 serve as a baseline for signal comparison.

The figure displays the frequency signal from the 2Hz blinking LED when the solar simulator is turned off. It indicates the fundamental frequency (f) is located at 2.286 Hz and has the greatest magnitude.

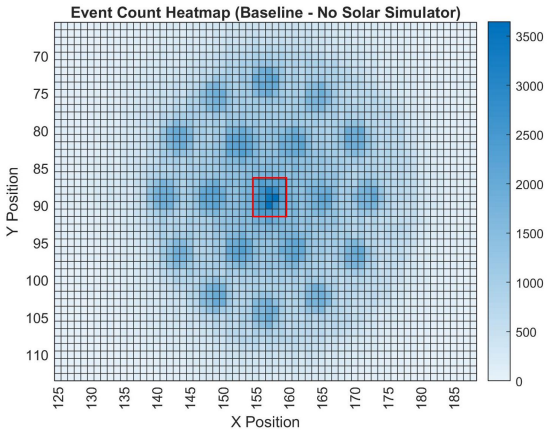

Figure 71. DVS240C Heatmap at Zero Degrees with Solar Simulator

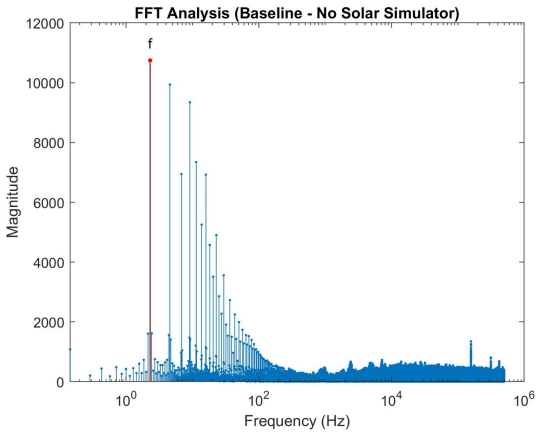

Figure 72. DVS240C Signal in the Frequency Domain with Solar Simulator OFF (Baseline)

Figure 73 and 74 display the DVS240C event output with the solar simulator directly behind the bright object target. The figures display that blinking LED is detected. Although the entire hole pattern on the black box is not visible as it is with the solar simulator off, the center hole is still visible. Translating this center pixel into the frequency domain reveals that the signal can be seen above the noise floor. The fundamental frequency (f) is still located at 2.286 Hz, however, the magnitude is 1719, a 144% decrease from the baseline signal.

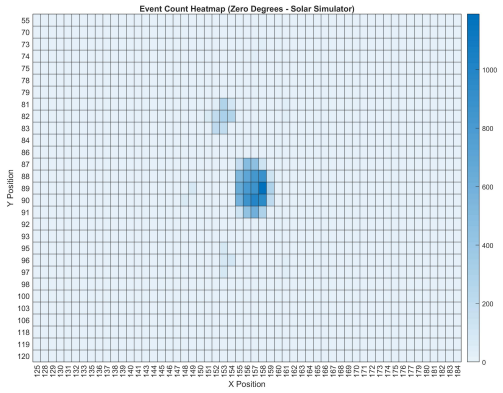

Figure 73. DVS240C Heatmap at Zero Degrees with Solar Simulator

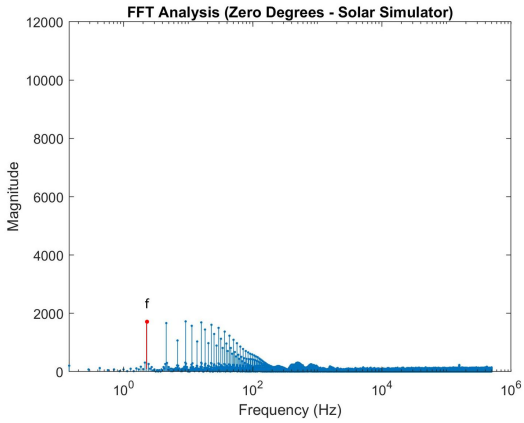

Figure 74. DVS240C Frequency Domain Signal at Zero Degrees with Solar Simulator

While the data indicates that the blinking LED can be detected when the solar simulator is behind the bright object target, additional investigation reveals that the black box setup blocked much of the solar simulator light from hitting the FPA. This can be seen with Figure 75 which shows the outline of the black box on the right side of the plot. Additional data collected using the APS functionality of the DVS240C displays that a conventional sensor does not saturate in this environment. Figure 76 displays a frame captured with the solar simulator directly behind the box. In this figure the hole pattern is visible. Therefore, the zero degree test results do not distinctly reveal an advantage of using the event-based sensor.

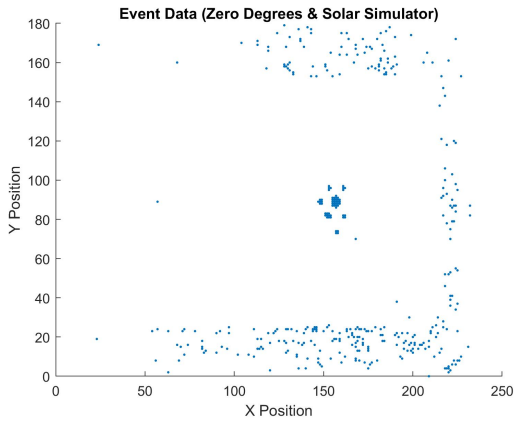

Figure 75. DVS Output - Zero Degrees with Solar Simulator

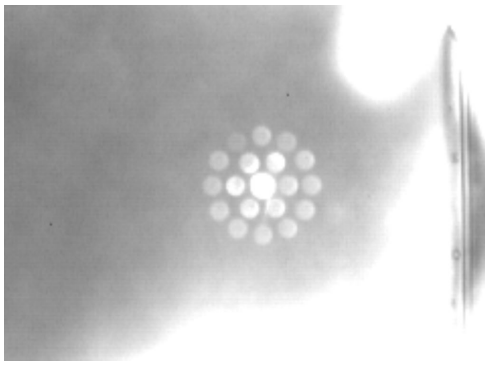

Figure 76. APS Sensor Output - Zero Degrees with Solar Simulator

Figure 77 and 78 display the results with the solar simulator at a 10 degree angle with respect to the sensor. Initial visualization from this test shows that the bright object is not detected. Figure 77 shows the solar simulator light bulb on the right side of the heatmap, but there is no obvious LED hole pattern. Figure 78 displays the signal in the frequency domain with low magnitude values close to the noise floor at all frequencies. The largest magnitude frequency in the plot appears at the fourth harmonic frequency (4f) of 9.143 Hz.

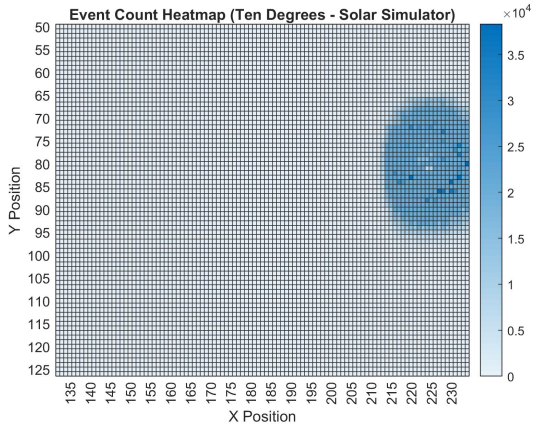

Figure 77. DVS240C Heatmap at Ten Degrees with Solar Simulator

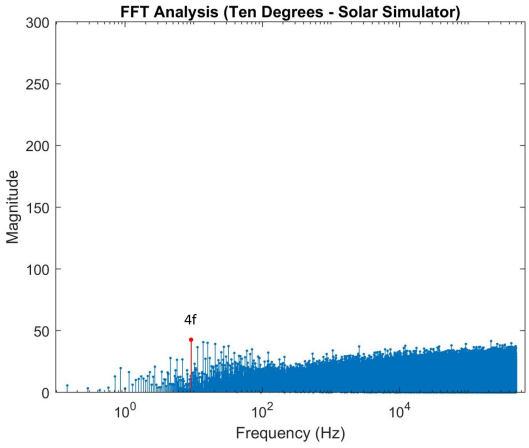

Figure 78. DVS240C Signal in the Frequency Domain at Ten Degrees with Solar Simulator

Although the 2 Hz LED signal cannot be seen in Figure 78, this test still reveals one advantage of using event-based sensors for bright object detection near the Sun. Figures 79 and 80 show output from the DV software which indicate that the sensor does not saturate. The images are constructed by accumulating DVS events to create a frame-like output (pseudoframe). The solar simulator light bulb can be seen in both images with the side of the black box also visible in Figure 80.

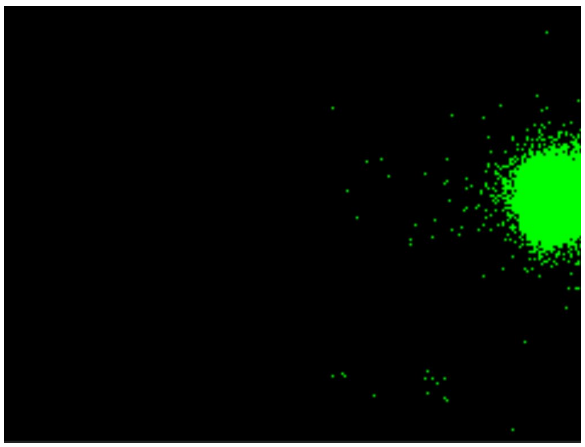

Figure 79. DVS240C Event Output - Ten Degrees and Solar Simulator

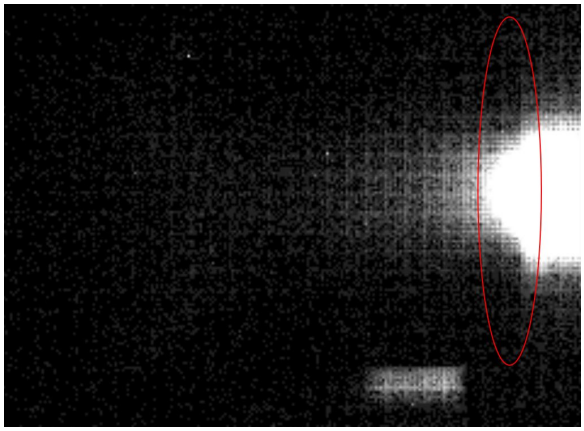

Figure 80. DVS240C Pseudoframes - Ten Degrees and Solar Simulator

Figures 81-84 display the results from testing with the solar simulator at a 20 degree and 30 degree angle with respect to the sensor. At these angles, the solar simulator light bulb is no longer within the view of the DVS240C and the bright object (blinking LED) is detectable. At a 20 degree angle, the sensor can barely detect the bright object. As shown in the heatmap in Figure 81, only a few pixels at the center hole of the pattern generate events. However, the fourth harmonic frequency (4f) at 9.167 Hz is above the noise floor as shown in Figure 82. At a 30 degree angle, the blinking LED signal is more distinguished and has a fundamental frequency (f) at 2.286 Hz again. The fundamental frequency magnitude is 161.37% below the baseline signal. As expected, the bright object signal is closer to the baseline at further angles with respect to the solar simulator. These results give an initial indication that the

event-based sensor is advantageous for SDA near the sun since 20 and 30 degree angles are typical values for solar exclusion angles of conventional CMOS and CCD sensors in space. However, additional testing needs to be done to establish more confidence and gain understanding of bright object detection near the Sun.

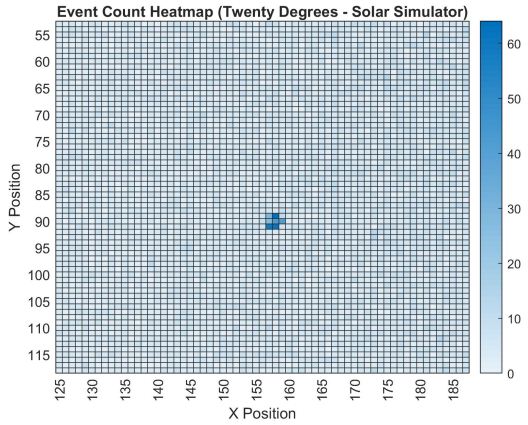

Figure 81. DVS240C Heatmap at Twenty Degrees with Solar Simulator

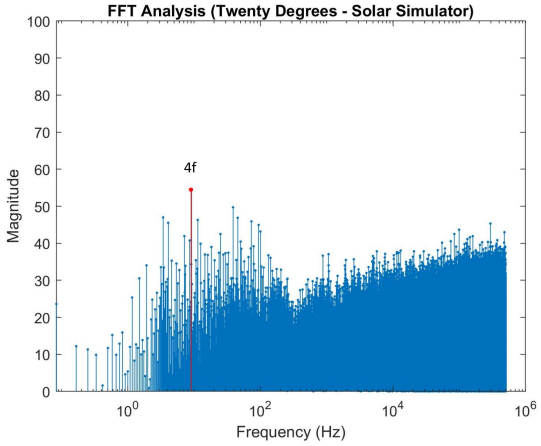

Figure 82. DVS240C Signal in the Frequency Domain at Twenty Degrees with Solar Simulator

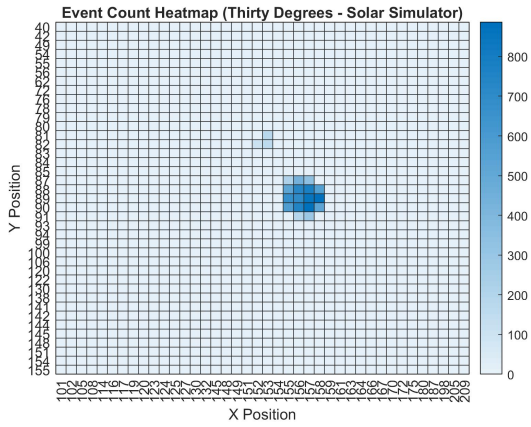

Figure 83. DVS240C Heatmap at Thirty Degrees with Solar Simulator

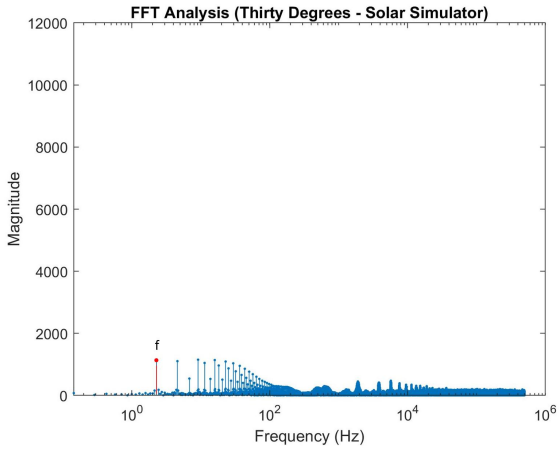

Figure 84. DVS240C Signal in the Frequency Domain at Thirty Degrees with Solar Simulator

Figure 85 shows the setup of a field experiment with the DVS240C outside pointing at the Sun. During this test, a blinking LED bulb was put within the sensors field of

view. Results from the test are shown in Figures 86 and 87. In both images, events are generated by the Sun and can be seen in the center of the screen. The blinking LED is faintly visible and its position is circled in red. The DVS240C APS was also used to look at absolute brightness values with the same experimental setup; however, the sensor saturated when pointed at the Sun.

Figure 85. DVS240C Outside Pointed at the Sun

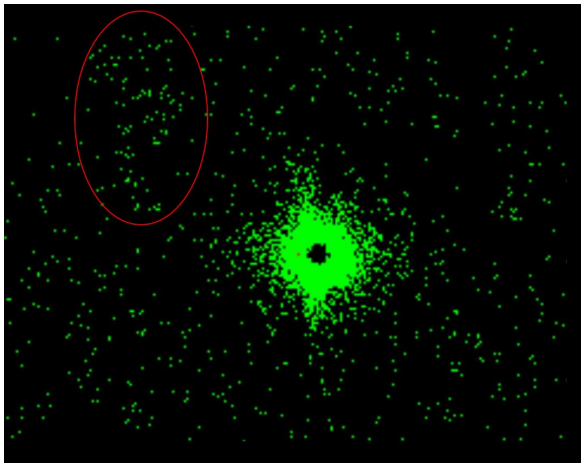

Figure 86. DVS240C Event Output - Outside Pointed at the Sun with blinking LED in FOV

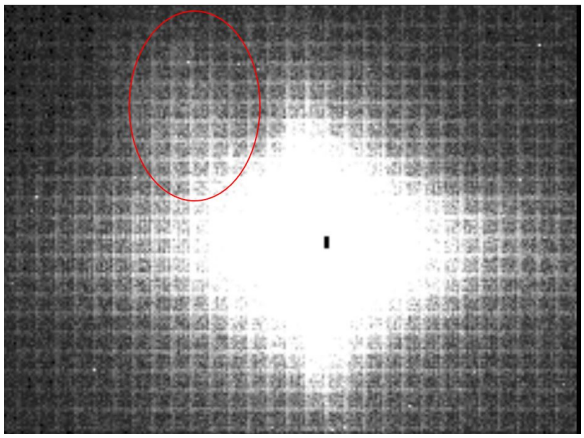

Figure 87. DVS240C Pseudoframes - Outside Pointed at the Sun with blinking LED in FOV

The test results show that there is a potential SDA advantage of using the event-based sensor in space. Although the LED is not detectable at all angles with the solar simulator and faintly detectable in the presence of the Sun, the DVS240C does not saturate when the solar simulator or Sun are within the field of view of the sensor. Additionally, bright objects can be detected with the DVS240C at angles falling within the typical solar exclusion zone. However, additional testing is needed to gain a full understanding of bright object detection near the Sun. Experimental setup should involve changing sensor sensitivity settings as well as experimenting with objects of varying brightness in relation to the Sun. Additionally, simultaneously capturing data with a traditional space-based sensor during experimentation would give better insight into the true advantage event-based sensors hold. Overall, the solar simulator and outside testing results indicate the feasibility and advantage of using event-based sensors to do bright object detection in space and should be further investigated.

4.3.1.2 Dark Object

The SDA application demonstration for dark object detection includes results from testing with the solar simulator and the Sun. A rotating black circle is used as the dark object ('target') and is meant to simulate a dark object in space, such as a piece of debris or satellite. Results show that the event-based sensor detects the dark object when the solar simulator is within the sensor's field of view (0 and 10 degrees). Results also show that the DVS240C is able to detect dark objects as they move across the Sun.

Results from solar simulator testing are displayed in Figures 88-93. Figures 88-90 display DVS240C event data with the solar simulator at a zero degree angle with respect to the sensor. Figures 89 and 90 show the light bulb of the solar simulator is detected by the event-based sensor and it can be seen that the edge of the rotating black circle crosses over part of that light bulb. Visualization of the data is shown with Figure 88 which displays approximately 10 seconds of DVS240C event data as a heatmap and Figure 31 which is one frame of accumulated events captured during the test. The frame output shows event data with green indicating 'ON' events (increasing intensity) and red indicating 'OFF' events (decreasing intensity). Figure 89 translates the first 5 seconds of data into the frequency domain. The highest frequency peak is located at 63.6 Hz and approximates the rotational speed of the fan. These results indicate that the sensor does not saturate and is able to detect a dark object near the Sun.

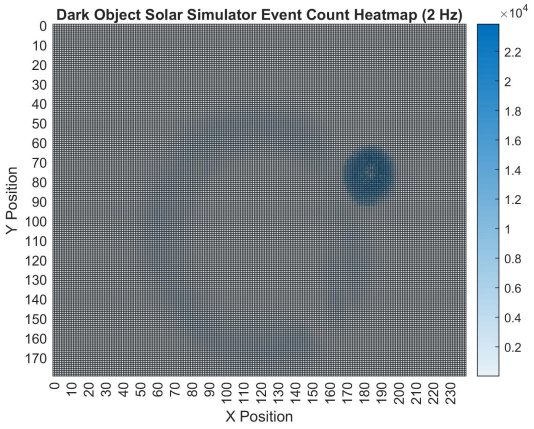

Figure 88. DVS240C Heatmap at Ten Degrees with Solar Simulator

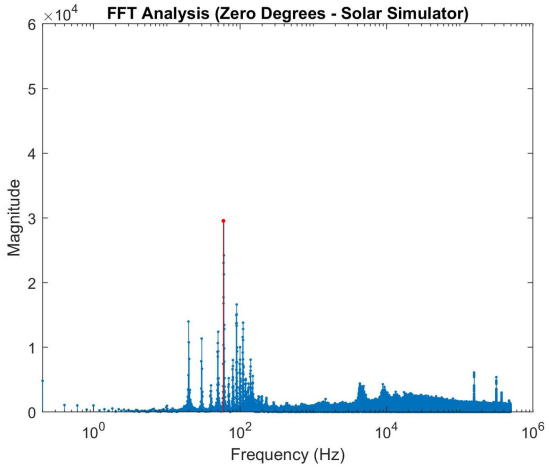

Figure 89. DVS240C Signal in the Frequency Domain at Zero Degrees with Solar Simulator

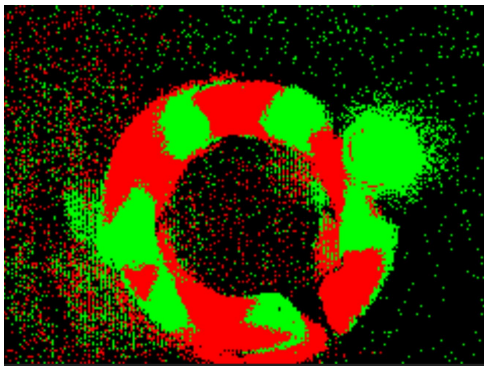

Figure 90. DVS240C Event Output - Zero Degrees with Solar Simulator

Figures 91-93 display DVS240C event data with the solar simulator at a ten degree angle with respect to the sensor. Again, Figures 91 and 93 help visualize the data and show that the solar simulator light bulb is partially visible. The figures make it clear that the dark object is detected by the sensor. Figure 92 shows 5 seconds of data in the frequency domain, with the largest frequency located at 60 Hz. This indicates the rotational speed of the circle and the value at this frequency is 61.62% greater than the signal at zero degrees. The rotational speed of the fan is clearer at this angle which is likely because the edge of the dark circle crossing in front of the

Sun (shown at zero degrees) generates more noise for the sensor. This again indicates that the DVS240C is capable of detecting dark objects in the presence of the Sun.

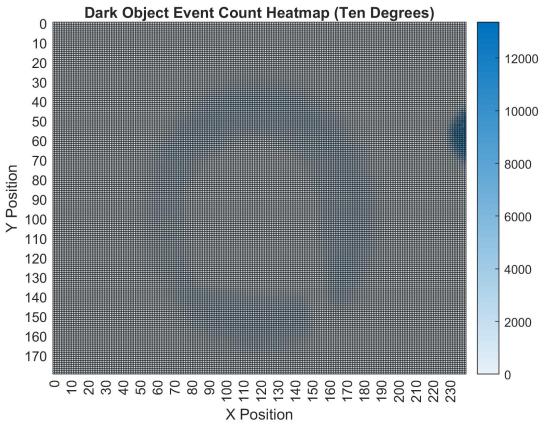

Figure 91. DVS240C Heatmap at Ten Degrees with Solar Simulator

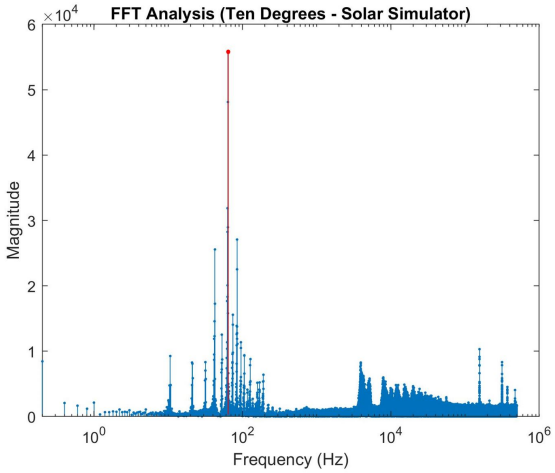

Figure 92. DVS240C Signal in the Freuency Domain at Ten Degrees with Solar Simulator

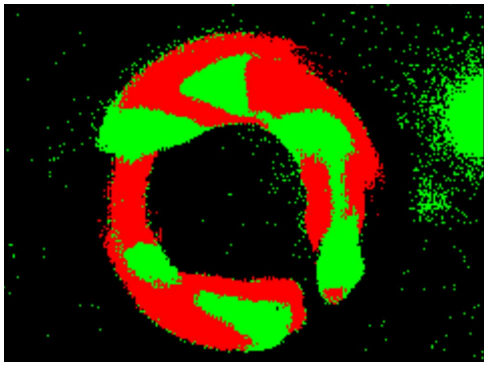

Figure 93. DVS240C Event Output - Ten Degrees with Solar Simulator

Although these tests show dark object detection, the rotating dark circle takes up a large portion of the sensor array. To determine if a smaller dark object is detected, a thin pencil is moved across the sensor's field of view. Figures 94 and 95 display two images of the event output accumulated onto a frame. In Figure 94, the center portion of the pencil can be seen as it changes the light intensity directly in front of the solar simulator bulb. In Figure 95, the entire pencil crossing the solar simulator

can be seen. These images are just two snapshots of event data collected during the dark object testing, but they indicate that the sensor does not saturate and is able to detect the object.

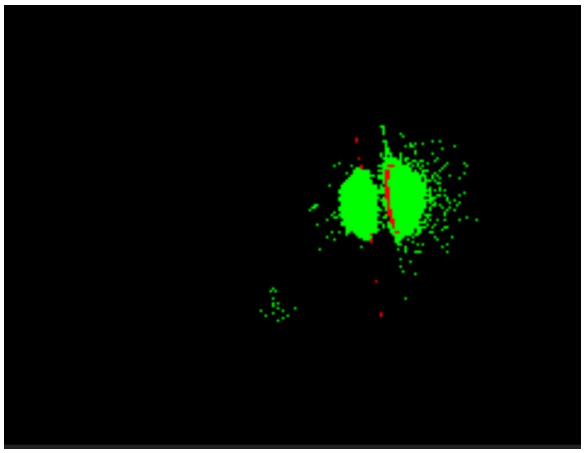

Figure 94. DVS240C Event Output - Pencil in front of Solar Simulator

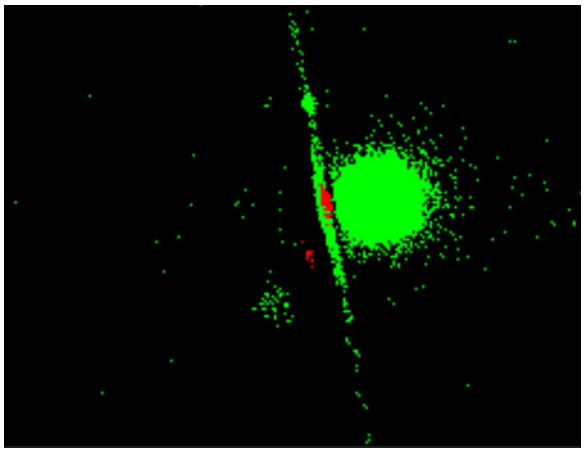

Figure 95. DVS240C Event Output - Pencil in front of Solar Simulator

Additional field testing with the setup shown in Figure 85 also indicates that the DVS240C can be used to detect dark objects in front of the Sun. Figures 96 and 97 display DVS240C event output data accumulated onto frames. The images are snapshots of the rotating black circle directly in front of the Sun. In both figures, the edges of the rotating circle can be seen.

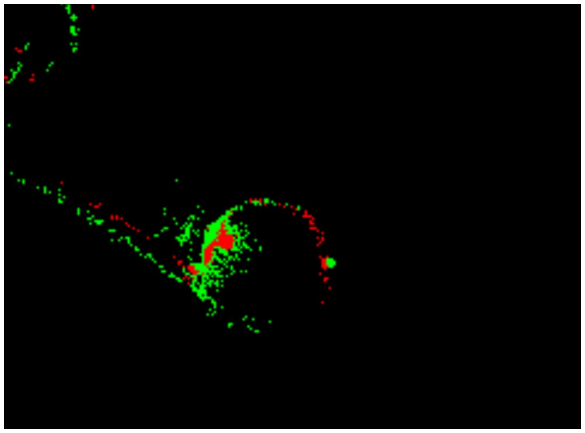

Figure 96. DVS240C Outside Pointed at the Sun

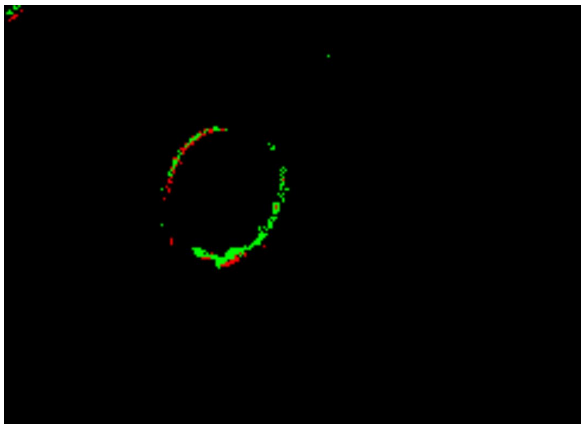

Figure 97. DVS240C Outside Pointed at the Sun

Figures 98, 99, and 100 display DVS240C data from moving a thin metal bar across the sensor's field of view. The data shows that the DVS240C does not saturate and a thin line of events is generated as the bar is moving across the sensor's field of view. Opposite from the blinking LED which generates its own light, less events are generated as the object moves away from the Sun. During these tests, the DVS240C APS sensor also attempted to collect data, however the sensor saturated.

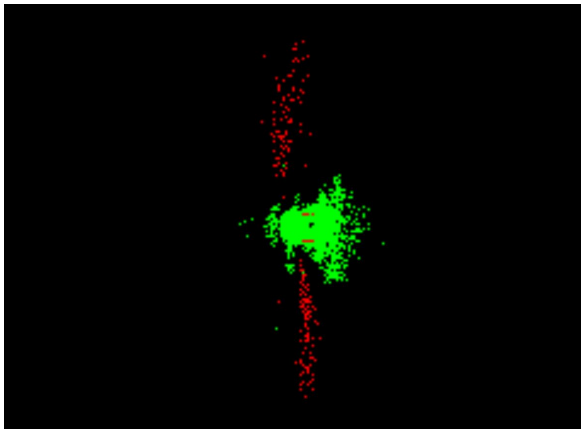

Figure 98. DVS240C Outside Pointed at the Sun

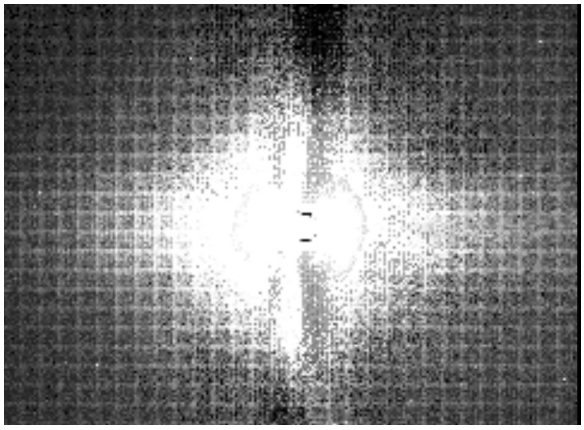

Figure 99. DVS240C Pointing Directly at Sun (Pseudoframe)

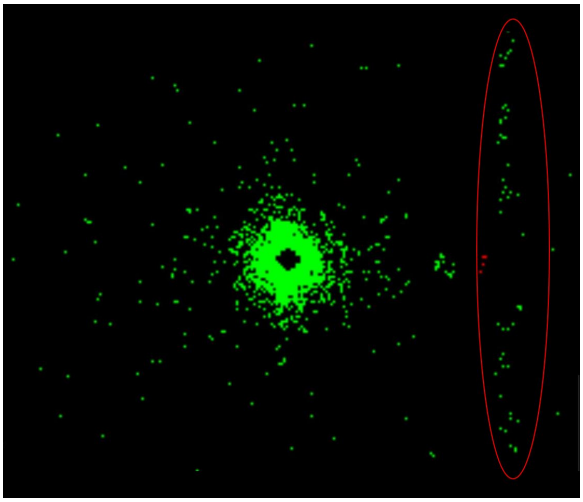

Figure 100. DVS240C Outside Pointed at the Sun

The test results show there is a potential SDA advantage of using the event-based sensor in space to do dark object detection near the Sun. The DVS240C does not

saturate when pointed directly at the Sun and therefore is able to detect dark objects passing across. However, additional testing is needed to gain a full understanding of dark object detection near the Sun. Experimental setup should involve changing the sensitivity settings as well as experimenting with objects of different sizes and locations relative to the sensor. Overall, the solar simulator and field tests have shown that it is advantageous and feasible to use event-based sensors for dark object detection near the Sun in space. The bright and dark object demonstrations show the feasibility of using event-based sensors to fill a gap in SDA that currently exists with traditional camera sensors.

4.4 Summary

This chapter has shown that the DVS240C passes all survivability tests. It is able to withstand high vacuum environments of 10^{-4} Torr, large temperature ranges between -24 to 61°C, and SMC acceptance level vibration profiles with negligible degradation to performance. Demonstration testing has also explored the possibility of using the event-based sensor for space-based SDA. The testing has shown that the sensor does not saturate within standard solar exclusion zones and is capable of detecting both bright and dark objects within these zones. Chapter V summarizes the research discoveries from this thesis and provides insight into the significance of the work. It finishes with a discussion of potential avenues for further research in this domain.

V. Conclusions and Recommendations

5.1 Conclusions of Research

Neuromorphic vision sensors may provide new capabilities for satellites in the space domain. Capable of withstanding environmental conditions seen at LEO and vibrations experienced at launch, postures the event-based vision sensor for future use in space. Additionally, displaying the advantage and feasibility to detect objects in front of the Sun gives purpose for further exploration of the event-based technology.

This thesis focused on two areas of research. It first investigated the DVS240C sensor's ability to withstand the low Earth orbit and launch environments through simulated testing. The event-based sensor survived all vacuum, thermal-vacuum, and vibration tests with no appreciable changes to sensor operation. Next, this thesis explored the possibility of using the sensor for space-based SDA through a demonstration of capability. It displayed the ability to detect both bright and dark objects passing in front of the Sun without saturation. Ultimately, this illustrates that event-based vision sensors are viable for future use on small satellites.

5.2 Significance of Research

Although this work is preliminary, displaying the initial viability of using the sensor in space opens the door for further exploration of the technology. Demonstrating that the sensor survives initial vacuum, thermal vacuum, and vibration tests, is likely to attract more aerospace scientists and engineers to the technology and finding a use for it. While only one application for the sensor has been explored in this thesis, it is likely that other space applications exist. Event-based sensors provide a low power, low latency, high temporal resolution, and high dynamic range solution, aligning with DoD's push towards smaller satellites. This research provides an initial assessment

with the hope of motivating further research efforts in bringing neuromorphic vision technology into space.

5.3 Recommendations for Future Work

Multiple avenues for future work with event-based vision sensors exist. For starters, additional survivability testing at a space qualification level could be done with the sensor. Space qualification level testing would require more thermal cycle tests and additional vibration testing with increased magnitude and duration. Executing a SWaP analysis could be another avenue for future work. Although, it is already known that the DVS240C has a small SWaP with a size of 70 x 60 x 25 mm^3, weight of 75g, and power draw of 5-14mW [12], a SWaP analysis with a specific mission in mind could help quantify the sensor's advantage for small satellites. This could also provide a path for future CubeSat integration and testing of the event-based sensor as a payload. Finally, future work could be done to explore other applications for the event-based sensors in space. Star sensing, to support attitude determination and control, is one possible application, but is not considered in this research due to time constraints. This thesis has provided an initial assessment of event-based sensor viability for space-based applications, making it possible to explore further in the future.

Appendix A. LED Thermal Vacuum Assembly

Appendix A displays CAD diagrams of the LED thermal vacuum assembly. The diagrams include specifications for the black aluminum LED box (lid hole pattern, holes to attach LED fixture, and hole to attach DB-9 connector). The diagrams also include specifications for the support brackets used to attach the black box and DVS240C to the test fixture. The assembly shown is used throughout vacuum, thermal vacuum, and vibration testing to collect DVS240C functional data. The assembly is also used throughout bright object SDA demonstration testing to collect DVS240C data.

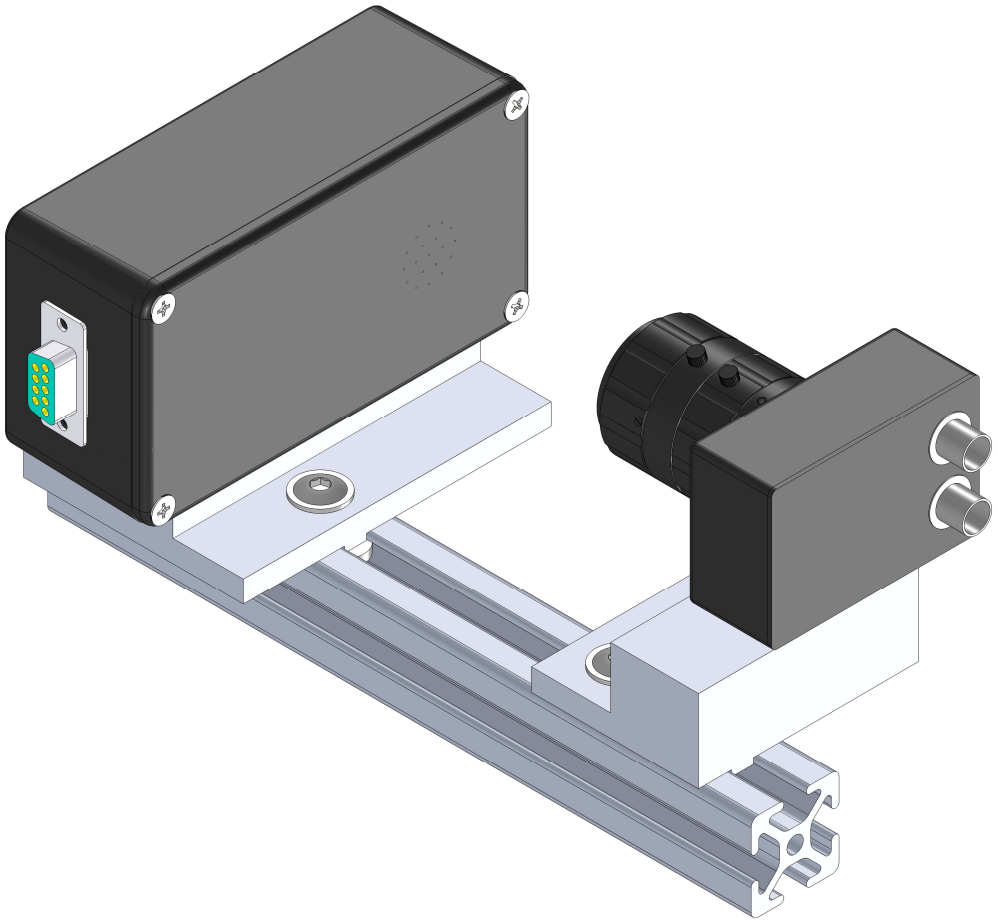

PARTNAME: LED TVAC ASSM
SLDDRW: LED TVAC ASSM

AFIT
AIR FORCE INSTITUTE OF TECHNOLOGY

WARNING: UNCLASSIFIED INFORMATION

THE INFORMATION CONTAINED IN THIS DRAWING IS PROPERTY OF AIR FORCE INSTITUTE OF TECHNOLOGY (AFIT).

ANY REPRODUCTION IN PART OR AS A WHOLE IS PROHIBITED BY ITAR CATEGORY "*XV SPACECRAFT SYSTEMS AND ASSOCIATED EQUIPMENT*"

UNLESS OTHERWISE SPECIFIED:
DIMENSIONS ARE INCHES

UNLESS SPECIFIED, TOLERANCES:
X.X ± 0.1"
X.XX ± 0.01"
X.XXX ± 0.005"
X.XXXX ± 0.0005"

MATERIAL

FINISH

DO NOT SCALE DRAWING

	NAME	DATE
DRAWN		7/22/2020
CHECKED		
ENG APPR.		
MFG APPR.		
Q.A.		

COMMENTS:

Overview

TITLE:

SIZE	DWG. NO.	REV
B		

SCALE: 1:1 | SHEET 1 OF 6

DRAWING LAST UPDATED: Wednesday, July 22, 2020 5:39:01 PM

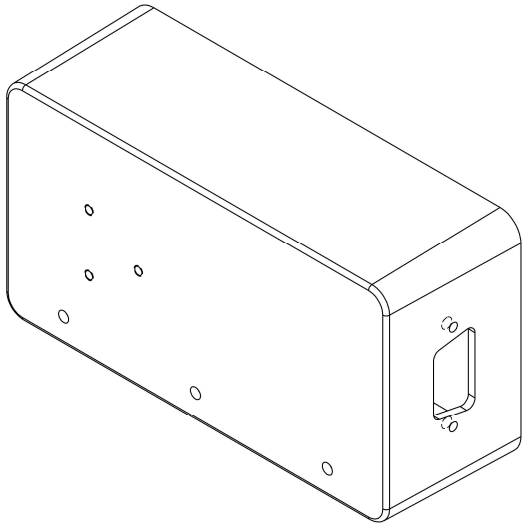

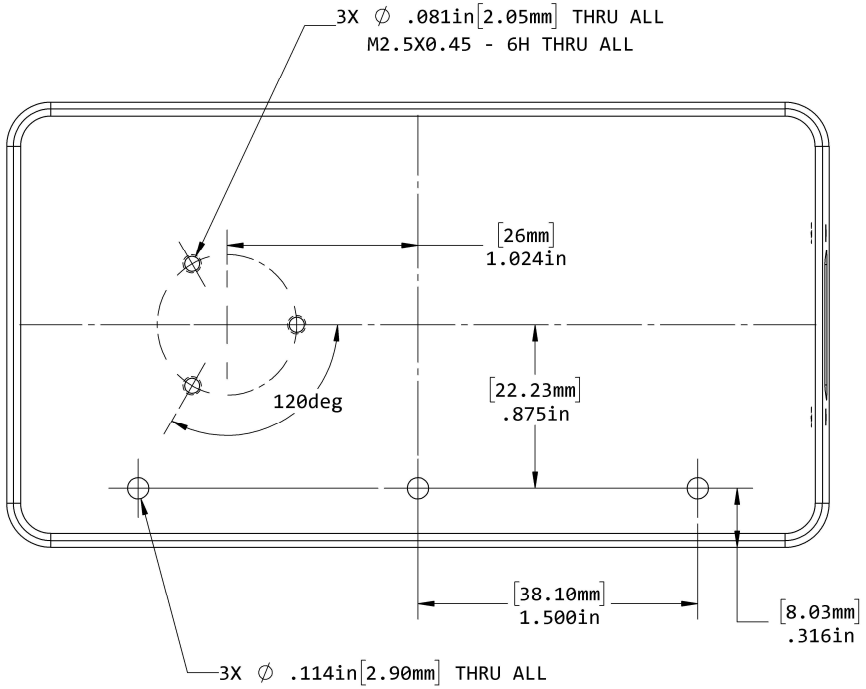

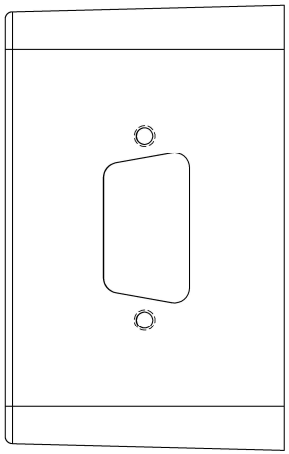

PARTNAME: 1590BS BOX
SLDDRW: LED TVAC ASSM

AFIT
Air Force Institute of Technology

WARNING: UNCLASSIFIED INFORMATION

THE INFORMATION CONTAINED IN THIS DRAWING IS PROPERTY OF AIR FORCE INSTITUTE OF TECHNOLOGY (AFIT).

ANY REPRODUCTION IN PART OR AS A WHOLE IS PROHIBITED BY ITAR CATEGORY "*XV SPACECRAFT SYSTEMS AND ASSOCIATED EQUIPMENT*"

UNLESS OTHERWISE SPECIFIED:
DIMENSIONS ARE INCHES

UNLESS SPECIFIED, TOLERANCES:
X.X ± 0.1"
X.XX ± 0.01"
X.XXX ± 0.005"
X.XXXX ± 0.0005"

MATERIAL: Material <not specified>
FINISH:
DO NOT SCALE DRAWING

	NAME	DATE
DRAWN		7/22/2020
CHECKED		
ENG APPR.		
MFG APPR.		
Q.A.		

COMMENTS:

LED Box 1 of 2

TITLE:

SIZE B | DWG. NO. | REV

SCALE: 1.5:1 | SHEET 2 OF 6

DRAWING LAST UPDATED: Wednesday, July 22, 2020 5:39:01 PM

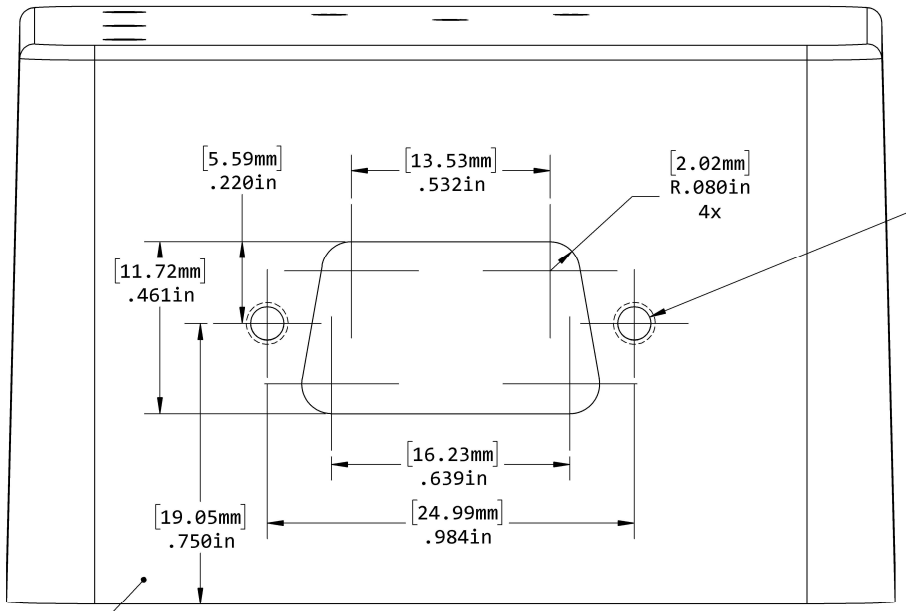

PARTNAME: 1590BS BOX
SLDDRW: LED TVAC ASSM

AFIT
Air Force Institute of Technology

WARNING: UNCLASSIFIED INFORMATION

THE INFORMATION CONTAINED IN THIS DRAWING IS PROPERTY OF AIR FORCE INSTITUTE OF TECHNOLOGY (AFIT).

ANY REPRODUCTION IN PART OR AS A WHOLE IS PROHIBITED BY ITAR CATEGORY "*XV SPACECRAFT SYSTEMS AND ASSOCIATED EQUIPMENT*"

UNLESS OTHERWISE SPECIFIED:
DIMENSIONS ARE INCHES

UNLESS SPECIFIED, TOLERANCES:
X.X ± 0.1"
X.XX ± 0.01"
X.XXX ± 0.005"
X.XXXX ± 0.0005"

MATERIAL
Material <not specified>

FINISH

DO NOT SCALE DRAWING

	NAME	DATE
DRAWN		7/22/2020
CHECKED		
ENG APPR.		
MFG APPR.		
Q.A.		

COMMENTS:

LED Box 2 of 2

TITLE:

SIZE	DWG. NO.	REV
B		

SCALE: 3:1 | SHEET 3 OF 6

DRAWING LAST UPDATED: Wednesday, July 22, 2020 5:39:01 PM

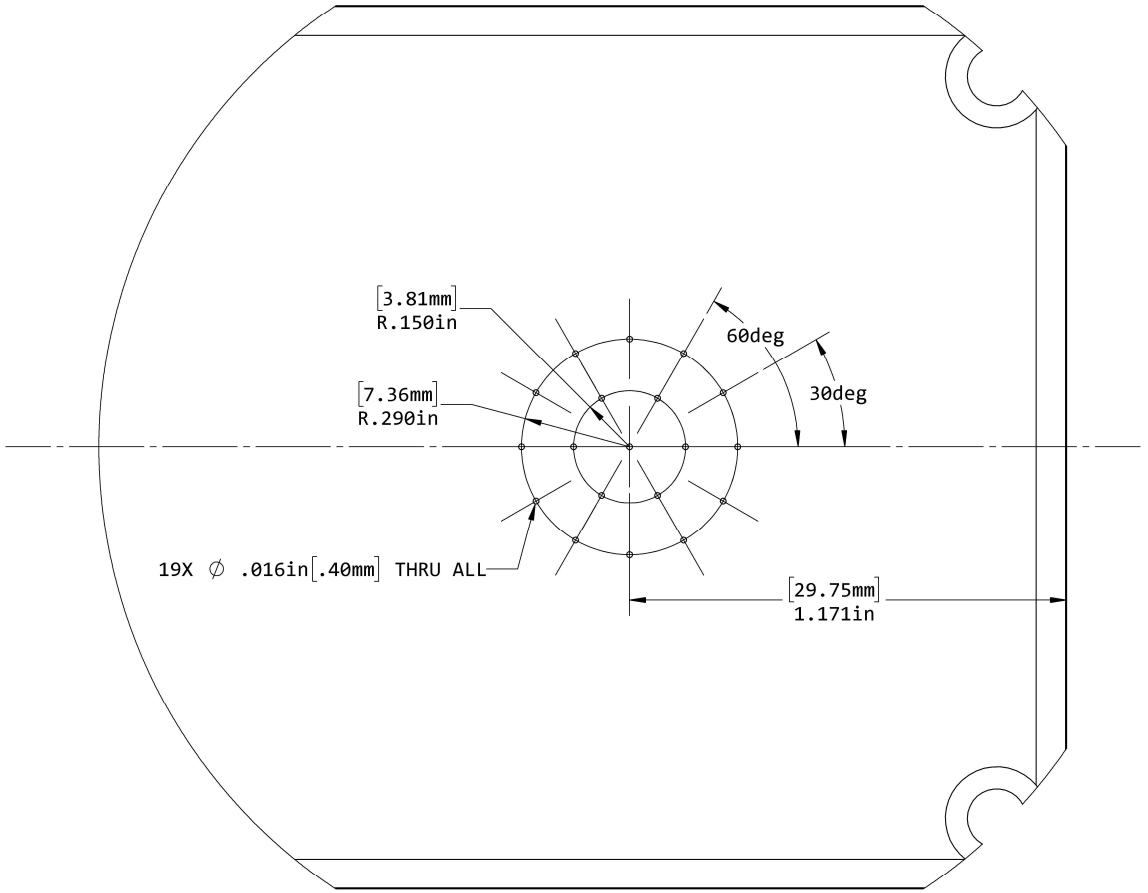

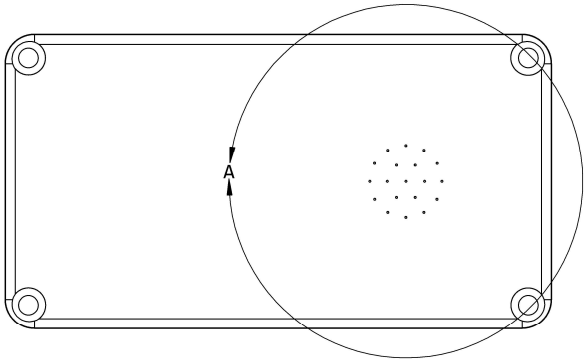

DETAIL A
SCALE 3 : 1

PARTNAME: 1590B-BS LID
SLDDRW: LED TVAC ASSM

AIR FORCE INSTITUTE OF TECHNOLOGY

WARNING: UNCLASSIFIED INFORMATION

THE INFORMATION CONTAINED IN THIS DRAWING IS PROPERTY OF AIR FORCE INSTITUTE OF TECHNOLOGY (AFIT).

ANY REPRODUCTION IN PART OR AS A WHOLE IS PROHIBITED BY ITAR CATEGORY "*XV SPACECRAFT SYSTEMS AND ASSOCIATED EQUIPMENT*"

UNLESS OTHERWISE SPECIFIED:
DIMENSIONS ARE INCHES

UNLESS SPECIFIED, TOLERANCES:
X.X ± 0.1"
X.XX ± 0.01"
X.XXX ± 0.005"
X.XXXX ± 0.0005"

MATERIAL: Material <not specified>
FINISH:
DO NOT SCALE DRAWING

	NAME	DATE
DRAWN		7/22/2020
CHECKED		
ENG APPR.		
MFG APPR.		
Q.A.		

COMMENTS:

LED Box Lid

TITLE:

SIZE	DWG. NO.	REV
B		

SCALE: 1:1 | SHEET 4 OF 6

DRAWING LAST UPDATED: Wednesday, July 22, 2020 5:39:01 PM

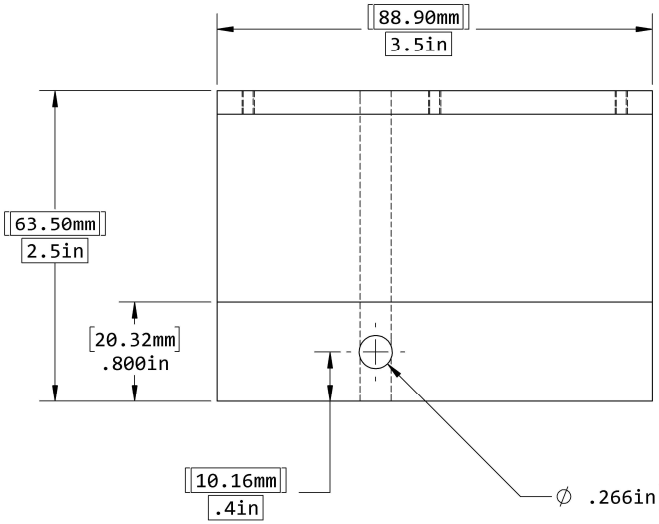

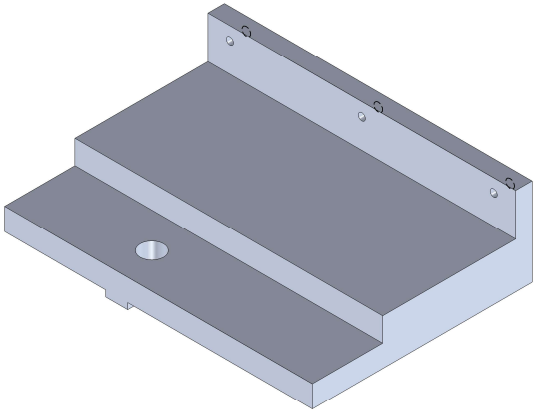

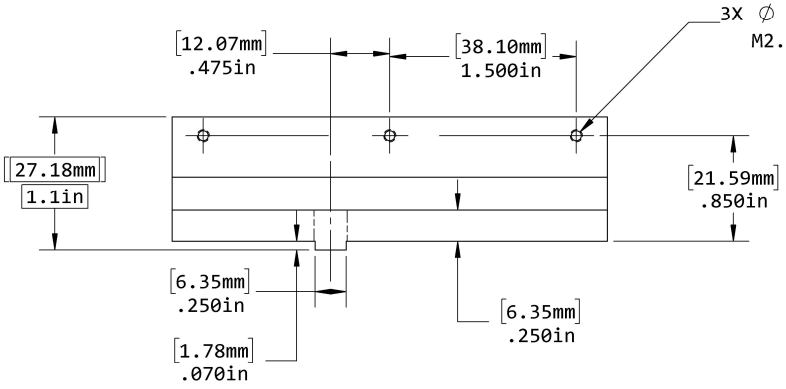

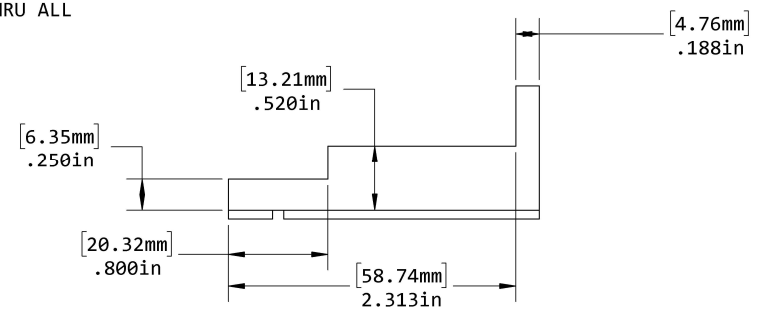

PARTNAME: LED Support Block
SLDDRW: LED TVAC ASSM

AFIT
Air Force Institute of Technology

WARNING: UNCLASSIFIED INFORMATION

THE INFORMATION CONTAINED IN THIS DRAWING IS PROPERTY OF AIR FORCE INSTITUTE OF TECHNOLOGY (AFIT).

ANY REPRODUCTION IN PART OR AS A WHOLE IS PROHIBITED BY ITAR CATEGORY "*XV SPACECRAFT SYSTEMS AND ASSOCIATED EQUIPMENT*"

UNLESS OTHERWISE SPECIFIED:
DIMENSIONS ARE INCHES

UNLESS SPECIFIED, TOLERANCES:
X.X ± 0.1"
X.XX ± 0.01"
X.XXX ± 0.005"
X.XXXX ± 0.0005"

MATERIAL: 6061 Alloy
FINISH:
DO NOT SCALE DRAWING

	NAME	DATE
DRAWN		7/22/2020
CHECKED		
ENG APPR.		
MFG APPR.		
Q.A.		

COMMENTS:

LED Box Support

TITLE:

SIZE B | DWG. NO. | REV

SCALE: 1:1 | SHEET 5 OF 6

DRAWING LAST UPDATED: Wednesday, July 22, 2020 5:39:01 PM

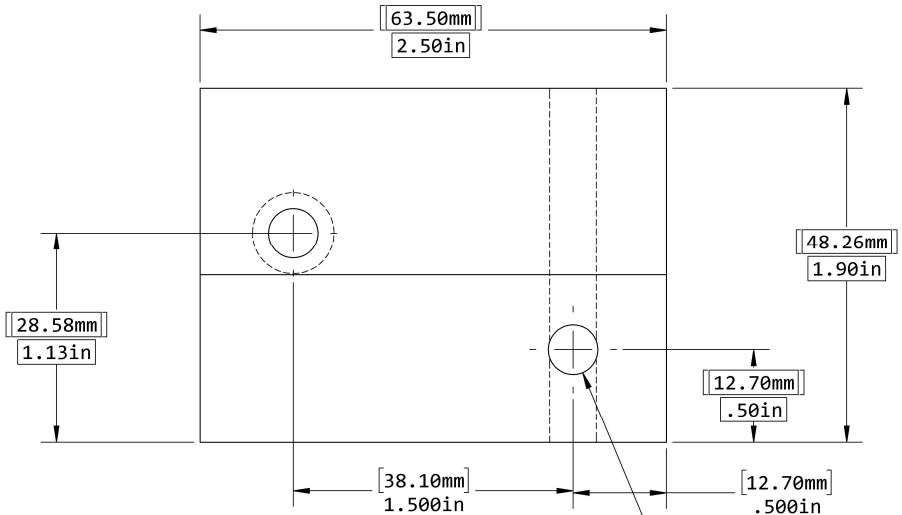

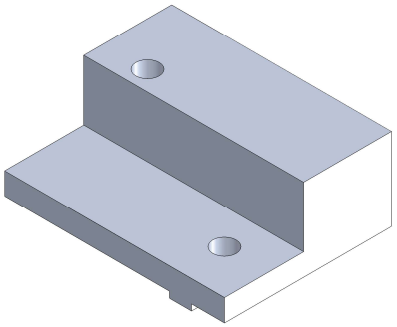

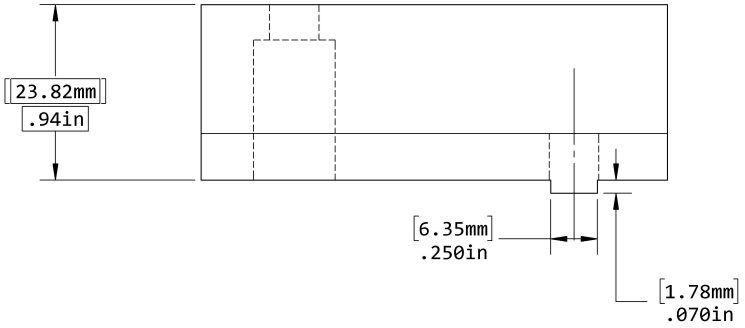

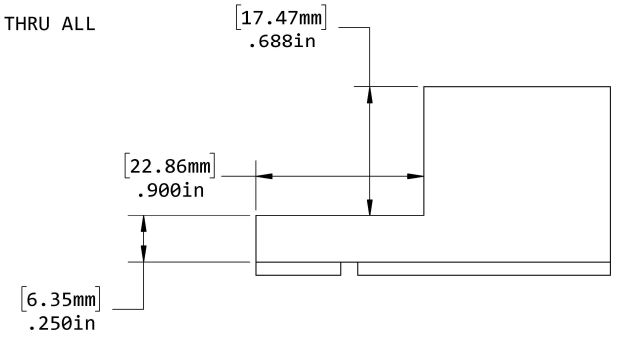

PARTNAME: Camera Support Block
SLDDRW: LED TVAC ASSM

AFIT
AIR FORCE INSTITUTE OF TECHNOLOGY

WARNING: UNCLASSIFIED INFORMATION

THE INFORMATION CONTAINED IN THIS DRAWING IS PROPERTY OF AIR FORCE INSTITUTE OF TECHNOLOGY (AFIT).

ANY REPRODUCTION IN PART OR AS A WHOLE IS PROHIBITED BY ITAR CATEGORY *"XV SPACECRAFT SYSTEMS AND ASSOCIATED EQUIPMENT"*

UNLESS OTHERWISE SPECIFIED:
DIMENSIONS ARE INCHES

UNLESS SPECIFIED, TOLERANCES:
X.X ± 0.1"
X.XX ± 0.01"
X.XXX ± 0.005"
X.XXXX ± 0.0005"

MATERIAL: 6061 Alloy
FINISH:
DO NOT SCALE DRAWING

	NAME	DATE
DRAWN		7/22/2020
CHECKED		
ENG APPR.		
MFG APPR.		
Q.A.		

COMMENTS:

Camera Support

TITLE:

SIZE B | DWG. NO. | REV

SCALE: 1.5:1 | SHEET 6 OF 6

DRAWING LAST UPDATED: Wednesday, July 22, 2020 5:39:01 PM

Appendix B. Vibration Testing Assembly

Appenidix B displays CAD diagrams of the vibration testing assembly. It details the specifications of the bracket used to attach and hold the DVS240C camera to the shaker table during vibration testing.

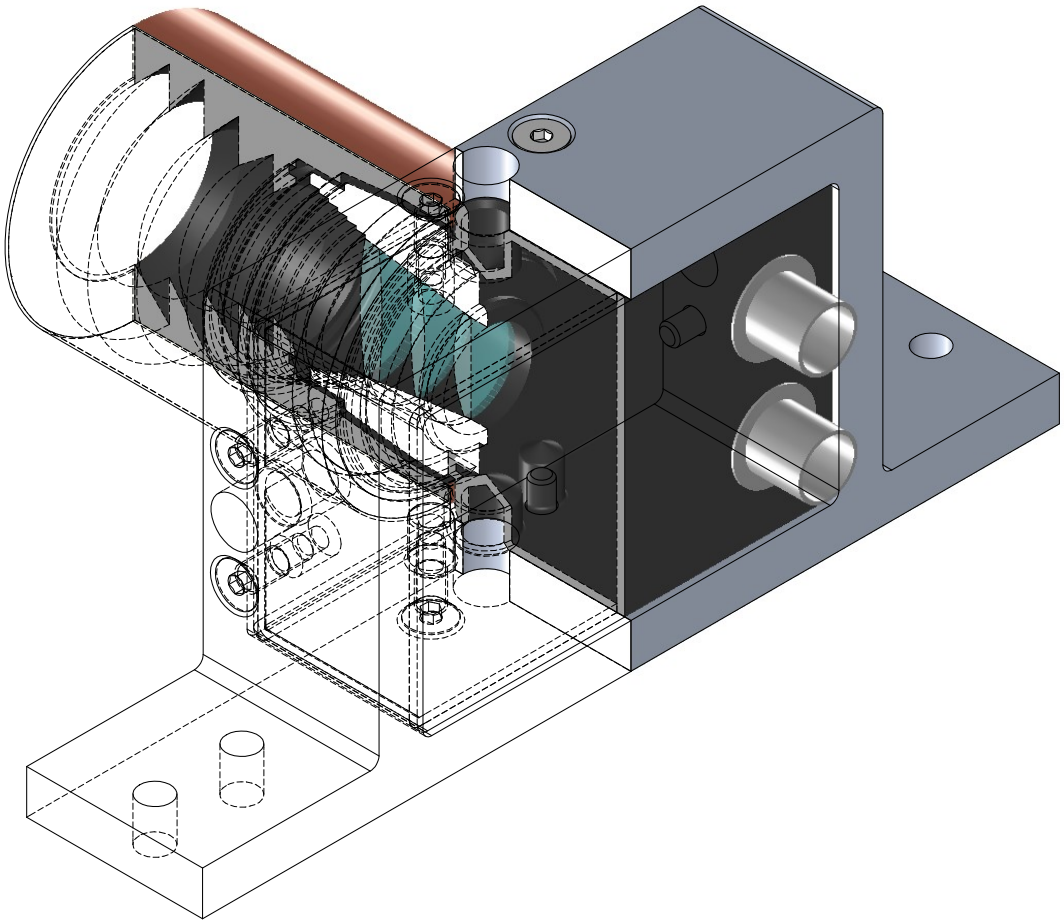

PARTNAME: Vibe Test Camera ASSM
SLDDRW: Vibe Test ASSM

DRAWING LAST UPDATED: Monday, January 4, 2021 5:26:01 PM

ITEM NO.	PART NUMBER	Description	Material	PartNo	QTY.	Vendor	Notes
1	Camera DVS240	Camera DVS240	Ultem		1		
2	Marshall Electronics V-4612-CS	Camera Lens	Various Composited		1	COTS	
3	Marshall Baffle V2	MarshallBaffleV2	Ultem		1		
4	Copper Wrap	Copper Wrap	Copper		1		
5	Camera Vibe Support	Camera Vibe Support	6061 Alloy	AMS	1	AFIT Model Shop	
6	M3X10 FHCS	M3 x 10mm Long FHCS	Stainless Steel	92125A130	8	McMaster-Carr	https://www.mcmaster.com/92125A130/
7	8-32 x 7_16 Long SHCS	8-32 x 7/16" Long SHCS	Stainless Steel	92196A193	2	McMaster-Carr	https://www.mcmaster.com/92196A193/

*** Fastener quantity is for one assembly**

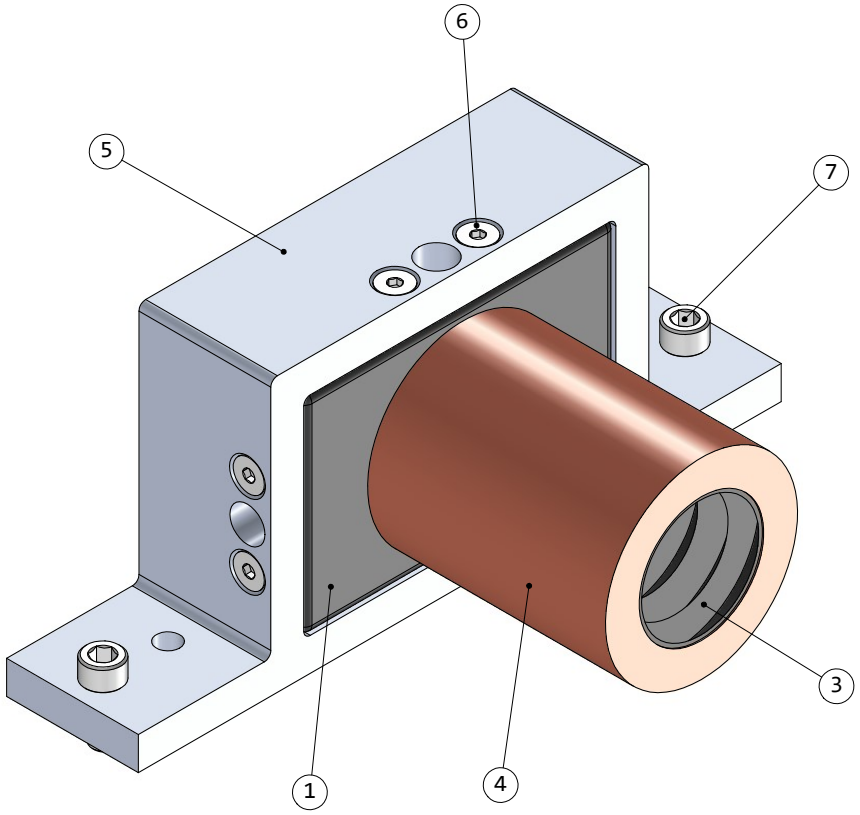

PARTNAME: Vibe Test Camera ASSM
SLDDRW: Vibe Test ASSM

DRAWING LAST UPDATED: Monday, January 4, 2021 5:26:01 PM

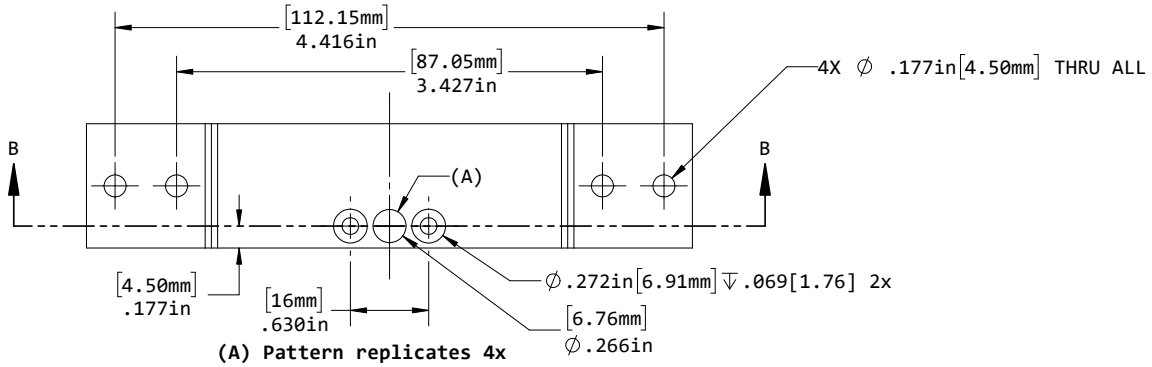

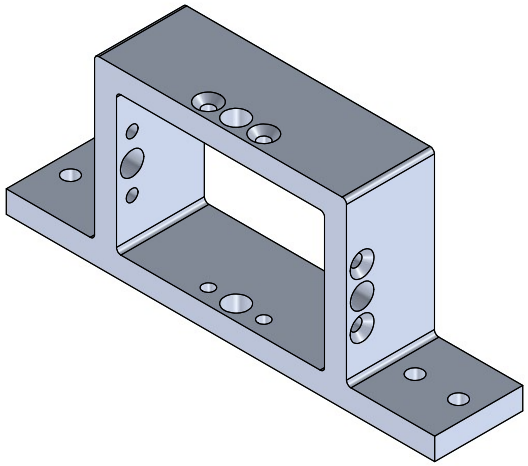

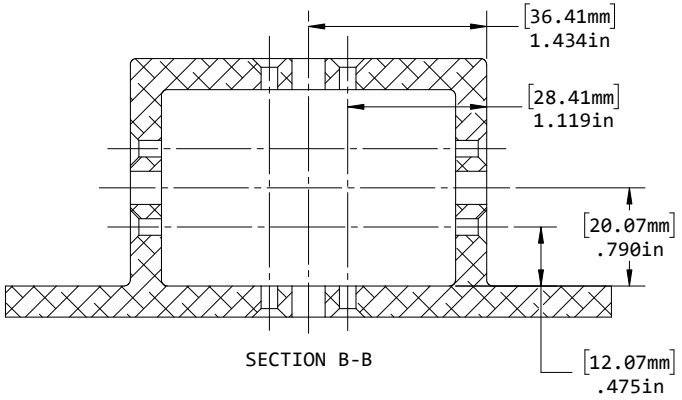

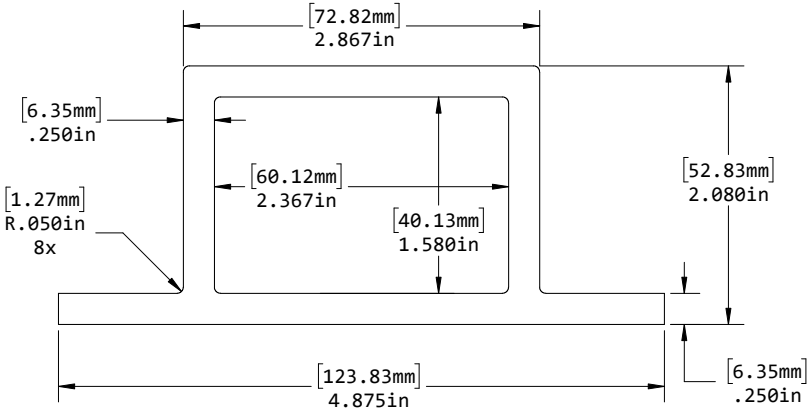

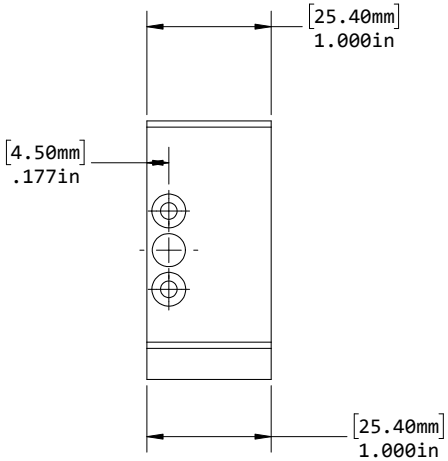

PARTNAME: Camera Vibe Support

SLDDRW: Vibe Test ASSM

DRAWING LAST UPDATED: Monday, January 4, 2021 5:26:01 PM

Bibliography

[1] P. Lichtsteiner, *An AER Temporal Contrast Vision Sensor*. PhD thesis, Swiss Federal Institute of Technology Zurich, 2006.

[2] C. Posch, T. Serrano-Gotarredona, B. Linares-Barranco, and T. Delbruck, "Retinomorphic event-based vision sensors: Bioinspired cameras with spiking output," *Proceedings of the IEEE*, vol. 102, no. 10, pp. 1470–1484, 2014.

[3] P. Lichtsteiner, C. Posch, and T. Delbruck, "A 128× 128 120 db 15 µs latency asynchronous temporal contrast vision sensor," *Solid-State Circuits, IEEE Journal of*, vol. 43, pp. 566 – 576, 03 2008.

[4] B. McReynolds, "A comprehensive test methodology and physics-based camera model for characterizing neuromorphic imagers," Master's thesis, Air Force Institute of Technology, 2019.

[5] U. Robotics and P. Group, "Event-based,6-dof pose tracking for high-speed maneuvers using a dynamic vision sensor." `https://www.youtube.com/watch?v=LauQ6LWTkxM&feature=youtu.be&t=35s`, 2014.

[6] H. Kim, *Real-time visual SLAM with an event camera*. PhD thesis, Imperial College London, 2017.

[7] J. Boettiger, "A comparative evaluation of the detection and tracking capability between novel event-based and conventional frame-based sensors," Master's thesis, Air Force Institute of Technology, 2020. 3154.

[8] G. Gallego, T. Delbrück, G. Orchard, C. Bartolozzi, B. Taba, A. Censi, S. Leutenegger, A. J. Davison, J. Conradt, K. Daniilidis, and D. Scaramuzza, "Event-based vision: A survey," *CoRR*, vol. abs/1904.08405, 2019.

[9] *Silicon Retinas*, ch. 3, pp. 37–69. John Wiley & Sons, Ltd, 2015.

[10] T. Delbruck and P. Lichtsteiner, "Fast sensory motor control based on event-based hybrid neuromorphic-procedural system," in *2007 IEEE International Symposium on Circuits and Systems*, pp. 845–848, 2007.

[11] G. Cohen, S. Afshar, A. van Schaik, A. Wabnitz, T. Bessell, M. Rutten, and B. Morreale, "Event-based sensing for space situational awareness," 11 2017.

[12] iniVation, "Dvs240 specifications," 2019.

[13] *Test Requirements for Launch, Upper-Stage and Space Vehicles, SMC-S-016*. Air Force Space Command Space and Missile Systems Center, 2014.

[14] G. Cohen, S. Afshar, and A. van Schaik, "Approaches for Astrometry using Event-Based Sensors," in *The Advanced Maui Optical and Space Surveillance Technologies Conference* (S. Ryan, ed.), p. 38, Sept. 2018.

[15] D. Scaramuzza and G. Gallego, "Event-based cameras: Challenges and opportunities." `https://www.youtube.com/watch?v=SU_Fp4xS_g4`, 2019.

[16] iniVation, "User guide: Biasing dynamic sensors." `https://gitlab.com/inivation/inivation-docs/-/blob/master/Advanced%20configurations/User_guide_-_Biasing.md#user-guide-biasing-dynamic-sensors`, 2018.

[17] T. Delbruck, "The development of the dvs and davis sensors." `https://www.youtube.com/watch?v=kisqhMqbWTU`, 2017.

[18] T. Nguyen, X. Pham, J. Song, S. Jin, D. Kim, and J. Jeon, "Compensating background for noise due to camera vibration in uncalibrated-camera-based vehicle speed measurement system," *Vehicular Technology, IEEE Transactions on*, vol. 60, pp. 30 – 43, 02 2011.

[19] A. Mitrokhin, C. Fermüller, C. Parameshwara, and Y. Aloimonos, "Event-based moving object detection and tracking," *CoRR*, vol. abs/1803.04523, 2018.

[20] I. Ruelas, G. Torres, E. U. Moya-Sanchez, and S. Ortega-Cisneros, "Pedestrian detection and tracking using a dynamic vision sensor," *Computacion y Sistemas*, vol. 22, p. 1077, 01 2019.

[21] D. Reverter Valeiras, X. Lagorce, X. Clady, C. Bartolozzi, S.-H. Ieng, and R. Benosman, "An asynchronous neuromorphic event-driven visual part-based shape tracking," *IEEE transactions on neural networks and learning systems*, vol. 26, p. 3045—3059, December 2015.

[22] S. Afshar, A. P. Nicholson, A. van Schaik, and G. Cohen, "Event-based object detection and tracking for space situational awareness," 2019.

[23] M. McHarg, "Stp-h7 falcon neuro: Critical design review." University Power Point Presentation, April 2020.

[24] M. Finckenor and K. de Groh, *A Researcher's Guide to: International Space Station Space Environmental Effects*. NASA ISS Program Science Office, 2015.

[25] C. Leonard, "Challenges for electronic circuits in space applications," 2017.

[26] U. Food and D. Administration, "Tin whiskers problems, causes, and solutions." `https://www.fda.gov/inspections-compliance-enforcement-and-criminal-investigations/inspection-technical-guides/tin-wiskers-problems-causes-and-solutions`.

[27] V. Pisacane, *The Space Environment and Its Effects on Space Systems*. American Institute of Aeronautics and Astronautics, 2 ed., 2016.

[28] C. Magnetics, "The effect of temperature on the life of power electronic devices." https://www.fda.gov/inspections-compliance-enforcement-and-criminal-investigations/inspection-technical-guides/tin-wiskers-problems-causes-and-solutions, 2015.

[29] B. K. . G. S. . P. Thernherr, "Electrical equipment in cold weather applications." https://www.eaton.com/content/dam/eaton/markets/oil-and-gas/knowledge-center/whitepaper/Electrical-equipment-in-cold-weather-applications.pdf, 2013.

[30] K. LaBel, "Radiation effects on electronics 101: Simple concepts and new challenges." https://nepp.nasa.gov/docuploads/392333B0-7A48-4A04-A3A72B0B1DD73343/Rad_Effects_101_WebEx.pdf, 2004.

[31] D. A. Vallado, P. J. Cefola, R. Kiziah, and M. Ackermann, *Removing the Solar Exclusion with High Altitude Satellites*.

[32] iniVation, "Dv software and manual." https://inivation.gitlab.io/dv/dv-docs/docs/getting-started.html.

[33] *Thermal Vacuum Solar Simulation System for Wright Patterson AFB, User Guide*. Abbess Instruments and Systems Inc., 2013.

[34] Y. Nozaki and T. Delbruck, "Temperature and parasitic photocurrent effects in dynamic vision sensors," *IEEE Transactions on Electron Devices*, vol. 64, no. 8, pp. 3239–3245, 2017.

[35] *General Environmental Verification Standards (GEVS), GSFC-STD-7000A*. NASA Goddard Space Flight Center, April 2013.

[36] MATLAB, "Fast fourier transform." https://www.mathworks.com/help/matlab/ref/fft.html.

REPORT DOCUMENTATION PAGE

Form Approved
OMB No. 0704-0188

1. REPORT DATE *(DD-MM-YYYY)*	2. REPORT TYPE	3. DATES COVERED *(From - To)*
05-03-2021	Master's Thesis	Aug 2019 – Mar 2021

4. TITLE AND SUBTITLE
Neuromorphic Vision Sensors for Space-Based Applications

5a. CONTRACT NUMBER

5b. GRANT NUMBER

5c. PROGRAM ELEMENT NUMBER

6. AUTHOR(S)
Horn, Jessica L., Capt, USAF

5d. PROJECT NUMBER

5e. TASK NUMBER

5f. WORK UNIT NUMBER

7. PERFORMING ORGANIZATION NAME(S) AND ADDRESS(ES)
Air Force Institute of Technology
Graduate School of Engineering and Management (AFIT/ENY)
2950 Hobson Way, Building 640
WPAFB OH 45433-8865

8. PERFORMING ORGANIZATION REPORT NUMBER
AFIT-ENY-MS-21-M-304

9. SPONSORING/MONITORING AGENCY NAME(S) AND ADDRESS(ES)
Intentionally Left Blank

10. SPONSOR/MONITOR'S ACRONYM(S)

11. SPONSOR/MONITOR'S REPORT NUMBER(S)

12. DISTRIBUTION/AVAILABILITY STATEMENT
DISTRIBUTION STATEMENT A:
APPROVED FOR PUBLIC RELEASE; DISTRIBUTION UNLIMITED.

13. SUPPLEMENTARY NOTES
This material is declared a work of the U.S. Government and is not subject to copyright protection in the United States.

14. ABSTRACT
This research examines the viability of event-based vision (neuromorphic) sensors for future use on satellites. Outputting single pixel events only when a change in intensity is detected, event-based vision sensors offer a potential low power, low latency, high temporal resolution, and high dynamic range solution as compared to traditional CCD or CMOS camera technology. The commercial off-the-shelf DVS240C sensor, is analyzed to determine if operability is affected by launch conditions and the low Earth space environment through vacuum, thermal vacuum, and vibration tests. No appreciable changes in sensor operation was observed throughout testing. Additionally, the sensor was able to detect both bright and dark objects directly in front of a solar simulator without pixel saturation, demonstrating its high dynamic range which provides a possible advantage for use on space-based platforms.

15. SUBJECT TERMS
Event-based sensors, neuromorphic sensors, TVAC testing, vibration testing

16. SECURITY CLASSIFICATION OF:			17. LIMITATION OF ABSTRACT	18. NUMBER OF PAGES	19a. NAME OF RESPONSIBLE PERSON
a. REPORT	b. ABSTRACT	c. THIS PAGE			Little, Bryan D., Lt Col USAF AFIT/ENY
					19b. TELEPHONE NUMBER *(Include area code)*
U	U	U	UU	97	(937) 225-6565 byran.little@afit.edu